INSULIN TRAFFICKING PERTURBATIONS AT THE BLOOD-BRAIN BARRIER IN ALZHEIMER'S DISEASE MODELS

A THESIS

SUBMITTED TO THE FACULTY OF THE

UNIVERSITY OF MINNESOTA

BY

VIDUR SARMA

IN PARTIAL FULFILLMENT OF THE REQUIREMENTS

FOR THE DEGREE OF

DOCTOR OF PHILOSOPHY

KARUNYA KANDIMALLA

NOVEMBER 2017

ACKNOWLEDGEMENTS

My journey to attaining a Ph.D has been replete with learning curves, obstacles, discoveries and self-reflection. It began from a nascent stage in my post-graduate educational career. There were innumerable disappointments on the way but my upbringing and training taught me how to be resilient and develop situational awareness. For that, I am grateful to my parents, immediate family, friends, labmates, and the spirit of the city of Bombay.

I am grateful to my advisor, Dr. Karunya Kandimalla, for accepting me on board and providing me with enough resources, time and space to find my own within the scientific community. I am thankful to him for being patient with me, being cognizant of my learning curve but at the same time, not allowing me to settle for anything less than the best and most accurate. I would also like to extend my gratitude toward my thesis committee members, Drs. William Elmquist, Ling Li and Ronald Siegel, who have been supportive of my thesis proposal and ongoing research.

I am also honored to have had ‘big brother’ figures during my program at the University of Minnesota such as Dr. Suresh Swaminathan and Dr. Rajesh Omtri. They walked me through experimental procedures and nuances thereof. At the Mayo Clinic, I have been fortunate to learn about molecular imaging, animal surgeries and protocols from Geoffry Curran and Dr. Val Lowe, the director of the PET imaging facility. Radioactivity protocols and animal experiments would be tedious if not for the free-spiritedness and popularity of Geoff. Working with Dr.

Lowe, Geoff, Tyler and Paul has taught me how to adapt to differences in scientific investigation, presentation style and culture.

I have been extremely fortunate to be chosen to work within the fold of two honorable institutions, Mayo Clinic (Department of Neurology) and the University of Minnesota (Department of Pharmaceutics), every day for 5 years. Being embedded in the research environment and communicative process at these institutions has taught me how to apply tools to distinguish fact from fiction, and fact from opinion. They have instilled in me, concepts of innovation, team work, reciprocation, humility, free speech, justice and above all, equality. I have understood the investigative process in biomedical science well and become aware of differences in healthcare networks between America and India.

ABSTRACT

Alzheimer's disease (AD) is recognized as a multifactorial disease and a major cause of dementia in the elderly. Pathological hallmarks of AD include brain amyloid beta (Aβ) deposits and intraneuronal tangles of hyperphosphorylated tau protein. Reduction of brain Aβ burden is widely considered as a viable therapeutic strategy for AD, and developing methods to promote brain Aβ clearance has been at the forefront of AD research. Recent clinical trials conducted in a small group of AD patients demonstrated the efficacy of intranasally-administered insulin in improving memory and reducing brain amyloid burden (Craft et al., 2012). Although the mechanism of insulin action is not clear, epidemiological studies have linked type 2 diabetes (T2DM), characterized by hyperinsulinemia and peripheral insulin resistance, with cognitive decline and amyloid burden in AD (Matsuzaki et al., 2010).

One possibility is that hyperinsulinemia damages the cerebrovascular endothelium, referred to as the blood brain barrier (BBB). The BBB is a major signaling and material trafficking pathway between plasma and brain that not only delivers glucose and insulin to brain but also serves as the primary clearance portal for brain Aβ (Storck et al., 2016; Yuede et al., 2016). Hence, T2DM could augment AD pathology by inhibiting insulin delivery and disrupting brain Aβ clearance. Although, intranasal insulin may remedy the situation, this approach may be limited, due to variable absorption of insulin into CNS. Moreover, insulin is a growth factor with multiple physiological targets; hence, chronic insulin therapy will have off-target effects. As a fundamental approach,

critical insulin-responsive cellular and molecular pathways that facilitate Aβ trafficking should be identified. Only through elucidating these dysfunctions in AD/T2DM can novel therapeutic targets be rationally sought. In this work, **the key questions concern the dynamics of insulin transport from systemic circulation into brain via the BBB and the disruption in insulin trafficking caused by Aβ peptides in AD brain**. Importantly, molecular components in the insulin trafficking/signaling pathway that are disturbed by Aβ exposure were identified as well as the perturbed insulin delivery and brain insulin resistance. This new knowledge will facilitate the search for novel therapeutic targets for AD.

I have been investigating mechanisms triggering insulin scarcity in AD brains by conducting kinetic biodistribution and SPECT/CT imaging assays in Aß peptide over-producing transgenic mice (APP/PS1), insulin resistant db/db (leptin receptor deficient) and aged WT mice. I analyzed plasma pharmacokinetic and dynamic brain uptake data by 3-compartmental analysis on SAAM© and discovered differences in distribution rate constants between WT and the insulin-resistant mouse groups. Upon simulating tissue distribution of a given dose of insulin in a 3-compartmental Stella© model with the estimated rate constants, I discovered that APP/PS1, db/db aged, and Aβ40/Aβ42 pre-treated WT mouse display higher plasma AUC and lower brain AUC levels of insulin, as compared to healthy, young WT mice. This led us to a hypothesis that Aß40 and Aß42 interfere with the transport of insulin into the brain parenchyma.

Now, the appearance of systemic insulin in the brain parenchyma is contingent upon insulin receptors (IR) expressed by BBB endothelial cells. Therefore, I

employed human cerebrovascular microendothelial cells (hCMEC) and over-expressed hCMEC monolayers with IR to investigate mechanistic interactions between Aß peptides and insulin transcytosis across the BBB. The processes involved in insulin transcytosis across BBB endothelial cells are postulated to operate in tandem with downstream signaling cascades. I studied variables in IR-mediated transport processes and correlated the results with shifts in phosphorylation of proteins expressed in downstream insulin signaling pathways, because of Aß peptide exposure.

Through flow cytometry and radioactive Transwell© transport assays, I discovered that the IR-mediated uptake, permeability and exocytosis of insulin across hCMEC/D3 cells were significantly impaired by pre-exposure to Aβ40 and Aβ42. With help of FRAP/FLIP imaging analyses, I found that the half-life of lateral diffusion and exocytic recycling of IR in response to insulin was increased in presence of Aβ40 and Aβ42. With respect to hCMEC/D3 signal transduction downstream of IR, Western Blot analyses confirmed that Aβ40 and Aβ42 excessively activated the phosphorylation of the IR-β subunit at Tyr1162/1163 and decreased the phosphorylation of Akt at Ser 473. In addition, reverse-phase protein array (RPPA) assays revealed that phosphorylation of MAPK3 was increased whereas that of caveolin-1 was decreased due to Aβ40 and Aβ42 exposure. My results lead to conclude that Aβ peptides interfere with insulin signaling/trafficking at the BBB and reduce insulin availability in the AD brain. It is therefore imperative to rectify motifs which result in impaired insulin signaling at the BBB to improve its transport into the brain parenchyma.

TABLE OF CONTENTS

LIST OF TABLES

LIST OF FIGURES

CHAPTER 1. INTRODUCTION

1.1 Synopsis

Alzheimer's disease (AD) pathology is caused by age, genetic or environmental factors, however the temporal progression of the disease due to any of these risk factors remains poorly understood. One major risk factor is Type-2 Diabetes (T2DM), which is caused due to an unresponsiveness of tissues to insulin signaling (Ott et al., 1999). The literature findings based on studies between the mechanistic link between T2DM and AD with respect to insulin action in the brain are inconclusive (Han & Li, 2010; Takeda et al., 2010). Several lines of literature evidence have directed me to a hypothesis that impairment in insulin availability and signaling in the brain is a consequence, rather than a cause, of AD pathology. Therefore, my Ph.D. thesis pertains to a study of distribution of the insulin hormone in brains displaying an Alzheimer's disease (AD) phenotype. It also delineates the transport and signaling mechanisms by which the biomarkers in AD affect insulin transport across the blood-brain barrier (BBB). Below, I shall outline the structure of my research models and then, provide an overview of my findings obtained by addressing my research questions.

AD is characterized by an increased accumulation of amyloid-beta (Aß) peptides, which are breakdown products from the amyloid precursor protein (APP) expressed in neuronal cells. (Swaminathan et al., 2017) recently proved that insulin regulates clearance of Aβ peptides from the plasma to brain and vice versa. It is common knowledge that in healthy individuals, insulin is an anabolic hormone which regulates the rate of glucose metabolism, cell proliferation, growth, lipid metabolism and cognition. However, research from the last decade

has shown that brain insulin levels in AD patients at progressive stages of the disease are significantly reduced relative to age-matched control brains. Moreover, insulin resistance is associated with AD pathology. Intranasally-delivered insulin helps reduce brain deposits of Aß and alleviate cognitive decline. However, it is speculated that brain insulin resistance may have homeostatic mechanisms which may counteract the positive outcomes stemming from the chronically elevated levels of CSF insulin obtained after intranasal delivery of insulin (Freiherr et al., 2013). In fact, (Stanley et al., 2016) have recently found no correlation between peripherally administered insulin and cerebral insulin in AD transgenic mice. In their discussion, they emphasized the need to understand the physiology relating peripheral levels of the hormone to brain levels. It is therefore important to identify and understand the physiological barriers to insulin action in the brain. This will assist in the construction of physiologically inclusive transport models which predict development of resistance to insulin action. Tailoring various disease and system-specific parameters in the model will then help regulate treatments aimed at increasing its availability in the brain parenchyma and facilitating improvements in cognition and Aß clearance.

I have been investigating distribution of administered insulin in AD brains, by employing Aß peptide over-producing transgenic mice (APP/PS1) and age-matched wild-type (WT) mice. My group employs Single Photon Emission Computed Tomography coupled with Computed Tomography (SPECT/CT) to dynamically image the kinetics of radiolabeled peptides in mice. With help of this

technique, I studied the plasma-to-brain and brain-to-plasma kinetics, and overall accumulation of insulin into brain regions and peripheral organs in the above groups of mice. This was achieved by administering ^{125}Iodine-labeled insulin into the femoral vein, internal carotid, or right hippocampus, followed by tracking the radioactivity in the brain within the time frame of insulin activity, which is typically between 20 to 25 minutes. I discovered that APP/PS1 mice brains accumulate lesser quantities of administered insulin. Surprisingly, brain counts were lower in APP/PS1 brains due to a slower rate of uptake and a faster rate of radioactive decline from the brain, as compared to WT mice. This led me to a hypothesis that Aß40 and Aß42 interfere with insulin transport into the brain parenchyma. Based on this work, our group, along with collaborators at Mayo Clinic, has initiated the development of ^{68}Ga-labeled insulin as a PET tracer to validate my findings in human patients.

Now, the mechanistic details underlying decreased insulin transport into the brain is not yet available, which is the focus of my investigation. To accomplish this goal, I constructed a physiologically-based compartmental model using Stella© to simulate the kinetics of insulin in brain regions affected in AD. Intriguingly, I observed that the rate-limiting step to availability of insulin in the brain was its transport across the BBB, subject to the extent of Aß peptide load. Since it well known that transport of insulin into the brain is contingent upon insulin receptors (IR) expressed at the BBB endothelium, I hypothesized that Aß40 and Aß42 impair the signaling and transport processes of insulin at this juncture. There is strong evidence that the BBB or neurovascular unit is a key contributor to the

cascade of neurological damage. The BBB is a critical portal by which systemic insulin is delivered to brain and previous publications have underscored its significance in accumulation and clearance of Aß peptides, Aß40 and Aß42, the primary biomarkers of AD (Storck et al., 2016) (Mackic et al., 1998). The cerebrovasculature, a component of the BBB, is understood to be a significant portal for the clearance of Aß peptides.

I tested my hypothesis through two 'arms'. In the first arm, I investigated whether Aß peptides causes any changes in the sequential processes of binding, IR-mediated uptake, IR recycling, and insulin transcytosis across the BBB. I probed these events using flow cytometry, fluorescence recovery after photobleaching (FRAP) and permeability assays with radiolabeled insulin, respectively. Here, I employed cell-culture based BBB models since mechanistic experiments are extremely challenging to conduct in humans or mouse models. I utilized human cerebrovascular microendothelial cells (hCMEC) as a model, following characterization of its barrier integrity and transporter expression. Since hCMEC did not display adequate downstream activation of signaling events in the Akt pathway in response to insulin treatment, I over-expressed hCMEC monolayers with insulin receptors (IR) to elicit sustained activation.

Binding of insulin to hCMEC monolayers was not affected by pre-incubation with Aß peptides. Intriguingly, I discovered that Aß40 and Aß42 significantly inhibit the steady-state reversible uptake of insulin into hCMEC, with the Michelis-Menten parameters pointing to a mechanism of uncompetitive inhibition. Further, the permeability of insulin was significantly reduced across the hCMEC monolayer, in

presence of Aß40 and Aß42. When I tracked the mobility of GFP-tagged IR on the surface of hCMEC through spinning-disc confocal microscopy, I could clearly differentiate between clustering of IR on the cell surface (in response to insulin treatment) and clustering in the intracellular space (in response to insulin treatment following Aß peptide incubation). These images were corroborated by detailed FRAP assays which helped identify that half-lives of IR exocytosis and lateral diffusion were lower in response to insulin alone, rather than in response Aß peptide pre-incubation.

In the second arm, I probed the effect of Aß peptides on regulation of receptor tyrosine kinase signaling networks, phosphorylation cascades of which are postulated to influence the phenotypic actions of insulin. To do so, I first investigated the impact of insulin on the downstream receptor tyrosine kinase signaling, based on a hypothesis that intracellular trafficking of insulin at the BBB endothelium affects receptor tyrosine kinase signaling. Our collaborators initiated work in this direction by setting up a database of the genomic architecture of the BBB http://bioinformaticstools.mayo.edu/bbbomics/. So, following on the lead, I conducted a Reverse Phase Protein Array analysis of hCMEC/D3 cell monolayers treated with either insulin alone, or insulin following pre-incubation with Aß40 and Aß42. The results displayed changes in phosphorylation of proteins expressed in the mitogenic (MAPK) and metabolic(PI3K) arms of insulin signaling, as a consequence of Aß peptide exposure. These led to a conclusion that Aβ peptides interfere with mitogenic and metabolic motifs of insulin signaling. Studies with finer detail are however required, to test an association between

insulin-mediated signaling and its transport. Results obtained from them will be crucial to determine whether rectification of impaired signaling motifs will enhance its transport into the brain parenchyma in AD, or vice-versa.

The following segments will provide a detailed background for areas associated with this nexus between AD, T2DM and insulin transport.

1.2 Alzheimer's disease:

1.2.1 Classification of AD**:** AD is a degenerative mental disorder affecting more than 35 million people in the world every year. It represents the 6th leading cause of deaths in the United States (Alzheimer's, 2016). It accounts for the most percentage of dementia-related neuropathologies, amongst cases such as primary age-related tauopathy, frontotemporal dementia, tangle predominant dementia, non-Alzheimer disease tauopathies, parkinsonism, Lewy body disease and multiple system atrophy. AD could manifest early or late in a person's lifetime, in either a familial or sporadic manner. Persons developing AD before the age of 60 are grouped as early-onset patients whereas those above 60-65 years of age are grouped under the late-onset category. Though there might be several subtypes on the AD spectrum due to early-onset cases which remain undiagnosed, it is now recognized that there exist as many as four subtypes of AD, depending on the basis for inheritance.

Familial form of AD is responsible for 5% of AD cases whereas sporadic AD (LOAD) accounts for 90-95% of AD cases. The familial form of AD is associated with a variation in the expression of three genes. The genes which are most studied are amyloid-precursor protein (APP), presenelin 1 (PS1), presenelin 2 (PS2). Mutations in APP and PS1 lead to phenotypes which are prevalent in distinct populations around the world. Diagnosis of mutations in APP or PS1 guarantees the development of AD symptoms, at least 10 years before its onset in people who do not possess those mutations. It is important to note that the familial form of AD accounts for <1% of diagnosed AD cases.

Sporadic AD does not develop due to a specific familial link, rather its etiology may be imputed to a complicated interplay between genes, ageing process, lifestyle and the environment. Certain genes may increase the susceptibility to AD, therefore they are known as susceptibility genes. Apolipoprotein E (ApoE) is a gene which constitutes a major risk factor for late onset sporadic AD. Two copies of the ApoE4 allele increases the risk for AD by 1200% whereas a single copy of the allele increases the risk for AD by 370%. Genome-wide association studies and meta analyses have recently identified at least 20 susceptible genes for AD (Van Cauwenberghe, Van Broeckhoven, & Sleegers, 2016). The ageing process is marked by brain lesions and inflammation, shrinkage of the brain areas associated with planning, execution and memory, and neuronal death, all of which are characteristic early-stage symptoms of AD. Vascular disorders, depression, cerebral injuries etc are strongly associated with the subsequent onset of AD symptoms. Sporadic AD accounts for more than 95% of AD cases.

1.2.2 Clinical manifestation: AD progression is typically associated with a steep decline in cognitive function and performance of physical activities, which ultimately leads to incapacitation and untimely death in advanced stages of disease. AD progresses through three stages, namely, early, moderate and late-stage. Progress of the disease symptoms differs from patient to patient. Clinical symptoms begin to surface 4-5 years before the detection of Aβ plaques and tau tangles, whose accumulation in the brain is the hallmark of AD neuropathology. The initial signs of cognitive decline include forgetting names of people, locations and addresses. Language is an area of communication which is known to be

hindered in people who are at a significant risk for developing dementia. There have been numerous cases of people-at-risk depicting lapses in the ability to construct sentences with appropriate grammar or convey meaning through conversation. These tell-tale signs lead to a worsening in performance of activities of daily living such as speaking, reading, writing, eating, cleansing and maintenance of personal hygiene. A precipitous decline in performance of the above activities is correlated with increased detection of plaque accumulation in the brains of AD patients.

1.2.3 Biochemical manifestation**:** Brains of individuals affected by AD are characterized by the presence of Aß plaques in the extracellular space and neurofibrillary tangles in the intracellular regions. Aβ peptide, a characteristic hallmark of AD, is a cleavage product of a naturally occurring glycoprotein called the amyloid-precursor protein (APP). APP is abnormally cleaved in a sequential manner, first by beta secretases, which separate the ectodomain of APP from the transmembrane domain, and then by a gamma secretase complex which cuts the C-terminal fragment within the transmembrane domain to produce Aß peptides of varying length of amino acids. The gamma secretase complex, then employs presenelin-1 to further cut the transmembrane domain into peptides, predominantly Aß40 and Aß42, consisting of 40 and 42 amino acids, respectively. Aß40 is understood to be less pathogenic than Aß42, which has a higher propensity for accumulation in the extracellular spaces of the brain. The ratio of Aß40 to Aß42 in AD patients reflects changes in Aß peptide metabolism and serves as a measure to differentiate between AD and other forms of

dementia, such as vascular, Lewy Body or frontotemporal dementia. (Spies PE et al, Current Alzheimer's research). An increase in the Aß42 to Aß40 ratio is strongly correlated with the severity of the disease in early-onset AD (www.alzforum.org/mutations)

Tau tangles are produced due to several mechanisms, which include an excessive phosphorylation of microtubule-stabilizing tau proteins, mutations in the tau genes or aberrant degradation of tau proteins. The tangles are disposed to accumulate within neurons and glial cells. They assume the shape of elongated strands of protein within cells and spread through the brain tissues when tau species released into the interstitial fluid are internalized by surrounding neurons (Clavaguera et al., 2009). Regions of the brain such as the hippocampus, entorhinal cortex, amygdala, cerebellum and brain stem acquired from post-mortem AD patients, have shown to harbor abnormal amounts of tau tangle deposits. The presence of these deposits causes the respective regions of the brain to atrophy and form significantly more gyri and sulci as the disease progresses.

(Braak & Braak, 1991) introduced a staging system to categorize the development of neurofibrillary tangles and plaques in the brain, characteristic markers of AD. Braak stages I and II indicate presence of tangles and plaques in trans-entorhinal regions of the brain. Stages III and IV refer to the involvement of the limbic system in progression of tangles and plaques, while Stages V and VI indicate their distribution in the neocortical system. Plaques and tangles in the brain are theorized to spread from one dysfunctional cell to another and

subsequently, from one Braak staged- anatomical region to the next, culminating in a network of apoptosis and regional atrophy. (Spires-Jones, de Calignon, Meyer-Luehmann, Bacskai, & Hyman, 2011)

Aβ plaques begin to deposit in the aforementioned areas in the early stages of AD which persists for 3-5 years. Plaque presence is associated with initial clinical symptoms such as declining ability to plan, decide, remember or physically execute.

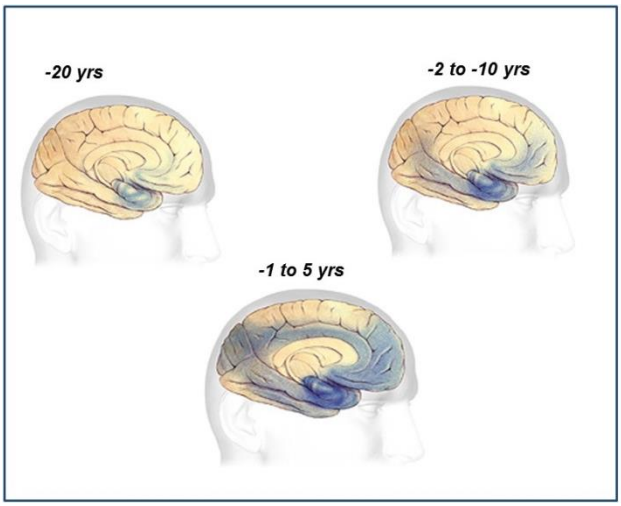

Figure 1.1. Schematic depicting the progression of amyloid plaque in the brain at three stages i.e. 20 years, 2 to 10 years and 1 to 5 years before the onset of clinical symptoms.

The clinical endpoints associated with Aβ peptide deposits include but are not limited to neuronal degeneration, shrinkage of brain regions, and impairment of energy metabolism, factors which govern learning, memory, thinking and planning,

Interestingly, a seminal study conducted in 2010 indicated that it is the clearance and not an accumulation of Aβ proteins which influences the clinical effects of AD, pointing to the fact that Aß peptides are endogenous to the brain

(Mawuenyega et al., 2010). The clearance of Aβ peptides from the blood-brain barrier as well as affected regions of an AD brain such as hippocampus, entorhinal cortex and amygdala is known to decrease as the disease progresses, until the clearance reaches a low steady state level. Thus, researchers are attempting to develop agents to track Aβ plaques in a more accurate and non-invasive manner. PET agents which have been deployed to trace Aβ plaques in AD brains are Pittsburg compound etc. The dynamics of Aβ peptide clearance at tissue junctions in the periphery and the brain remain to be mapped with respect to the progression of pathological symptoms.

Curiously, current biomarker assessments at various stages in AD such as volumetric MRI, amyloid PET do not align well with the disease progression or the clinical endpoints. They also do not associate well with any changes in the disease pathology. These are arguments which have been raised against the hypothesis that amyloid proteins are the primary biomarkers of AD. One of the points of contention by the ‘Tau theorists’ is that neurofibrillary tangles correlate much better with cognitive impairments than amyloid proteins. In their defense, amyloid beta theorists assert that amyloid plaques begin to surface years before the detection of clinical symptoms and are instrumental in gradual biochemical and signaling defects in the neurons. The other point of contention by tau theorists is that normal cases (not displaying AD-like symptoms) also possess plaque deposits in the brain as found through post-mortem analysis. Amyloid theorists counter this assertion by explaining that amyloid deposits in normal

cases have a propensity to sequester oligomeric forms of non-diffusible forms of Aβ peptides in a relatively less toxic state.

It underscores the need to develop more dynamic biomarkers at early stages of the disease. Therefore, PET agents which bind to neurofibrillary tangles are being researched as the more promising trackers of AD progression.

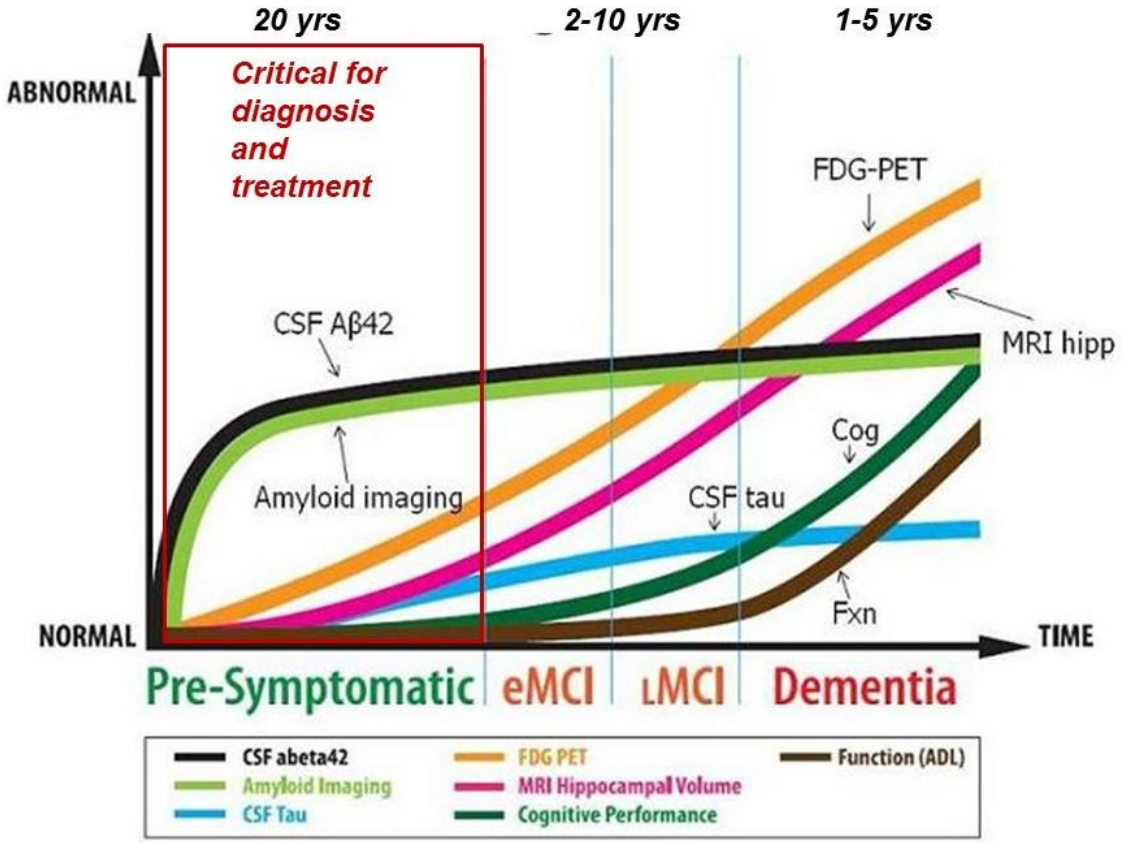

Figure 1.2. Schematic depicting the progression of stages in AD on the y-axis and the severity of biomarker progression on the x-axis.

1.3 Blood-brain barrier and its importance in AD

The BBB is a neurovascular interface consisting of capillary endothelial cells, astrocytes and pericytes. It can be visualized as a group of endothelial and

perivascular cells interacting with the astrocytes and neurons. The endothelial cells contain tight junctions and adherens junctions and lack fenestrae unlike those expressed in capillaries lining the peripheral organs of the body. It also contains low level of pinocytes. The BBB vascular system is developed from the CNS tissue through a gradual increase in density of expression of pro-angiogenic factors such as vascular endothelial growth factor (VEGF-1) and fibroblast growth factor (FGF) (Bautch & James, 2009). Following vascular development and differentiation, there is an asymmetric distribution of receptors and molecular transporters. These elements pose a significant layer of fortification which prevents the passage of water-soluble solutes and molecules lesser than 4000 daltons in size, across the BBB interface. The neurovascular unit thereby maintains optimal and stable brain cell function, blood flow, immune function and homeostasis.

Greater than 98% of vessels at the BBB are covered by astrocytic endfeet. The endfeet sense synaptic activity and communicate to the vessels to induce a supply of micronutrients. Astrocytes assist in the induction of tight junction properties of the BBB endothelium. This was evidenced by a study which proved that astrocytes cultured onto leaky vessels reduced their leaky nature. Astrocytes or glial cells also facilitate receptor-mediated signaling initiated from the BBB endothelium, as shown by experiments set up to measure the release of intracellular calcium from glial-endothelial co-cultures. The astrocytes also release certain chemicals which influence the permeability of the BBB endothelium. This aids in transient opening the BBB endothelium to modulatory

chemicals present in the plasma. This is postulated to be of advantage for the regulatory function of the brain, as the exposure of these chemicals to neurons helps the brain maintain immune and homeostatic control over the body (Abbott, 2002).

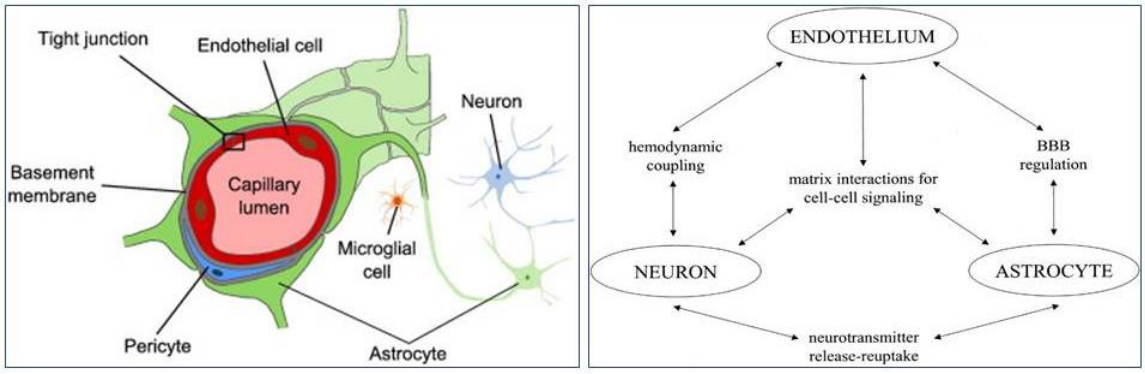

Figure 1.3: Schematic representation of the top-view of the neurovascular unit and physiological functions of its components**.** The schematic on the left depicts the unique characteristics of the neurovascular unit such as presence of tight junctions, basement membrane, endothelial cells, periyctes, astrocytes, microglial cells and neurons. The schematic on the right explains the connections between the endothelium, neuron and astrocytes in relation to the phenotypic processes regulated by them.

Pericytes are another critical component of the BBB since the permeability of the BBB endothelium is compromised when pericytes are ablated (Armulik et al., 2010). Pericytes are therefore required to maintain a steady flux of nutrients between the blood and the brain parenchyma. They also affect the gene expression in endothelial cells. They also help in maintaining the neurovascular coupling initiated by astrocytes by steadily regulating the polarization of astrocytic endfeet.

The pathways of molecular transport across the BBB endothelium are the paracellular pathway, transcellular pathway and transport protein mediated

pathway. Paracellular transport is restricted across the BBB endothelium due to the presence of tight junctions which exhibit a trans-endothelial electrical resistance of 1000-5000 Ω-cm^2 as compared to 3-33 Ω-cm^2 in other tissues (Butt, Jones, & Abbott, 1990). Transcellular passageways allow for the transport of molecules exhibiting lipophilicity greater than a certain threshold value. Receptor-mediated transcytosis represents a source of selective uptake of molecules such as ligands, hormones, enzymes, proteins and lipoproteins. Receptor-mediated transport is facilitated by members of the solute carrier family (SLC) of transporters, which include receptors for insulin, low-density lipoproteins (LDL) and transferrin. The insulin receptor is an important tyrosine kinase receptor expressed by the BBB (Duffy & Pardridge, 1987), which has relevance to the upcoming BBB pathology-related discussions in this thesis. The BBB also expresses molecules capable of transporting molecules out of the endothelium. These molecules, known as efflux transporters, consist of ATP-binding cassette (ABC transporters) and multidrug resistance associated protein (MRP) (Davis Lab, University of Arizona).

In AD, the BBB loses the integrity of structural properties of the barrier. We gauge a measurable impact of the BBB on AD progression from results of a recent paper (van de Haar et al., 2016), wherein the aim was to noninvasively investigate two functional elements of the neurovascular unit linked to each other i.e. BBB permeability and cerebral blood flow (CBF), in patients with early AD compared to healthy controls. Both dynamic contrast-enhanced magnetic resonance imaging and arterial spin labeling magnetic resonance imaging were

applied to measure BBB permeability and CBF, respectively. Dynamic MRI analyses conducted on brain capillaries of mild cognitively impaired (MCI) patients proved that functional aspects of BBB integrity such as the vascular volume, grey matter voxels, permeability were significantly modulated as compared to normal patients. The MCI patients showed significantly lower CBF and local blood volume in the gray matter, compared with controls. In the MCI patients, they also discovered that a reduction in CBF is correlated with an increase in leakage rate. This finding supports the hypothesis that neurovascular damage and impairment of the neurovascular unit constitutes the pathophysiological link between CBF reduction and BBB impairment in AD. Consequently, the BBB vasculature of AD patients does not exhibit the high TEER value of non-demented patients and becomes vulnerable to the influx and efflux of toxins. The authors of the study posited that lapses in BBB integrity in MCI patients could be due to the surrounding presence of Aß plaques in the MCI brain.

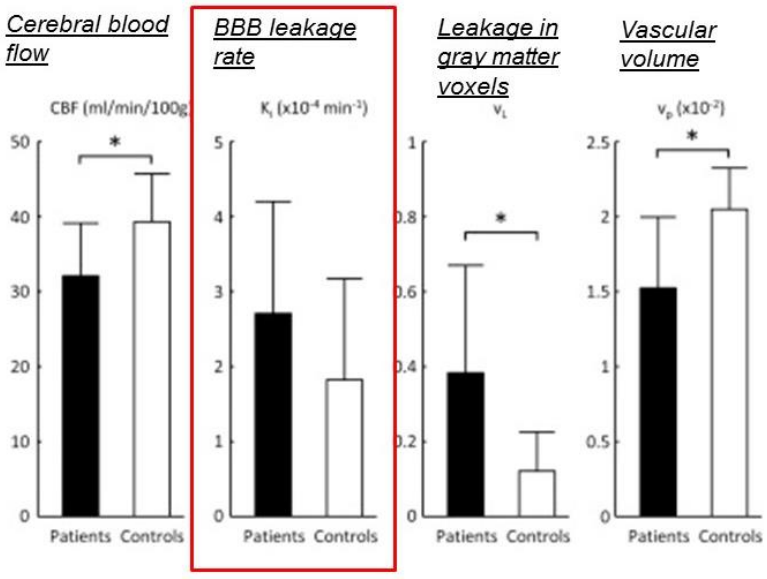

Treatment groups:

1. *7 AD and 7 MCI patients (mean age-75.3 yrs)*
2. *16 healthy controls (mean age-76.4 yrs)*

Figure 1.4: Published figure proving the role of the BBB through MRI studies in AD patients. Based on contrast-enhanced MRI analysis. (van de Haar et al., 2016) outlined differences in cerebral blood flow, BBB leakage rate, leakage in gray matter voxels and vascular volume between AD patients and controls.

Indeed, the clearance of Aß peptides from the brain involves the normal functioning of the blood-brain barrier. (Winkler et al., 2015) also discovered that the glucose transporter, GLUT1, is scarcely expressed in mice over-expressed with Aß protein which results in decreased clearance of Aß proteins and reduced vascular function. This, combined with an earlier discovery by (Mawuenyega et al., 2010) that Aß proteins exhibit a reduced clearance from the brains in AD patients, points to a role of impaired BBB transport proteins in the clearance of Aß deposits from the brain.

1.4 Pathological connection of AD with T2DM

LOAD is a neurological disorder which is understood to manifest due to the influence of lifestyle choices on the appropriate genetic framework and metabolic functions within an individual. It is a disease which evolves due to a system of interconnected pathways and organs.

LOAD and Type-2 diabetes (T2DM) share common risk factors such as obesity, oxidative stress, physical instability and predisposition to genetic causality. Besides, there have been several epidemiological studies suggesting congruence between these two diseases (Bosco, Fava, Plastino, Montalcini, & Pujia, 2011). Type-2 diabetes is characterized by abnormal glucose metabolism which develops as a result of variations in tissue response to insulin action. T2DM is also characterized by amyloid deposits in the islet cells (IAPPs) of the pancreas. It is a major cause for obesity and age-related metabolic disorders.

Research over the past decade and a half has proven that T2DM, in fact, is correlated or forms a precursor to a host of neurological disorders such as stroke, dementia, Parkinsons's disease etc. Now, LOAD brains display decreased insulin-dependent energy metabolism, as revealed by PET scans conducting using fluorodeoxyglucose as a marker. Since insulin resistance is a precursor to T2DM, sporadic AD and insulin resistance are correlated.

A considerable amount of research has been directed at delineating signaling pathways involved in LOAD progression within the brain. Early research in the field has linked age-dependent brain insulin reduction with sporadic AD progression. This correlation between AD, T2DM and insulin dysregulation was started to be researched in the late 1990's during which, insulin signaling and glucose utilization by the brain was studied after intracerebroventricular injections of streptozotocin (to induce T2DM) in mice (Ding, Nitsch, & Hoyer, 1992; Duelli, Schrock, Kuschinsky, & Hoyer, 1994; Grunblatt, Salkovic-Petrisic, Osmanovic, Riederer, & Hoyer, 2007; Lannert & Hoyer, 1998; Plaschke & Hoyer, 1993; Plaschke et al., 2010). They discovered that the uptake of insulin in the brains of those mice was lowered and on further probing, observed that the amount of insulin receptors in the brain was reduced. Much of the recent focus has been toward establishing the role of brain insulin dysregulation on amyloid accumulation and consequently, LOAD symptoms.

Physiologically, insulin resistance progresses vis-à-vis several cardiovascular and neurovascular complications such as atherosclerosis, stroke and AD. (Banks, Owen, & Erickson, 2012) reviewed the pathophysiology of insulin

resistance and AD with a focus on factors that modulate insulin signaling. They recognized intranasally administered insulin as an effective strategy to overcome AD-associated cognitive decline. In discussing potential causative factors for insulin resistance in the brain, the author implicated the phenomenon of attenuated transport of insulin across the BBB as a likely factor, amongst other factors such as low expression of insulin receptors and insulin, for deterioration of the neuropathology. In (Heni et al., 2014), evidence for modulated insulin transport into the brain was reviewed. Based on results from oral glucose tolerance tests which indicated reduced CSF/plasma ratios of insulin in insulin resistant subjects, the author asserted that availability of insulin in the CSF is related to its sensitivity in peripheral tissues. This association, in fact, is surprisingly unexplored in insulin resistance research. The author's conclusion, however, is a broad hypothesis about the systems impact of insulin resistance. (Banks et al., 2012) also hinted at the hitherto unexplored connection between peripheral and central insulin resistance and added that fluctuations in insulin sensitivity in different tissues might be independent of each other. It underlines the suggestion that the intracellular treatment of insulin varies depending upon the nature of the tissue it is exposed to. Through his discussion, he proposed that it is the counter-regulatory functions of the BBB which are responsible for the varying central and peripheral effects of hormones such as insulin.

Based on the above reports from the past few years, we can see that there is a surge in BBB and insulin resistance research, focused toward markers for BBB integrity, whilst hinting at altered blood-to-brain transport routes for insulin.

Now, based on results from (Azizi et al., 2015), insulin disposition in peripheral vasculature differs from its disposition in central vasculature. Its uptake in limited by the surrounding vasculature but the mechanism of its receptor-mediated internalization varies, for e.g. in the adipose vasculature, it is taken up by a clathrin-mediated endocytic process, whereas in muscle and aortic endothelial cells, it is taken up by a caveolae mediated process. These conclusions have been derived based on confocal and Total Internal Reflection Fluorescence (TIRF) microscopy studies designed to track insulin uptake and exocytosis, respectively, in endothelial cells. Although experiments in these publications are designed to distinguish between uptake processes at the endothelium, they do not explore downstream vesicular machinery that could be involved in insulin transport and exocytosis to the basolateral end. Further, (H. Wang, Wang, Liu, & Barrett, 2008) have delineated the effects of insulin signaling on insulin uptake, but whether the uptake leads to transcytosis was not examined in their publication. Intracellular ligand and receptor transport and ligand exocytosis are two phenomena which need to be studied in order to define the target site entrance and distribution of insulin. The spatial and temporal kinetics of insulin receptor transport within the cell are key regulators of the intracellular transport of insulin.

Literature accrued on insulin resistance in diabetes over the last few years (Dorrance, Matin, & Pires, 2014) pertain to the effect of insulin resistance on cerebrovascular dysfunction. Specifically, the markers for effective endothelial functioning pertain to structural changes which are contingent upon cerebral

blood flow, nitric-oxide-mediated vasodilation, blood pressure etc. These vascular changes are eventually correlated to pathological observations in dementia.

1.5 Insulin

Insulin is an anabolic hormone secreted by the pancreas in response to increased blood glucose levels. It is produced by beta cells of the islets of Langerhans in the pancreas. The structure of insulin consists of an A and B peptide chain linked together by disulfide bonds. The beta cells, which constitute 60-80% of the cells in the islets of Langerhans, initially generates the A and B insulin polypeptide chains as a merged, single polypeptide chain known as preproinsulin. In the endoplasmic reticulum of the beta cells, the preproinsulin is incised to remove a signal peptide to form pro-insulin. Pro-insulin migrates to the trans-golgi network wherein it matures to insulin through the assistance of prohormone convertases and an exoprotease known as carboxypeptidase E. Cleavage results in the removal of a C-peptide fragment and a remainder of the A and B chained joined by 2 disulfide bonds.

When glucose binds to the GLUT transporters on the surface of the cell, it is phosphorylated to glucose-6-phosphate (G-6-P). Thereafter, G-6-P enters the Krebs cycle, following passage through the glycolytic cycle, to produce ATP. The ATP:ADP ratio within the cell rises, thereby depolarizing the cell. Depolarization induces the influx of calcium ions into the cell. An increase in calcium storage triggers the release of insulin from the secretory vesicles. This results in exocytosis of insulin from the cell following stimulation with glucose, leucine,

mannose etc. Incretin hormones such as glucagon also regulate the exocytosis of insulin. Glucagon-like-peptides are utilized to induce the release of insulin.

Kinetics: Endogenous insulin secretion into plasma occurs in a pulsatile manner, regulated by blood levels of glucose. Insulin released from the pancreas exists in form of hexamers. Typically, insulin levels range from 6 pg/ml to 10pg/ml in a fasting adult. It has proved difficult to measure the secretion of endogenously secreted insulin. Glucose levels in the blood are therefore used as a surrogate marker of insulin secretion. Insulin administered exogenously into the subcutaneous tissue passes from the injection site into the interstitium before entering the blood space (Wilinska et al., 2005). Oligomeric forms of insulin act slower on tissues as opposed to monomeric forms which are considered to be fast-acting. Removal of insulin from the blood has been shown to assume linear kinetics, according to many models established heretofore. Some models have displayed Michelis Menten kinetics, albeit through employment of concentration intervals which are narrow in range. In-vivo models have therefore not adequately delineated the transport of insulin through various compartments following its passage through plasma. Also, most models have also not accounted for the interactions on insulin with insulin receptors in these compartments (Hovorka & Hilgertova, 1991).

Apart from regulating peripheral glucose metabolism and normal feeding behavior, insulin is understood to effect lipid metabolism, cell proliferation and normal functioning of cognitive processes in the brain. Its synthesis by the brain, however, remains unresolved, amidst reports that insulin mRNA is expressed in

certain regions of the brain. Systemically available (i.e. in the plasma) insulin, similar to other macromolecules, gets transported into the brain, a highly perfused organ. Partridge et al have shown that ^{125}I labeled insulin injected into rabbits via the internal carotid artery crosses the blood-brain barrier endothelial cells through an insulin receptor-mediated endocytic process. It was one of the first studies to prove that the insulin receptor expression is essential to insulin transport across tissues.

1.5.1 Insulin receptor

The insulin receptor is a tetrameric glycoprotein consisting of two alpha and two-beta subunits. Insulin receptors are expressed either on the surface of the cell or in the intracellular regions of the cell. The alpha subunit is expressed extracellularly whereas the beta subunit is present within the cytoplasm and it possesses tyrosine kinase activity (Goldfine, 1987). The insulin receptors are synthesized and degraded in a manner similar to other cell membrane proteins. The receptor protein is synthesized following the replication and transcription of the insulin receptor gene. The receptor has two isoforms which are produced due to differential splicing of the insulin receptor gene (INSR). The two isoforms, A and B, influence the strength of consequent binding of insulin to the receptor. Isoform B includes exon 11 and is associated with stronger insulin binding whereas isoform A, which excludes exon 11, binds with both insulin and insulin-like-growth factor (IGF-2). Variations in alternative splicing of INSR leads to differences in the relative expression of isoform A versus isoform B in different cell types within the body. These differences in ratios of IR-A versus IR-B are

strongly correlated with different disease states, such as insulin resistance, cancer or myotonic dystrophy (Malakar et al., 2016).

Following synthesis of the respective receptor isoforms, IR is transported to the surface of the cell membrane either independently or as a result of ligand-mediated stimulation of signaling pathways within the cell. On the plasma membrane, IR moves laterally to facilitate better interaction with ligand molecules. This signals the beginning of a transport cycle wherein the cell surface IR is then internalized after binding with ligands. The internalized receptor complex dissociates from the ligand within the cell. The dissociated IR is then either recycled back to the cell surface or degraded. The kinetics of this transportation process wherein, IR is either exocytosed to the surface, or moved laterally on the cell surface, dictates the fate of the insulin ligand and subsequent downstream developmental and proliferation processes in the cell.

It is known that the endocytic trafficking of receptor tyrosine kinases affects the downstream signaling of ligands. The intracellular sorting of the ligand-receptor complexes is influenced by post-translational modifications to proteins in the sorting pathways. Variations in the phosphorylation of endosomal proteins affect the regulation of receptor entry and exit through the endosomes. For instance, it is known that the epidermal growth factors are internalized and depending upon their localization of specific endosomes, the signaling activity of the cell is modulated.

1.5.2 Transport pathways of insulin into the brain

The blood-brain barrier is a neurovascular interface which regulates the passage of essential nutrients, hormones, solutes to and fro from the brain. It consists of brain capillary cells which contain tight junctional proteins preventing the transfer of molecules above a certain size range and lipophilicity. The brain capillary cells do not comprise of as many pinocytotic vesicles as peripheral cells, but internalize molecules through caveolin, clathrin or macropinocyte-mediated endocytosis (Preston, Joan Abbott, & Begley, 2014). Insulin binds to tyrosine kinase receptors on the surface of the capillary endothelial cells. The bound insulin causes the insulin receptor substrate protein to attach to the insulin receptor complex. This, in turn, phosphorylates a series of second messenger molecules, finally leading to the phosphorylation of protein kinase B (Akt). The activation of Akt triggers the translocation of GLUT1 receptors to the cell surface. It also leads to the activation of transcriptional factors that result in gene expression and cell proliferation over a period of several days.

After being internalized, the receptor-ligand complex traverses the early, mid and late endosomes. Phosphorylation events of appropriate second messenger molecules occur in tandem as the receptor-ligand complex travels through the endosomal compartments. The internalized insulin is either directed toward acidic compartments of the lysosomes or dispatched further away from lysosomes into the directionally opposite end of the luminal surface i.e. the abluminal surface. However, the vesicular path traversed by insulin in its exocytic journey still remains unresolved due to insufficient resolution rendered through

fluorophore-based imaging, despite advances in two photon and total internal reflection microscopy. The receptor-ligand complex dissociates and the receptor is eventually recycled back to the plasma membrane. The only details discovered thus far describe the role of Rab GTPases in the insulin exocytosis to the cell surface (Ljubicic et al., 2013). The BBB endothelial surface, however, has a significantly higher expression of GLUT1 receptors, known to be involved in the transcytosis of glucose across the BBB. Whether insulin is a pre-requisite to the normal functioning of this process remains unclear. Recently (Sajja, Prasad, & Cucullo, 2014) showed that the integrity of tight junction proteins and nutrient transporters at the surface of hCMEC/D3 cell monolayers are impaired under altered glycemic conditions. In another review (Yoon, Dang, Chasiotis, Kelly, & Sweeney, 2014), the authors considered altered para-cellular permeability of the vasculature as an important marker for the diabetic phenotype and proposed that aspect as a novel preventative strategy for Type-2 diabetes progression.

Another route through which insulin is administered clinically is the intranasal route. It precludes passage through the blood-brain barrier and thereby, evades systemic exposure. Intranasally administered insulin can be transported either through the intracellular or extracellular route (faster absorption) through the olfactory and trigeminal nerves. It then interacts with the olfactory bulb which are situated in the cribiform plate separating from the upper part of the nasal cavity from the brain. After passage across the cribiform plate, the insulin enters the perivascular spaces of the brain’s blood vessels through the subarachnoid spaces (Rosenbloom et al., 2014).

1.6 Conflicting evidence related to insulin dynamics in AD

Over the past two decades, about 25-30 papers have studied parameters associated with insulin action with respect to an AD phenotype. The dynamic parameters assessed in relation to AD include the extent of blood insulin, CSF insulin and insulin receptors in specific regions of the brain. Parameters related to insulin signaling include the extent of brain p-AKT signaling, brain p-IR, brain IRS-1, brain p-IRS-1, brain GSK-3, brain p-GSK-3, brain p-JNK. A review by (Stanley et al., 2016) has comprehensively reviewed the above parameters in respective publications and charted variations to those parameters in AD.

Insulin levels in the blood have consistently been shown to be increased in AD patients. A few studies have proved that CSF levels of insulin are increased in AD patients while some other studies have proved the converse of this finding. (Molina et al., 2002) have discovered that there is no change in insulin levels in the CSF. Similarly, (Stanley et al., 2016) have succinctly classified findings in the field per variations in brain IR, and molecules of the insulin signaling pathway such as Akt, pAKT IRS1, GSK3 etc.

Stanley et al also raised many important questions regarding the quid pro quo between T2DM and AD, which are heretofore unanswered. The implications of one aspect of this pathogenic exchange will be addressed in this thesis by attempting to answer questions related to the influence of AD on T2DM characteristics.

1.7 Interactions between insulin and Aß peptides

Numerous papers have documented the effects of hyperinsulinemia on the uptake of Aß peptides in AD brain. There is however, scant evidence regarding

the effect of Aß peptides on systemic brain uptake of insulin. Since the BBB is an important port of insulin brain entry through the systemic side, it is critical to study the mechanistic impact of Aß isoforms on insulin transport through the BBB. The Aß levels are known to be regulated by the insulin degrading enzyme (IDE). Mice deficient in IDE were shown to possess excessive cerebral levels of Aß peptides (Farris, Leissring, Hemming, Chang, & Selkoe, 2005). The IDE is responsible for the regulation of insulin levels, since loss of IDE function in mice has shown to result in excessive levels of insulin.

1.8 Challenges in treatment of AD and T2DM: Therapies for neurological disorders such as AD have been largely palliative and focused on design of small, target-specific molecules. Over the last decade, studies have investigated the potential of stem-cell based therapy in reducing cognitive deficits and reverse synaptic degradation and memory loss in AD. Several growth factors vital for consolidation of long-term potentiation and cognition such as brain-derived neurotrophic factor (BDNF), nerve growth factor(NGF) (Covaceuszach et al., 2009), insulin-like growth factor-1(IGF-1), vascular endothelial growth factor(VEGF) etc. have been screened for delivery into the brain. However, the limited transport of these molecules through the BBB has warranted the development of gene delivery techniques to enhance their efficacy. These efforts have not yielded encouraging results in clinical trials (Bradbury, 2005).

Newer treatments for AD and T2DM employ novel pathways for insulin delivery, notably the intranasal route, in an attempt to preclude intervention by the blood-brain barrier. Clinical trials with intranasal insulin initiated by (Craft et al., 2012)

demonstrate positive symptomatic effects in early stage AD patients, however only at optimum doses of intranasal insulin. These findings are suggestive of functioning insulin receptors in areas of the brain accessible to the olfactory route. Paradoxically, in-vitro as well as in-vivo studies have delineated that Aβ plaques inhibit insulin binding to insulin receptors in major cortical and hippocampal areas, specifically at later stages of AD (Ling, Martins, Racchi, Craft, & Helmerhorst, 2002) (Rivera et al., 2005). This ambiguity in findings can be attributed to a dynamic dose and AD stage-dependent physiological resistance to administered insulin. Due to Aβ plaque-induced degenerative nature of sporadic AD, dose elevation or barrier evasive delivery is not expected to yield therapeutic benefits unless insulin resistance is diagnosed and overturned within a certain time frame and therapeutic window. The solution to increasing brain availability of insulin thus lies in **overcoming brain-barrier resistance at asymptomatic stages of the disease**. It is therefore crucial to understand the mechanistic interactions between AD and T2DM at the BBB to explore robust treatment options. It warrants examination of the BBB permeability and transport characteristics in in-vitro and in-vivo models closely mimicking the pathophysiology of AD.

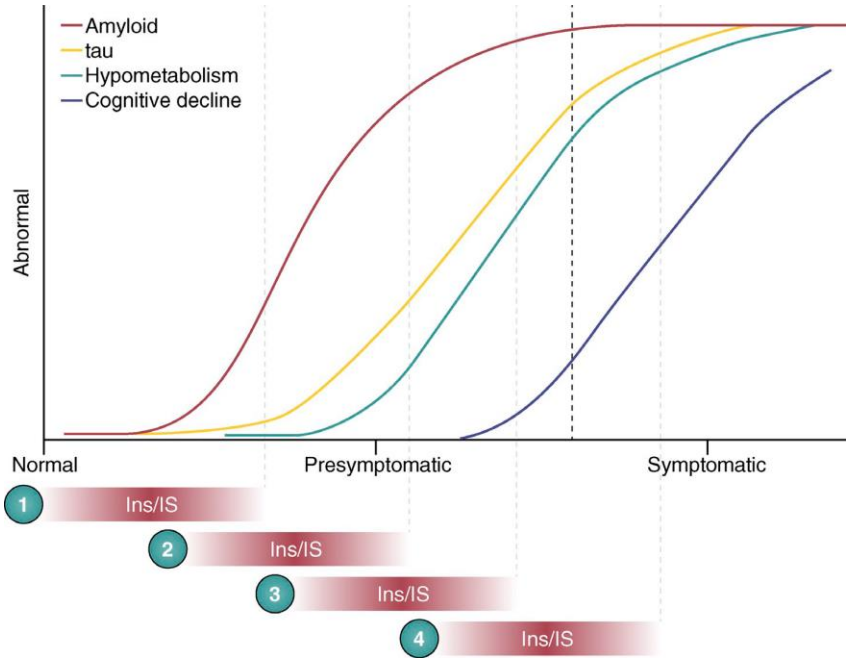

Figure 1.5: Delineation of the temporal relation between insulin levels or insulin signaling and progression of AD pathology. Stanley et al (2016) attempted to explain the stages at which insulin resistance could affect AD or vice versa. They graphed the progression of degenerative markers from normal to abnormal versus the symptomatic timeline in AD. They postulated that an alteration of insulin levels and insulin-mediated signaling at any of the four labeled steps in the schematic, could impact the progression of pathology in different ways. If Ins/IS were to be altered at step 1, it could potentially initiate the accumulation of Aβ plaques. Alternatively, if Ins/IS changes at step 2 or 3, the progression of pathology could be attributed to a feedback loop between impaired Aβ clearance and insulin signaling. Step 4 would indicate that the abnormalities in the biomarker levels in AD lead to an impairment of Ins/IS. In summary, insulin resistance could either be an promoter (step 1), a strong associative factor (step 2, 3), or a product (step 4) of AD progression.

1.9 Rationale

Various kinetic and dynamic measures of insulin distribution have been well examined in tissues encompassing the peripheral system of healthy as well as insulin-resistant physiological systems. These measures have also been documented in the brain in healthy humans and animal models. However, distribution of insulin in the brain relative to the periphery has not been investigated as a function of time and disease severity in AD. A significant

measure of the distribution into the brain viz. transcytosis of insulin across the BBB vasculature has been documented in several publications. However, it has not been studied in context of Alzheimer's disease in-vitro and in-vivo. As described earlier, the BBB endothelium represents a crucial portal for insulin transport into the brain. To graph the effect of amyloid peptides on insulin disposition in the early stages of the diseased brain, it is critical to study transport mechanisms of insulin through the BBB endothelium under the aforementioned disease conditions. This will generate data crucial to understand the consequence of AD on development of insulin resistance. It will assist in answering questions related to the effect of AD on T2DM, thereby help clarify one end of the recursive pathological loop between AD and T2DM.

1.11 Specific aims

The purpose of my thesis is therefore to closely examine the effect of Aβ peptides on insulin transcytosis in models representative of the BBB in early stage AD. My specific aims are as follows:

Specific Aim 1: Measure the rate of insulin uptake and clearance, and the extent of its distribution in the brain in an AD phenotype:

Specific Aim 1a: Study the biodistribution of exogenously administered radiolabeled insulin in APP/PS1 mice and mice which have been infused with excessive amounts of Aβ40 or Aβ42 peptides.

Specific Aim 1b: Conduct Single Photon Emission Computed Tomography to measure the rate of uptake of radiolabeled insulin into the brains of APP/PS1 mice, which are characterized by increased accumulation of Aβ peptides.

Expected outcomes: These in-vivo studies are expected to provide us with a temporal pattern of insulin influx and efflux from the brain, in presence of Aβ peptides. It will also provide us with the fraction of peripherally administered dose which accumulates in various brain regions in APP/PS1 and WT mice. It will help us understand the effects at the given doses, such that the doses for in-vitro BBB models can be titrated accordingly.

Specific Aim 2: **Delineate the effect of Aβ peptides on uptake mechanisms of insulin at the BBB**

The working hypothesis is that Aβ40 and Aβ42 time and dose-dependently inhibit insulin receptor-mediated uptake into the BBB.

Specific aim 2a: *Examine effects of Aβ40 and Aβ42 peptide isoforms on interactions of insulin with insulin receptors in-vitro:* We hypothesize that kinetic parameters of insulin receptor recycling will be modulated in presence of Aβ40 and Aβ42. Confocal fluorescent imaging will be conducted to measure kinetic interactions of insulin with insulin receptors in presence of Aβ40 and Aβ42.

Specific aim 2b: *Study insulin uptake and intracellular trafficking in hCMEC/D3 cells:* Time and dose-dependent effects of Aβ isoforms on insulin uptake will be examined in polarized hCMEC/D3 cells. Flow cytometry will be employed to investigate the cellular uptake of fluorescein labeled Aβ proteins, whereas the trans-endothelial trafficking/itinerary of FITC or AlexaFluor-labeled insulin will be assessed by confocal microscopy.

Specific aim 2c*: Examine transcytosis of insulin across BBB endothelial cells in the presence of Aß40 and Aß42:* To investigate if insulin transport impairment in LOAD brains is due to an elevated exposure of BBB to Aβ proteins, insulin permeability across polarized hCMEC/D3 monolayers will be assessed as a function of exposure time and dose of Aβ40 and Aβ42.

Expected outcomes: The studies proposed in this specific aim are expected to resolve Aß peptide-induced perturbations in

- Kinetics of insulin binding to BBB insulin receptors
- BBB endothelial vesicular trafficking of insulin
- BBB endothelial transcytosis of insulin

Specific Aim 3: Examine effects of Aβ40/42 on insulin-mediated signal transduction at the BBB:

The working hypothesis is that Aβ40 and Aβ42 modulate MAPK and PI3K pathways, which are regarded as the mitogenic and metabolic arms of insulin downstream signaling respectively.

Specific aim 3a: *Investigate impact of PI3K and MAPK pathways on insulin uptake at the BBB*: Differential contributions of PI3K and MAPK pathway to insulin uptake at the BBB will be studied by measuring insulin uptake in the presence of specific pathway inhibitors.

Specific aim 3b*: Identify effect of Aβ peptides on insulin-mediated signaling interactions between MAPK and PI3K pathways at the BBB*: The working

hypothesis, based on literature evidence, is that the Aß peptides will induce differences in insulin-mediated ERK phosphorylation downstream of the MAPK pathway, thereby modulating serine phosphorylation of IRS-1, a marker for insulin signaling impairment at the PI3K pathway. This will be tested through in-vitro Western Blot assays toward ERK and IRS-1 serine phosphorylation as a function of Aß peptide exposure time.

Expected outcome:

We expect to understand the effects of Aß peptides on insulin signaling events associated with impairment to the PI3K pathway. This in turn, is expected to corroborate differences in association, dissociation and receptor internalization rate constants obtained from transcytosis studies in Specific Aim 1. It will support the hypothesis that Aβ40 and Aβ42 affect the mitogenic (MAPK) pathway of insulin to a greater extent than the metabolic (PI3K) pathway, implying modulation of the insulin-mediated growth, differential and inflammatory phenotype.

1.12 Significance

Insulin delivery via the intranasal route may not be a viable strategy for reduction of AD symptoms in the long term owing to the poor and variable absorption of insulin. Moreover, insulin is a growth factor which has multiple physiological targets, hence chronic insulin will have off-target effects. Fundamentally, it is important to ascertain the critical insulin responsive cellular and molecular pathway required for Aß trafficking. Understanding the quid-pro-quo between amyloid-beta peptides and insulin at the blood-brain barrier will answer questions

concerning the relation between the systemic and brain insulin resistance in AD. Only through elucidating these dysfunctions can rational targets for drug delivery be sought. In this work, **the key questions concern the dynamics of insulin transport from systemic circulation into brain via the BBB and the disruption in insulin trafficking caused by Aβ peptides in AD brain**. Importantly, molecular components in the insulin trafficking/signaling pathway that are disturbed by Aβ exposure was identified as well as the perturbed insulin delivery and brain insulin resistance. This new knowledge will facilitate the search for novel therapeutic targets for AD.

1.13 Approach (specialty areas of laboratory research employed in the thesis): Dynamic single-photon emission computed tomography/computed tomography (SPECT)/CT was employed to assess the absorption and disposition of radioiodinated (^{125}I) insulin and peptides in wild type (WT), AD transgenic (APP/PS1), and diabetic (db/db) mouse models. The pharmacokinetic parameters obtained from these studies were employed to construct physiologically-based pharmacokinetic models using SAAMII and WinNonlin software. These models were further employed to identify the molecular processes perturbed at the BBB upon Aβ exposure by employing Stella© ©. Role of Aβ peptides on insulin trafficking at the BBB was investigated in human cerebrovascular micro-endothelial cell (hCMEC/D3) monolayers in vitro. Moreover, the effect of Aβ peptides on the expression of insulin receptors (IR) on the BBB endothelial surface was imaged by spinning disc confocal microscopy. Further, fluorescence recovery after photo bleaching (FRAP) technique was

employed to investigate the impact of Aβ peptides on the lateral diffusion and exocytic recycling capacity of IR. Reverse phase protein array (RPPA) assays were employed to investigate the insulin signaling perturbations caused by Aβ peptides in hCMEC/D3 monolayers. These efforts have helped us to generate a significant body of knowledge that could be translated to studies in AD patients and age-matched normal patients aimed at investigating the role of insulin resistance during AD progression.

CHAPTER 2. INSULIN ADMINISTRATION INFLUENCES THE FLUX OF Aß40 AND Aß42 FROM THE PLASMA TO BRAIN AND VICE VERSA

2.1 Synopsis

AD progression is strongly associated with an impaired clearance of Aβ peptides across the BBB. Now, hyperinsulinemia, associated with T2DM, is known to damage the BBB and increase brain levels of Aβ peptides. However, mechanisms by which systemically administered insulin affects the fluxes of Aβ peptides remain unclear. In this chapter, the effects of peripherally administered insulin on the plasma and brain distribution of Aβ peptides were evaluated. Insulin administered via the left internal carotid artery resulted in a significant increase in plasma clearance and decrease in the Cmax and AUC of Aβ40, whereas it decreased the plasma clearance and increased the Cmax and AUC of Aβ42. The brain influx rate constant for Aβ40 was significantly increased following an insulin infusion, whereas that for Aβ42 was significantly lowered. SPECT/CT imaging assisted in constructing Patlak plots of unidirectional brain transfer of Aβ40 and Aβ42, which revealed that the trends for influx clearance were similar to that calculated following the bio-distribution study. Further, intracerebrally injected Aβ40 was cleared at a faster rate while Aβ42 was cleared at a slower rate as a result of insulin infusion. These set of studies were the first demonstration of an intricate relationship between systemic insulin and brain levels of Aβ peptides which likely affects the pathology of cerebrovascular and metabolic disorders.

2.2 Background

Newer therapies designed for AD treatment have been premised on the rationale that clearance of Aβ peptides from the brain is perturbed as the disease progresses. (Zlokovic, 1997) posited that deficits suffered by the brain in AD begin with injuries to the cerebrovasculature culminating in further insults due to impaired clearance of Aβ peptides. Several pathologies could contribute to the initial cerebrovascular insults. Type-2 diabetes (T2DM) is known to be strongly associated with cerebrovascular dysfunction.

Hyperinsulinemia is known to be a precursor for T2DM. T2DM is associated with symptoms of AD such as memory decline and neuronal degeneration. Levels of insulin are known to be dysregulated in brains of patients diagnosed with varying stages of AD. Per a concise review by (Stanley et al., 2016), hyperinsulinemia could either be considered as a cause or a consequence of AD. Longitudinal studies have reported that abnormal levels of insulin pose an increased risk for the development of AD since it could influence the deposition of Aβ peptides in the brain, as reported by (Stanley et al., 2016). Insulin is also understood to regulate the amounts of Aβ in the plasma. But, to date, there has been no trial reporting the levels of Aβ in normal patients, several years before the onset of AD. Hence there exists no confirmation of the hypothesis that resistance to insulin uptake and signaling is in fact a pre-cursor to AD progression.

Clinical trials conducted in the last decade have proved that insulin administration via the intranasal route improves the cognitive defects suffered because of AD progression. However, the caveat involved in that trial was that higher doses of

intranasal insulin did not result in a regression of clinical symptoms in AD. It suggested that causes for dysregulation of insulin within the brain in AD need to be evaluated from a mechanistic standpoint. This includes a detailed understanding the impact of insulin on reactivity of the cerebrovasculature or the blood-brain barrier (BBB) which serves as the portal for transcytosis of systemically available of insulin into the brain

Now, the BBB is the primary regulator of Aβ flux between the plasma and the brain. The distinct mechanisms by which Aβ peptides are transported from the plasma to the brain and vice versa, via the BBB, is still unknown. Therefore, it is critical to probe the kinetics of these peptides across the BBB in presence of insulin. For this thesis, my aim was to understand how systemically administered insulin affects the kinetics of Aβ peptides from the plasma to the brain and vice versa.

Results obtained from kinetic studies probing the impact of administered insulin on Aβ peptide transport into the brain will lead us to an understanding of the peptide transport perturbations involved in normal or pre-symptomatic stages of AD. This coupled with the results from the subsequent chapters investigating the impact of Aβ peptides on physiological distribution of insulin will point toward the subtle interactions occurring between insulin and Aβ peptides at the BBB in early stages of AD.

2.3 Materials and Methods: Assays were conducted in age-matched wild-type mice in which the effect of insulin administration via the internal carotid on the transport of Aβ peptides into the brain was ascertained. Protocols involving

radioactivity and non-survival animal surgeries were approved by the IACUC (Institutional Animal Care and Use Committee) at Mayo Clinic, Rochester, MN.

2.3.1 Animals: Wild-type animals (B6SJL1) at 2 months of age were procured from the Jackson laboratory and subsequently nurtured with access to food and water at the Mayo Clinic Animal Care Facility, Rochester, MN. When the animals were at 6 months of age on average, they were selected at random and distributed into the treatment groups.

2.3.2 Radiolabeled Aβ peptides: Aβ peptides were labeled with ^{125}Iodine by the Chloramine-T procedure. The steps involved in the Chloramine-T procedure are outlined as follows:

500 µg of Aβ peptides reconstituted from dried films are added to 50 µl of phosphate buffer. To this solution, 20 µl of 0.1N HCl is added. Then, the required dose of ^{125}Iodine is spiked into the solution, followed by 20 µl of Chloramine-T. The reaction mixture can stand for 5 minutes with intermittent mixing by means of a vortexer. After 5 minutes, the reaction is terminated by addition of 10 µl of sodium metabisulphite. The reaction mixture is transferred to a pre-treated and purified, 3-inch long Spectra-Por dialysis tubing (1000 MWCO) to remove unconjugated peptide. The dialysis is conducted against a 1 L PBS solution pH 7.4, overnight at 4ºC. Buffer is changed the next morning and the mixture is continued to be dialyzed for 5 more minutes. The solution is then extracted from the dialysis bag and measured for the dose of ^{125}I-Aß40 or ^{125}I-Aß42.

2.3.3 Insulin: Commercially available Humulin (Generic name: Regular insulin, human, rDNA origin: 100 U/ml) is diluted to 5U/ml in PBS and 1 U is subsequently used for injection into the animal during the study.

2.3.4 Bio-distribution studies: Randomly selected mice were anaesthetized individually and subjected to a catheter insertion via the femoral vein and the femoral artery for venal injection and arterial sampling respectively. Bolus dose of 100 µCi of ^{125}I-Aß40 or ^{125}I-Aß42 was injected into the femoral vein and 20 µl of blood was sampled arterially at 0.5, 1, ,3, 5, 10, 15 and 30 minutes. The samples were spun at 3000 rpm for 3 minutes to separate the plasma components. The plasma components were then subjected to TCA precipitation (addition of 100 µl BSA+ 200 µl trichloroacetic acid; centrifugation at 14000 rpm for 5 mins) and the TCA precipitated fraction was assessed for the accumulation of gamma counts from the injected ^{125}I-Aß40 or ^{125}I-Aß42.

For studies involving assessment of the influence of insulin on the brain uptake of ^{125}I-Aß40 or ^{125}I-Aß42, an internal carotid surgery was performed. The surgery could be summarized as a surgical incision into the neck area of a mouse, followed by a cannulation of the internal carotid with a catheter. The other end of the catheter is attached to a syringe infusion pump and the required amounts (1 U) of insulin or saline are infused at the desired flow rate (4 µl/min), whilst checking to prevent the occurrence of bubbles in the catheter space.

After blood sampling, the mouse received to a 1mm incision in the right auricle of the heart and was subjected to a slow transcardial perfusion with 10 ml of PBS.

Transcardial perfusion was conducted to wash off unbound fraction of radiolabeled peptide from tissues.

Following perfusion, the animal was euthanized. Skull was removed; brain was extracted and dissected into left and right hemispheres. Further, individual hemispheres were dissected to yield cortex, caudate putamen, hippocampus, thalamus, brain stem and cerebellum. The extent of ^{125}I-Aß40 or ^{125}I-Aß42 accumulation in brain regions was determined by gamma counting on a two-channel gamma counter (Cobra II, Amersham Biosciences Inc., Piscataway, NJ).

A sub-study involved measuring the accumulation of ^{125}I-Aß40 or ^{125}I-Aß42 in the left or right hemispheres following an infusion of a higher dose (4.2 U) of insulin via the internal carotid by the same surgical procedure summarized above).

Decline of radioactivity in plasma fit most appropriately (determined by goodness of fit and F-tests) to a bi-exponential equation on WinNonlin® (Pharsight, Mountain View, CA) as follows:

$$C = Ae^{-\alpha t} + Be^{-ßt}$$

Estimates for initial parameters (V, k_1, k_2) were specified; number of iterations (500), variance model (relative), convergence criterion (0.00001) and the minimization algorithm (Gauss-Newton) were chosen and the model was simulated to estimate the values for the intercepts A and B and the macro-constants $\boldsymbol{\alpha}$ and β. Secondary parameters such as clearance, area under the curve, distribution and elimination half-lives were also estimated from the model simulation. The model also predicted plasma values at 40 one-minute intervals.

Influx of ^{125}I-Aß40 or ^{125}I-Aß42 into the brain was calculated by normalizing the accumulation of radiolabeled peptides in individual hemispheres of the brain by the calculated AUC in the plasma. The underlying assumption was unidirectional transfer of tracer from the plasma to the brain.

$$Brain\ influx\ clearance = \frac{Radioactivity\ in\ left\ or\ right\ hemisphere\ (\mu Ci}{AUC\ in\ plasma\ (\mu Ci.\frac{min}{ml})}$$

2.3.5 Dynamic SPECT imaging: SPECT was conducted to measure the dynamic rate of uptake or clearance of ^{125}I-Aß40 or ^{125}I-Aß42 into or from the brain as a physiological response to insulin administration. Animals were prepared for injection by a procedure described in section 3.2.4. For SPECT, the dose of radiolabeled Aß peptide used was 5-fold higher than that used for bio-distribution studies, due to a limited resolution of the SPECT scanner for the small fraction of injected dose accumulating in pre-determined brain ROI. 250 µl of saline containing 1U of insulin was infused via the internal carotid at 4 µl/min. The animal then received a bolus injection of 500 µCi of ^{125}I-Aß40 or ^{125}I-Aß42 via the femoral vein. It was immediately placed in the SPECT instrument and imaged dynamically (every 1 minute) for 40 minutes. A computerized tomography (CT)image of the entire body of the imaged mouse was obtained and the SPECT data was overlaid with the CT data.

Dynamic brain uptake (µCi) was normalized with predicted plasma values (predicted at 40 one-minute intervals; normalized to the SPECT dose). Values from this normalization step were plotted against the AUC in the plasma at each time point normalized to the predicted plasma value at that time point. The

resulting plot is well known as the Patlak plot, the slope and the intercept of which signify the influx clearance and the volume of distribution in the brain compartment respectively.

$$\frac{A_b}{C_p} = K\frac{\int_0^t C_p dt}{C_p} + V$$

2.3.6 Elimination of ^{125}I-labeled Aß peptides from brain: A right hippocampal injection of radiolabeled peptide was conducted in a subsequent study to determine the transport of the peptide from the brain to plasma. The effect of insulin on the transport from brain to plasma was assessed by infusing 4.2 U of insulin via the internal carotid for 15 minutes. A hole was drilled at co-ordinates (2, 2, -2) from Bregma on the ventral side of the mouse brain with help of 0.7mm Dremel tool. The co-ordinates correspond to the right hippocampal region per the mouse brain atlas. A gas-tight Hamilton syringe was then used to inject 1 µl of solution containing 3-4 µCi of ^{125}I-Aß40 or ^{125}I-Aß42 into the drilled space. The animal was swiftly transferred to the SPECT instrument, wherein the decline of ^{125}I-Aß40 or ^{125}I-Aß42 from the brain ROI was measured every minute for 100 minutes, followed by a CT scan. The SPECT data was overlaid with the CT image to confirm the demarcated ROI and calculate the final counts. Data from the hippocampal injection was analyzed by normalizing the radioactivity to the radioactivity at the first measured time point, body weight, and administered dose. It was then plotted on a natural log scale versus time and then fitted to a one-phase decay equation on Graph Pad Prism 5. The rate constant calculated from the one-phase decay equation signifies the first-order elimination of

administered radiolabeled Aß peptides from the brain with or without a prior infusion of insulin via the internal carotid.

ENDPOINT	PEPTIDE	SPECIES	METHOD
1. Influx into brain 2. Clearance from brain 3. Biodistribution	1. ^{125}I-Aβ40 2. ^{125}I-Aβ42	WT	1. SPECT 2. PK sampling

2.4 Results

The effects of systemic insulin infusion on the plasma kinetics of Aβ40 and Aβ42 were determined by measuring their plasma concentrations at 6 time intervals after pre-infusion with 1 IU of insulin via the internal carotid artery. The pharmacokinetic data was fit to a 2-compartmental model on WinNonlin© with initial estimates for V, k_{12} and k_{21} based upon prior results published by Kandimalla et al, 2005. Plasma values until 15 minutes were predicted and overlaid with the plasma data. Figure 2.1 proves that insulin infusion significantly decreases the Cmax (mean of 26.7 µCi/mL after saline treatment reduces to 11.56 µCi/mL after insulin treatment) and AUC and significantly increases the clearance of ^{125}I-Aβ40 (mean of 1.24 mL/min after saline treatment increases to a mean of 1.85 mL/min after insulin treatment). Intriguingly, insulin infusion increases the Cmax (mean of 9.72 µCi/mL after saline treatment increases to 17.76 µCi/mL following insulin treatment) and AUC and decreases the clearance

(mean of 2.01 µCi/mL reduces to a mean of 0.975 µCi/mL following insulin treatment) from the plasma for ^{125}I-Aβ42.

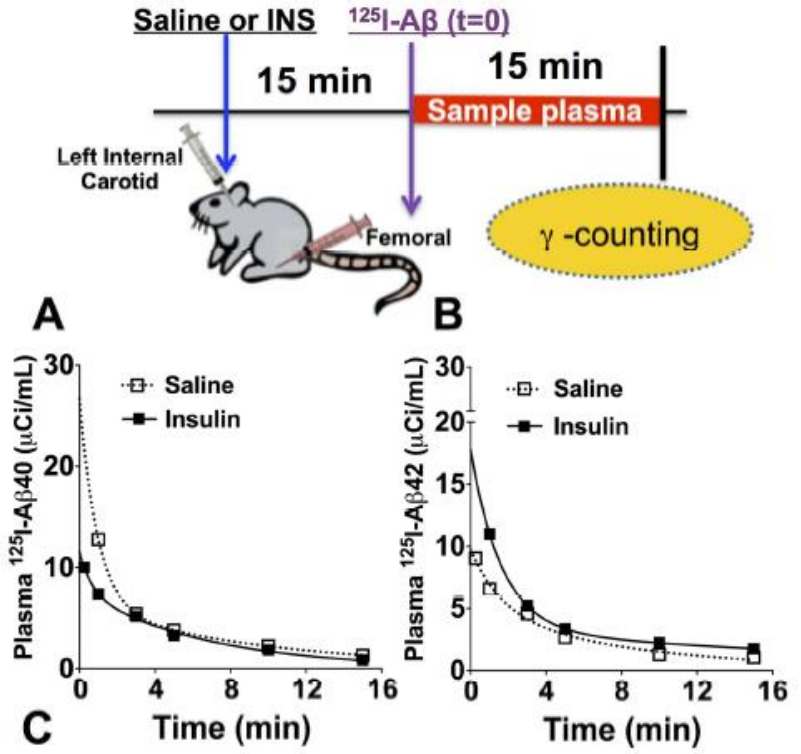

Parameters	^{125}I-Aβ40			^{125}I-Aβ42		
	Control	Insulin	*P*	Control	Insulin	*P*
Cmax, µCi/mL	26.70 ± 0.56	11.56 ± 0.92	*	9.72 ± 0.82	17.76 ± 0.17	*
CL, mL/min	1.24 ± 0.01	1.85 ± 0.14	*	2.01 ± 0.43	0.975 ± 0.04	*
AUC, min X µCi/mL	80.39 ±0.50	53.98 ± 4.12	*	49.75 ± 10.52	102.56 ± 3.85	*

Figure 2.1: Insulin administration via the internal carotid significantly modulates the plasma pharmacokinetics of ^{125}I-Aβ40 and ^{125}I-Aβ42. Figure A and figure B are plots of the observed (closed squares) vs predicted (open squares) values of plasma concentration (µCi/mL) of ^{125}I-Aβ40 against time and of ^{125}I-Aβ42 against time, respectively, when pre-injected with insulin. Figure C is a tabulated format of the plasma pharmacokinetic parameters for ^{125}I-Aβ40 and ^{125}I-Aβ42 obtained from a 2-compartmental simulation of plasma concentration profile on WinNonlin©. Data is presented as mean ± SD (n=3).

The effect of insulin infusion was measured by infusing low (1 IU) or high (4.2 IU) of insulin via the left internal carotid artery for 15 minutes, such that the left brain hemisphere received a two-fold higher exposure to insulin as compared to the right brain hemisphere (post-perfusion gamma counts of insulin in the left and

right brain hemispheres were measured and are displayed in the appendix section). As plotted in figure 2.2A, the brain radioactivity of ^{125}I-Aβ40 normalized to its plasma AUC was significantly higher when the WT mice received a pre-infusion with 1 IU of insulin.

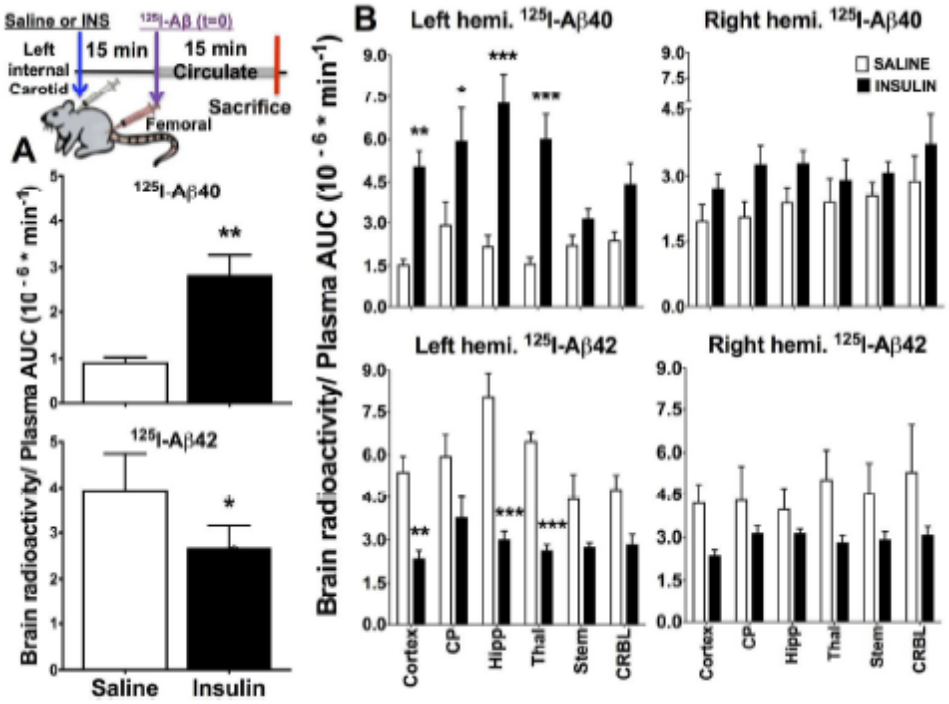

Figure 2.2. Brain radioactivity/plasma AUC of 125I-Aβ40 and 125I-Aβ42 following intravenous injection with or without a pre-infusion with 1 IU or 4.2 IU of insulin via the left internal carotid artery: Figure A depicts that brain radioactivity/plasma AUC was significantly higher for ^{125}I-Aβ40 and significantly lower for ^{125}I-Aβ42 following an administration of 1 IU of insulin. Figure B is a plot of the brain radioactivity/plasma AUC of ^{125}I-Aβ40 and ^{125}I-Aβ42 in various regions (cortex, caudate putamen, hippocampus, thalamus, brain stem and cerebellum) in the left hemisphere following administration of a higher (4.2 IU) dose of insulin. Data presented here is mean ± SD, n=3. *p<0.05.

Conversely, the brain radioactivity of ^{125}I-Aβ42 normalized to its plasma AUC was significantly lower for WT mice pre-infused with 1 IU of insulin. Figure 2.2B explains that an increased insulin dose (4.2 IU) significantly increased the brain radioactivity of ^{125}I-Aβ40 in the cortex, caudate putamen, hippocampus and

thalamus of the left hemisphere of WT mice. Whereas, the brain radioactivity of ^{125}I-Aβ42 in the cortex, hippocampus and thalamus of the left hemisphere of WT mice was significantly decreased following a pre-infusion with a higher (4.2 IU) dose of insulin.

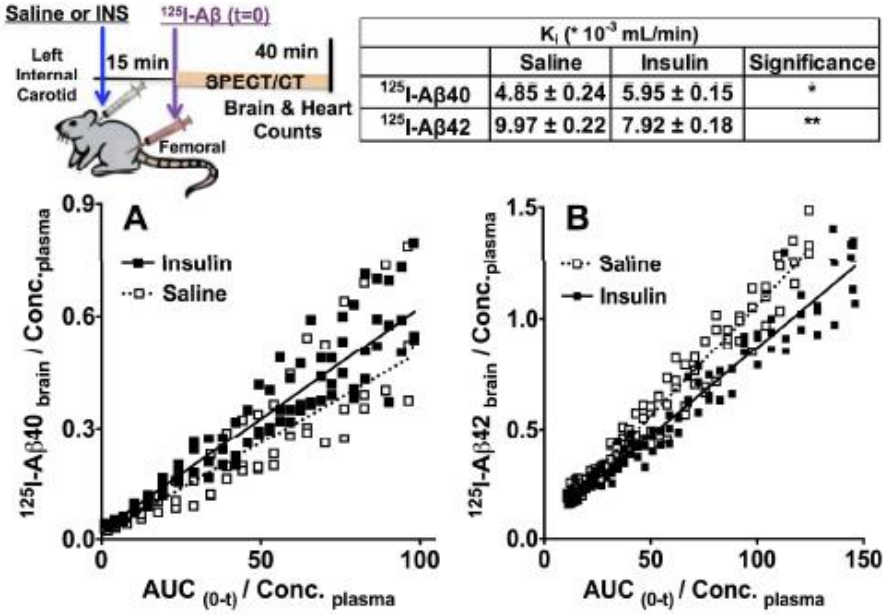

K_i (* 10^{-3} mL/min)			
	Saline	Insulin	Significance
^{125}I-Aβ40	4.85 ± 0.24	5.95 ± 0.15	*
^{125}I-Aβ42	9.97 ± 0.22	7.92 ± 0.18	**

Figure 2.3: Brain influx clearance obtained from Patlak analysis of brain uptake of ^{125}I-Aβ40 and ^{125}I-Aβ42 in WT mice following an insulin injection via the internal carotid artery. Figure A is a regression analysis (Patlak plot) of brain amounts of ^{125}I-Aβ40 normalized to its concentration in the plasma, versus the AUC of ^{125}I-Aβ40 in the plasma from 0 to t normalized to its concentration in the plasma. Figure B is a Patlak analysis of ^{125}I-Aβ42 amounts in the brain. The table printed on the top right of the figure represents values for brain influx clearance (as obtained from slopes of linear regression of figures A and B) for ^{125}I-Aβ40 and ^{125}I-Aβ42, following an insulin injection via the internal carotid artery.

Next, dynamic SPECT/CT imaging was employed to measure the brain uptake of intravenously administered ^{125}I-Aβ40 or ^{125}I-Aβ42 following an insulin infusion as in Figures 2.1 and 2.2. Amounts of ^{125}I-Aβ40 and ^{125}I-Aβ42 (μCi) in the brain at every minute until 40 minutes were normalized to predicted values (adjusted for dose) corresponding to the plasma concentrations of the tracer (from plots in

figure 2.1). They were plotted against the plasma AUC(0 to t) of the tracers normalized by the plasma concentrations of the given tracer. In other words, Patlak regression analysis of the unidirectional transfer of ^{125}I-Aβ40 and ^{125}I-Aβ42 into the brain tissue was conducted (figures 2.3A and B) Slopes of the regression lines in figures 2.3A and B represent the brain influx clearance for ^{125}I-Aβ40 or ^{125}I-Aβ42. They are tabulated in the inset of figure 2.3. A comparison of the brain influx clearance for ^{125}I-Aβ40 after an infusion with saline or insulin reveals that insulin significantly increased the influx clearance from a mean of 4.85 X 10^{-3} mL/min to 5.95 X 10^{-3} mL/min. Conversely for ^{125}I-Aβ42, brain influx clearance decreased following insulin infusion (reduced from a mean of 9.97 X 10-3 mL/min after saline treatment to 7.9 X 10^{-3} mL/min after insulin treatment).

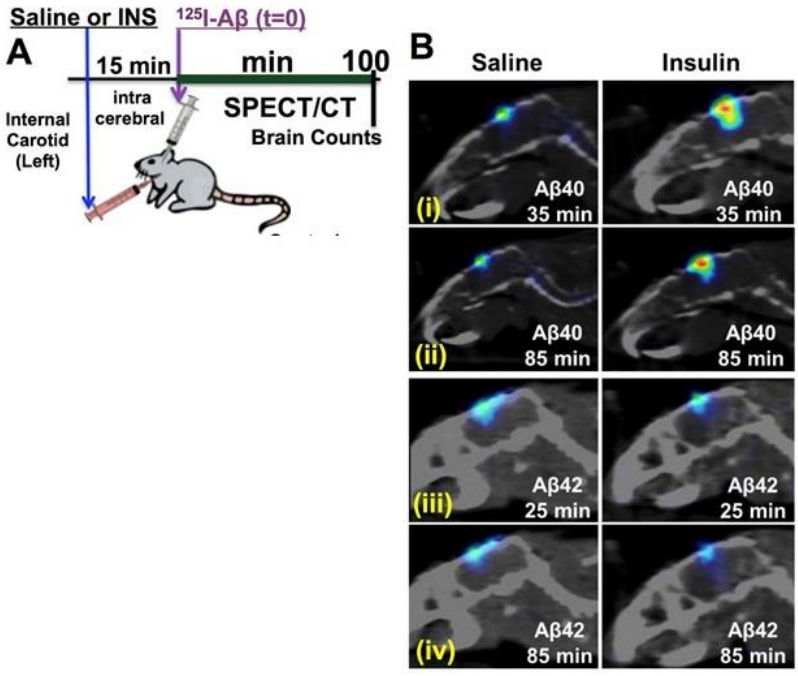

Figure 2.4. SPECT/CT scan of brain ROI in WT mice following an hippocampal injection with ^{125}I-Aß40 or ^{125}I-Aß42 with or without a pre-injection with 1 IU of Humulin via the internal carotid artery. Schematic 2.1 A displays the timeline of the SPECT/CT imaging assay wherein saline or insulin is administered via the

left internal carotid artery followed by an intra-cerebral ^{125}I-Aß injection and imaging for 100 minutes. On the right-hand side, SPECT/CT scans of brain ROI after saline or insulin infusion for Aβ40 after 35 minutes and 85 minutes in (i) and (ii) respectively.

Having noted a significant influence of insulin adminstration on plasma distribution and brain uptake kinetics of Aβ40 and Aβ42, subsequent SPECT/CT imaging was conducted to observe the effects of insulin infusion on kinetics of elimination of Aβ peptides from the brain. To capture elimination from the brain, ^{125}Iodine-labeled Aβ40 and Aβ42 (3-4 μCi) were injected into the right hippocampus and SPECT/CT imaging was conducted at each minute for 100 minutes. The effects of insulin infusion were observed by infusing the animal with 1 IU of insulin for 15 minutes into the internal carotid artery prior to the hippocampal injection of labeled Aβ peptides. Significant differences in brain elimination of ^{125}I-Aβ40 or ^{125}I-Aβ42 following saline or insulin pre-infusion are depicted through CT scans of brain ROI (figure 2.4).

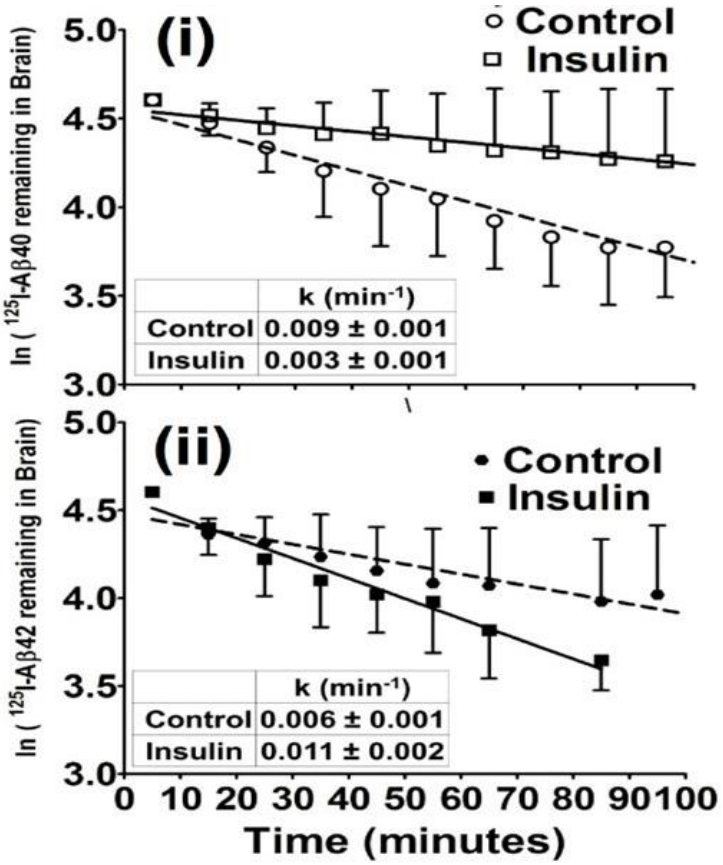

Figure 2.5. Semi-log plot of 125I-Aβ40 and 125I-Aβ42 remaining in the brain after injection with 1 IU of insulin via the internal carotid artery. Figure i) is a semi-logarithmic plot of SPECT/CT data concerning ^{125}I-Aß40 remaining in brain following a pre-infusion with saline or insulin. Figure ii) is a semi-logarithmic plot of SPECT/CT data concerning ^{125}I-Aß42 remaining in the brain following a pre-infusion with saline or insulin. The slopes of the logarithmic decline represent the

Elimination data for time points until 100 minutes was normalized to the elimination at the 1st minute. Resulting values were log transformed and fit to a one-phase decay equation. The elimination rate constants are presented in figure 2.5. Insulin infusion significantly decreases the brain elimination rate constant of ^{125}I-Aβ40 (0.003 min^{-1}) while it significantly increases the elimination rate constant of ^{125}I-Aβ42 (0.011 min^{-1}) as compared to saline infusion.

2.5 Discussion

(Stanley et al., 2016) found that peripherally administered insulin could modulate the plasma clearance of Aβ and increase its interstitial fluid levels. It also showed that intracerebrally administered insulin did not affect Aβ levels in the brain. Studies explained in this chapter attempted to resolve findings of earlier publications by examining the effect of systemically administered insulin on kinetics of brain uptake and elimination of Aβ40 and Aβ42.

Infusion of 1 IU of insulin through the left internal carotid artery resulted in a significant decrease in the plasma availability of Aβ40 i.e. it decreased the mean Cmax levels and increased the mean clearance of Aβ40. This finding corroborates the results from (Tamaki, Ohtsuki, & Terasaki, 2007) that insulin facilitates the hepatic clearance of Aβ40. The observation that Aβ42 clearance is decreased because of prior systemic exposure to insulin agrees with the finding that Aβ42 is disposed to cause hepatic insulin resistance which in turn, reduces the elimination of Aβ42 from plasma (Zhang et al., 2013).

Uptake rates of Aβ40 and Aβ42 into brains of WT mice were measured by two independent methods: a) by normalizing brain uptake after intravenous administration of the radiolabeled tracer to its AUC in the plasma and b) by Patlak regression analysis of amounts of radiolabeled tracer in the brain following SPECT/CT imaging. Through both methods, it was found that 1 IU of insulin significantly increased the rate of uptake for Aβ40 while it decreased the rate of uptake for Aβ42 into the brain. Higher levels of insulin in plasma enabled a better resolution of Aβ40 and Aβ42 amounts in various regions of the left and right

hemisphere. A comparison of the basal clearance of Aß40 and Aß42 shows that Aß40 has a significantly higher plasma AUC than that for Aß42. This could be due to a differential mechanism of LRP-1 mediated clearance from the peripheral circulation (Tamaki et al., 2007).

Per our estimates, infusion of insulin via the left internal carotid artery leads to a two-fold higher accumulation of insulin in the left hemisphere as compared to the right hemisphere (Figure A1; appendix) within the experimental time frame (30 mins). We found that an infusion of a high dose (4.2 IU) of insulin via the left internal carotid artery increased the accumulation of Aβ40 in the cortex, caudate putamen, hippocampus and thalamus of the left hemisphere. It did not significantly affect the accumulation of Aβ40 in various regions of the right brain hemisphere. This difference in Aβ40 accumulation in the left and right brain hemispheres aligns with our finding that insulin differentially accumulates in the left-brain hemisphere versus the right hemisphere following an infusion via the left internal carotid artery. It negates the possibility that the insulin-induced differential Aβ40 accumulation is a systemic pharmacological effect as opposed to a localized exposure effect. If it were a systemic pharmacological effect, accumulation of Aβ40 in both hemispheres would be less distinguishable.

Intracerebral injection resulted in a decreased rate constant of Aβ40 elimination in mice pre-treated with insulin, whereas the rate constant was significantly increased for Aβ42 elimination due pre-treatment with insulin. This observation provided additional support to the inference that Aβ40 is more disposed to be retained in the brain when WT mouse brains receive insulin while the opposite is

true in the case of Aβ42. In saline-treated controls, Aß40 has a lower propensity for brain retention as compared to Aß42, possibly due to enhanced LRP-1 mediated clearance from the vascular endothelium and brain parenchyma. Aß42 exhibits a higher basal retention in the brain, possibly due to formation of beta-sheet structure over extended time periods, thereby precluding its LRP-1 mediated clearance from the brain (Deane et al., 2004).

Findings from this chapter suggest that brain response to insulin is crucial to the regulation of Aβ40 and Aβ42 trafficking and maintenance of a therapeutic ratio of Aβ40: Aβ42 in the brain. Validation of the experimental data from this chapter regarding the role of insulin in Aβ trafficking will be done through the application of multi-compartmental pharmacokinetic simulations in chapter 4.

CHAPTER 3. INSULIN BIODISTRIBUTION AND BRAIN ACCUMULATION IS IMPAIRED BY THE PRESENCE OF Aβ40 AND Aβ42

3.1 Synopsis

Peripherally administered insulin dose-dependently modulates the peripheral and cerebral kinetics of Aβ40 and Aβ42, as demonstrated by findings in the previous chapter. Physiological levels of insulin are therefore implicated in maintaining therapeutic ratios of Aβ40: Aβ42 in the body. AD pathology, however, is known to be associated with peripheral insulin resistance and insulin levels have been found to be lowered in post-mortem AD brains. The relation between peripheral insulin resistance and its availability in the brain in an AD phenotype has heretofore not been investigated. This chapter examines the propensity of an early-stage AD, ageing or insulin-resistant phenotype to affect the biodistribution of insulin and its availability in the brain. Biodistribution studies revealed that insulin plasma kinetics were significantly modulated in APP/PS1 transgenic mice or mice systemically pre-infused with pathological doses of Aβ40 and Aβ42. Moreover, brain influx clearances for insulin in APP/PS1 mice or mice injected with Aβ40 and Aβ42 were significantly lowered as compared to control WT mice. Intracerebrally injected insulin was eliminated at a significantly faster rate from APP/PS1 brains as compared to WT brains. Further, the systemic administration of competing amounts of unlabeled insulin resulted in a steeper decrease in the influx clearance of ^{125}I-insulin into APP/PS1 brains as compared to WT brains. Similar modulation of insulin biodistribution and brain accumulation were observed in aged WT mice or insulin-resistant (db/db) mice. Moreover, peripheral kinetics and brain distribution of insulin is studied in diabetic model mice and

aged mice, which are understood to be resistant to insulin action. Results from these were compared with the findings regarding the effects of Aβ peptides on insulin distribution in WT mice in the context of peripheral insulin resistance and decreased brain uptake. In all, the findings from this chapter provide crucial in-vivo evidence for the inhibitory effects of Aβ peptides on insulin biodistribution and brain uptake.

3.2 Background: Approximately thirty publications, beginning in the 1950s, were based on an investigation of kinetics of insulin in the plasma following administration of the hormone via the peripheral circulation. The peripheral circulation data was embedded into compartmental models constructed to simulate the removal of insulin from the blood in normal and T2DM patients. Among the predicted parameters, a clinically relevant one was the half-life of insulin which was reported to occur in a time range between 15-35 minutes in a healthy adult human.

An investigation of insulin and glucose levels in the blood in AD patients, however, has only been conducted four to five times since the turn of the millennium, ever since the clinical association between AD and T2DM began to materialize. These studies have focused on measuring and reporting differences in plasma levels of glucose and insulin signaling markers in post-mortem brains between the two groups of patients. There is only one study, however, measuring the concentrations of insulin in the blood of an AD phenotype (Stanley et al., 2016). In this aforementioned study, the flux of the peripherally administered insulin into phenotypic AD brains was not examined. As explained in the

introduction to this thesis, systemic distribution of insulin in an AD phenotype and dynamics of its transport between organs, specifically from the periphery into the brain across the BBB is a critical parameter which requires a clinical investigation. This is due to the fact that it is likely associated with the kinetics of Aß peptides across the BBB from the brain to plasma and vice versa, as explained in chapter 1. Hence, mechanistic aspects of its distribution and anomalies thereof, in an AD phenotype, require to be investigated to ascertain the intricate interplay between insulin transport, signaling and Aß clearance in AD brains.

Distribution of insulin and insulin-like growth factor into brains has been documented in a few publications (Q. Wang & Lu, 1994), (Werther et al., 1989), (Hasselbacher et al, 1985). (Kamei et al., 2016) visualized and quantitatively assessed the distribution of radiolabeled insulin in the brain. Insulin was conjugated with a cell-penetrating peptide to improve its delivery across the nasal epithelium upon nasal administration. The administered insulin mainly accumulated in the olfactory bulb and hypothalamus. They also showed that the accumulation of insulin in the above brain regions after 15 minutes of intranasal administration was significantly more than that observed during blood-to-brain transport. This underscores the fact that the blood-to-brain transport is a transport mechanism fraught with systemic barriers. However, no study has extensively mapped the distribution of insulin in the brain following systemic exposure in AD.

In this chapter, the impact of Aß peptides on the kinetics of transport of administered insulin in AD transgenic (APP/PS1) mice will be reported and discussed. Kinetic measurements in APP/PS1 mice will be evaluated alongside results from control studies conducted in mice models expressing extreme insulin resistance (db/db) and aged wild-type mice. Insulin is postulate to be transported by a receptor-mediated blood-brain barrier process into db/db mice as in AD mice As an additional control, the effects of Aβ peptide infusion into the systemic circulation of WT mice on the kinetics of administered insulin will also be examined and discussed. The hypothesis is that Aß peptides decrease insulin transport into the brain parenchyma and perturb its kinetics in the plasma.

3.3 General Methods: The focus of my study was therefore to devise a method to measure the transport of insulin from its site of administration in the periphery, to tissues in various brain regions, wherein the insulin accumulates. To non-invasively track the influx of insulin into the brain and the heart, following its injection in the peripheral vein, we employed an imaging technology known as Single Photon Emission Computed Tomography (SPECT).

3.3.1 Generalities of SPECT: SPECT is a quantitative imaging modality which utilizes a radiotracer to dynamically track the biodistribution of labeled moieties within the body. The chief advantages of the SPECT modality are high resolution (picomolar limit), non-invasiveness and absence of a limit to the extent of tissue penetration (Suzuki et al., 2015). SPECT is often employed in combination with Computed Tomography (CT) as it helps generate an anatomical map of the region of interest. This enables an observation of functional abnormalities in a 3D

spectrum at greater resolution, an aspect which is not afforded through SPECT alone.

The first instance of the utilization of SPECT to study brain distribution was when (Kosuda et al., 1993) reported that SPECT assisted in non-invasively observing the efficacy of chemotherapy in patients. Post-operative patients were intra-arterially infused with 99mTc-HMPAO and SPECT measured the cerebral distribution. The results were shown to be significantly different from those obtained by performing angiography. It also showed variations in cerebral distribution, depending upon the nature of injection. (Declercq, Vandenberghe, Van Laere, Verbruggen, & Bormans, 2016) explained the significance of SPECT in visualizing molecular abnormalities in pathologies such as AD wherein the escalation of pathological Aβ plaques in the brain begins prior to the appearance of clinical symptoms. He emphasizes that SPECT procedures help highlight the visualization of dose-dependent target occupancy, thereby assisting in simplification of problems with dose optimization during clinical trials. Research is also being conducted to determine the effectiveness of SPECT in generating data with respect to cerebral perfusion. SPECT is therefore being considered as a functional imaging test as part of a routine examination for AD.

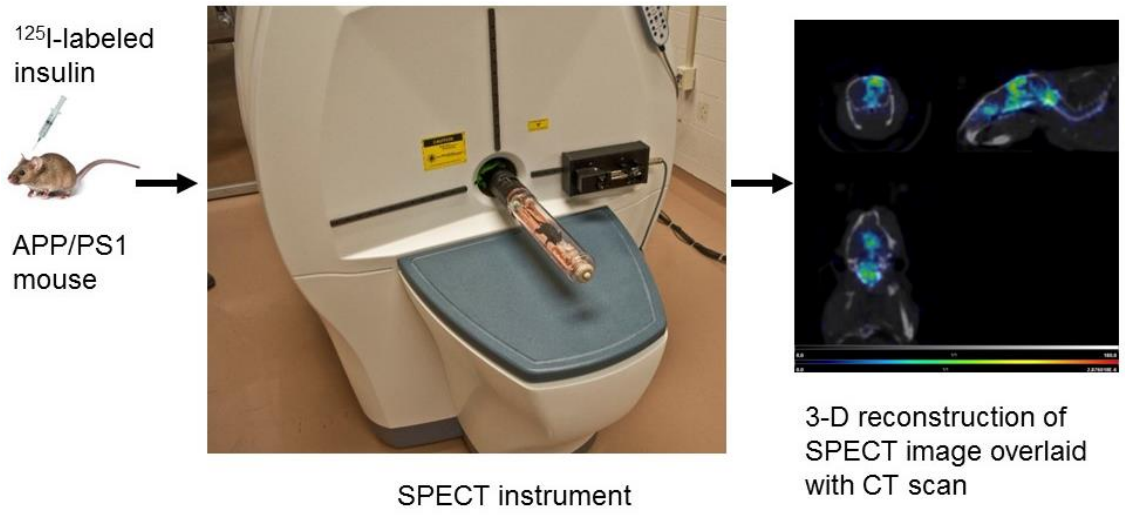

Figure 3.1. Pictorial representation of an in-vivo experiment involving SPECT/CT imaging.

3.3.2 Working of SPECT: A SPECT instrument captures spontaneous emission of gamma rays from a radiolabeled moiety with help of a stationed gamma camera. The emitted rays undergo attenuation in the tissue by a process known as Compton Scattering. Attenuated photons are predisposed to scatter thereby tracing a path separate from those which enter the collimator. This results in an increase in background signal. A well understood technique applied to correct for attenuation is Computerized tomography. It allows for a high resolution based reconstruction of cross-sectional anatomical features of the subject under the scanner. CT is often applied to ascertain the effectiveness of surgery or to devise strategies for radiation therapy. CT images are combined along with SPECT images with the inclusion of a correction factor to account for the resolution of CT images versus those acquired through SPECT. Data is generated from planar images obtained from the source by cameras situated at multiple angles are reconstructed in the 3-D format (Gamma Medica Ideas Pre-Clinical Imaging, Northridge, CA). For instance, 360º SPECT involves capture of 120 images every

3º. Acquisition time in SPECT depends upon the type of collimators used, density of the region being penetrated, and nature of the detector. For our studies, we utilized a low energy high-resolution parallel-hole collimator with 12.5 cm FOV. min acquisition time was 13.36 min; 64 projections (10 sec per projection); and reported resolution of 1 to 2 μm. The CT acquisition was a continuous circular orbit with a 50 μm slice thickness; 256 images at 80 kVp with a 0.28 mA current; and a reported resolution of 43 μm. SPECT-CT image processing was conducted using Biomedical Image Quantification and Kinetic Modeling Software version 2.85 (PMOD Technologies, Switzerland). The older SPECT instrument at Mayo Clinic (operated until 2013) generated one image every 15 seconds whereas the newer instrument (operated after 2014) procedure generated one 3-D image every 60 seconds. The entire duration of imaging was 40 minutes during which the uptake, distribution and elimination of insulin was captured.

SPECT differs from Positron Emission Tomography in that PET operates on a principle of measuring interactions between positrons and electrons, whereas SPECT is based on the sole measurement of gamma decay. SPECT cameras are also relatively cheaper and more available as compared to PET. SPECT typically does not allow for the heart to be a surrogate measure of the blood flow as opposed to PET. However, a novel prototype of SPECT/CT at the Mayo Clinic generates images following cardiac perfusion. These images are combined along 3-D images reconstructed from SPECT/CT to provide data regarding the post-perfusion uptake of tracer in the specified organs.

A parallel method adopted to study distribution of insulin was to measure the radioactivity of injected compound in the tissues by invasive sampling and tissue collection at the end of the experiment.

3.3.3 Radiolabeling the insulin: Insulin is radiolabeled by a Chloramine-T reaction procedure. Humulin is reacted with 100mM phosphate buffer, 0.1 N HCL and chloramine-T solution. ^{125}Iodine is then added to the reaction mixture based on the required amount of radioactivity. The reaction can progress for 5 minutes, following which, 10 µl of sodium meta-bisulphite is added to the reaction mixture to stop the reaction. The reaction mixture is dialyzed overnight, against PBS in a Spectra Por Molecular WT 1000 dialysis membrane.

Blood sampling- Blood sampling is done through the femoral vein through the insertion of a catheter. 20 µl of blood is withdrawn and plasma is separated by centrifugation at 3000 rpm for 3 minutes. Blood samples are withdrawn at 0.5, 1, 3, 5, 10, 15 and 30-minute time points. Radioactivity in the organs are determined by euthanizing the mouse and dissecting individual organs. Radioactivity is measured in a gamma counter in the ^{125}Iodine channel.

3.3.4 Plasma pharmacokinetics: Plasma kinetics are calculated by fitting the decline in ^{125}I-insulin radioactivity in the plasma versus time to a two-compartmental pharmacokinetic model. The primary and secondary parameters are obtained from simulating the model by adjusting a range of initial values for parameter and the minimization criteria.

Insulin uptake into the brain: The molecular weight of insulin is greater than 4000 dalton, an empirically determined limit below which exist molecules capable of crossing the blood-brain barrier. Pardridge et al proved that uptake of insulin into the brain is receptor-mediated by conducting transcytosis studies in microvessels isolated from the brain. Further, to avoid a confounding factor in form of the metabolism of insulin, they infused ^{125}I-insulin via the carotid artery of developing rabbits. Through a series of autoradiography, transport and degradation studies, they again proved, through the observation of saturation in uptake, that blood-to-brain transport of insulin required the presence of receptors at the blood-brain barrier.

With respect to this thesis, the objective was to measure the uptake of insulin in APP/PS1 mouse models after administration via the femoral vein. Insulin is understood to be metabolized mostly in the liver and the kidneys. It distributes extensively in muscles and adipose tissue. Therefore, only a miniscule fraction of the intravenously injected amount was expected to enter the brain parenchyma. The animals were injected intravenously with 500µCi of ^{125}I-labeled insulin. They were immediately placed in the SPECT instrument, which was calibrated to account for the measurement of signal in the brain. SPECT cameras capture the decay every minute for 40 minutes. The data is then superimposed with the CT scans to generate 3D-anatomical scans of the ROI. The experimental design was as follows and the results will be described in the same order:

ENDPOINT	PEPTIDE	SPECIES	ASSAY

1. Influx into brain 2. Clearance from brain 3. Biodistribution	^{125}I-insulin	APP/PS1	4. SPECT 5. PK sampling
1. Influx into brain 2. Biodistribution	^{125}I-insulin	db/db	1. SPECT 2. PK sampling
1. Influx into brain 2. Biodistribution	^{125}I-insulin; ^{125}I-insulin+ Aβ40/Aβ42	WT	1. SPECT 2. PK sampling
1. Influx into brain 2. Biodistribution	^{125}I-insulin	Aged WT	1. SPECT 2. PK sampling

Table 3.1: Scheme for experimental assays based upon the nature of endpoints, peptides or species of mice

Influx rate of insulin into the brains of mice was calculated both by graphical (non-compartmental) analysis and compartmental model analysis and simulation. Graphical plots were constructed using canonical Patlak and Logan equations and their relative accuracy in mimicking the physiological kinetics were assessed. SAAM2 (Simulation analysis and modeling) software was employed to construct a three-compartmental model of insulin distribution and goodness-of-fit of simulated parameters was assessed.

3.3.5 Patlak plots: Patlak plot represents a graphical method to determine the transfer of a radiotracer from the site of administration to the tissue of interest. The inherent assumption of Patlak equation is that the tracer transfer from the site of administration to the tissue region is irreversible. The final equation to be graphically plotted is obtained by normalizing by the concentration in the plasma.

$$\frac{A_{Tissue}(t)}{C_p(t)} = K\frac{\int_0^t C_p(\tau)d\tau}{C_p(t)} + V$$

The slope K represents the influx rate constant while the intercept V represents the volume of distribution in the tissue of interest. The term on the left-hand side represents the volume of distribution in the brain and the surrounding vasculature. The trend of the graphical plot will resolve to a linear phase following the initial time required for equilibration of the irreversible transfer from one compartment to the other. With respect to insulin distribution into the brain following injection through the femoral vein, it is assumed that plasma is the first compartment or the compartment of tracer administration. Since the whole brain will be the selected ROI for SPECT, it will represent the corresponding tissue region. The compartmental model ensures that the tracer's kinetics are irreversible after the initial period of equilibration.

3.4 Materials and methods:

3.4.1 Animals: APP/PS1(Swedish mutation) and WT mice were procured at the age of 2 months from Jackson Laboratory, Gainesville, FL. Diabetic db/db (leptin receptor deficient) and corresponding non-homozygous littermates were offered

generously by Dr. James Kirkland's laboratory at the Ageing Center, Mayo Clinic. Rochester.

SPECT/CT: Dynamic SPECT/CT (Gamma medica, Northridge, CA) was employed to measure the uptake of the radiotracer into the region of interest.

3.4.2 Insulin tolerance test (ITT): Sensitivity of Humulin (Eli Lilly) was assessed in mice before conducting studies described in this chapter. Mice were fasted for 4 hours prior to ITT. 0.6 IU/g of Humulin was injected intraperitoneally and glucose levels were monitored at time intervals until 120 minutes with help of glucose test strips. db/db mice were used as a control for insulin tolerance.

3.5 Results:

Tolerance of transgenic AD mice to insulin was measured in APP/PS1de9 mice. ITT test revealed that APP/PS1de9 mouse were more tolerant to the administration of 0.6mU/g of Humulin© (100mU/mL). The blood glucose levels in APP/PS1de9 mouse at the 15^{th} and 30^{th} minute time points (Figure 3.1) were significantly greater than those in WT mice (one-tailed t-test). ITT was a confirmation of the biological activity of the administered Humulin©. The relative insensitivity of insulin in transgenic AD mice was the first indication of a peripheral resistance to insulin in these mice.

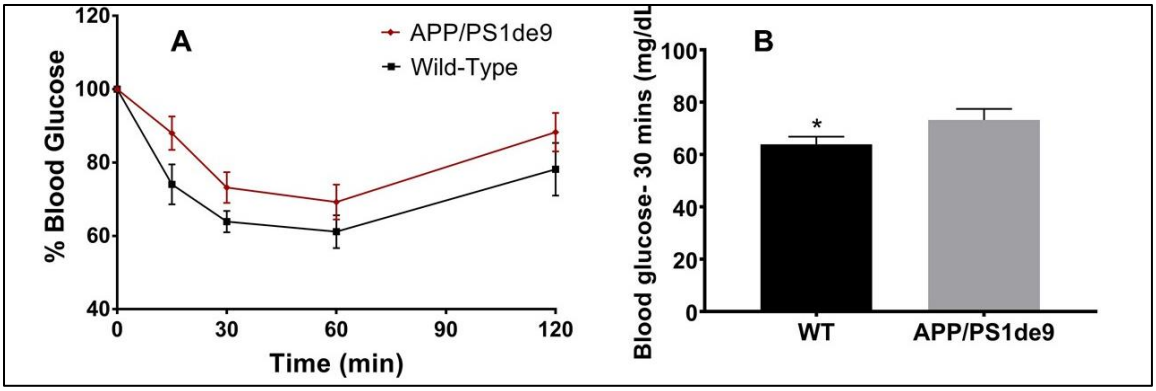

Figure 3.2. ITT of 8-month old WT mice and APP/PS1de9 mice: WT (n=19) and APP/PS1de9 (n=20) were fasted for 4 hours prior to ITT. Fig 3.1A) Both groups of mice were intraperitoneally administered with 0.6 mU/g of Humulin© (100U/mL), and blood was drawn from through tail bleeds at 15, 30, 60 and 120-minute time intervals. Blood glucose was measured with Precision Xtra© glucose test strips and normalized to the fasting blood glucose level at time 0. Fig 3.1B) Blood glucose levels at the 30th minute time point for WT is significantly lower than APP/PS1de9 mice. A one-tailed t-test was performed on Graph Pad 7©; *one-tailed p-value=0.037.

The clearance and AUC of ^{125}I-insulin in APP/PS1 mice was significantly increased and decreased respectively, as compared to WT mice. when the data from the plasma concentration profiles were input into a two-compartmental model on SAAM II© and analyzed with initial estimates for V, k12 and k21 (two-compartmental distribution rate constants) (Table 3.1)

	WT	APP/PS1	Statistics
CL (Mean ± SD) (ml/min)	0.30 ± 0.05	0.74 ± 0.35	**P < 0.01
AUC (Mean ± SD)(µCi.min/ml)	332.9 ± 59.1	136.03 ± 64.26	*P < 0.05

Table 3.1 Clearance and AUC of intravenously injected ^{125}I-insulin in APP/PS1 and WT mice. Parameter estimates for clearance and AUC were obtained from two-compartmental analyses of data averaged from the plasma concentration profile of 6-month old WT (n=6) and APP/PS1 (n=6).

Following the observations of lowered peripheral insulin levels (increased clearance) in APP/PS1 mice , brain uptake of 500 µCi of intravenously administered ^{125}I-insulin in APP/PS1 mice was measured by the SPECT/CT imaging protocol. Within the first three minutes after administration of ^{125}I-insulin, it is assumed the radioactivity in the brain parenchyma is insignificant. The brain radioactivity can thus be attributed to ^{125}I-insulin binding to its receptor at the cerebrovascular endothelium. The kinetic curves presented in Fig. 3.3 have clearly demonstrated that ^{125}I-insulin binding in WT mice was significantly higher than that observed in APP/PS1 mice. Except the earliest data point, the ^{125}I-insulin radioactivity was substantially greater in WT mice (n=5) than in APP/PS1 (n=4) mice (*p<0.05, two-tailed t-test).

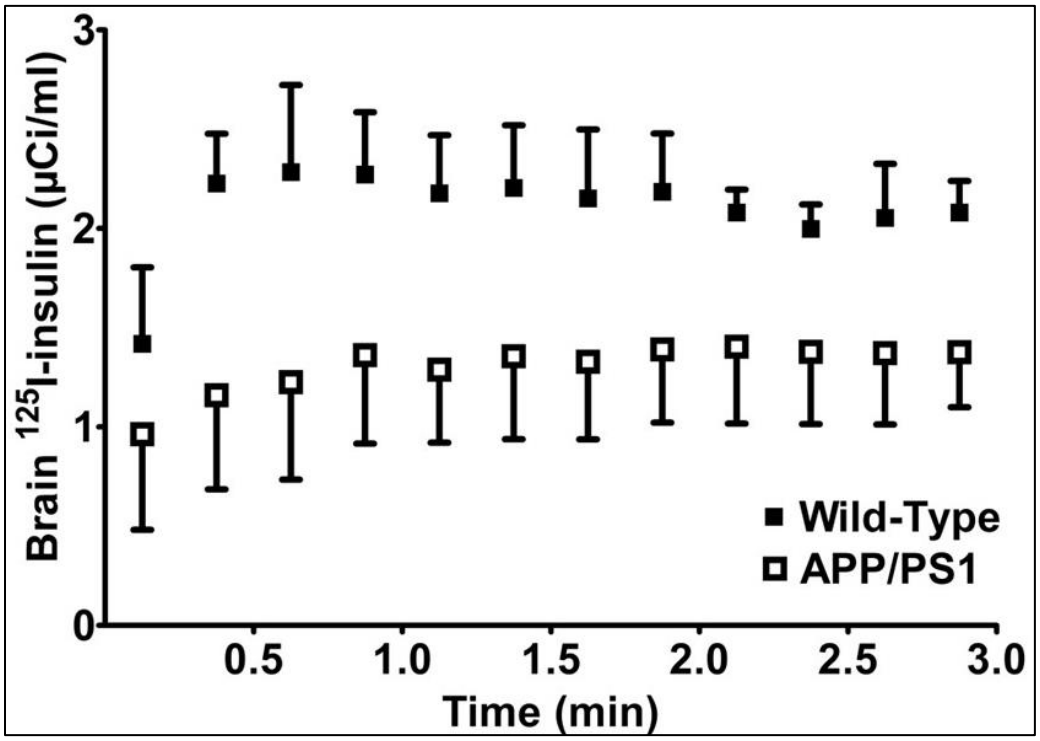

Figure 3.3: Brain uptake of ^{125}I-insulin (µCi/ml) is plotted against time for Wild-Type and APP/PS1 mice. 500 µCi of ^{125}I-insulin was injected via the femoral vein

into and the brain uptake was measured every 12 seconds by SPECT. The brain concentrations of ^{125}I-insulin were corrected for the vascular component by subtracting the brain concentrations by the vascular concentrations (obtained by multiplying the plasma concentration at each time point by the vascular volume. The vascular volume was calculated by normalizing the amount of ^{125}I-insulin in the vasculature by the plasma concentration at the last measured time point. The vascular amount was obtained by subtracting the perfused brain amount from the brain amount at the last measured time point)

Next, we wanted to quantitate the influx clearance into the brain based on the uptake data for 3 minutes. To do so, we normalized the brain uptake in µCi to the plasma concentration (predicted from plasma pharmacokinetic studies conducted in WT and APP/PS1 mice). This was then plotted against a ratio of area under the curve of ^{125}I-insulin from 0 to t to the concentrations of ^{125}I-insulin in the plasma. The slope generated from this plot would represent the influx rate constant of ^{125}I-insulin into the brain. The intercept would represent the volume of distribution of ^{125}I-insulin in the plasma. We observed that the influx rate constant of ^{125}I-insulin into APP/PS1 brains was significantly reduced as compared to WT mice.

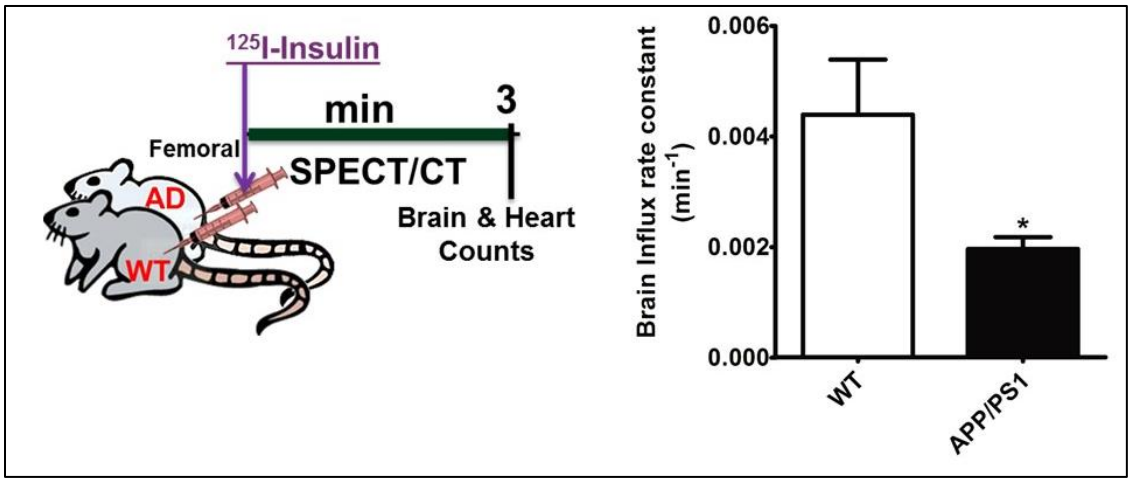

Figure 3.4: Brain influx clearance (ml/min) of ^{125}I-insulin were plotted for WT (n=4) and APP/PS1 mice (n=4). Brain influx clearances are the slopes of multiple regression (Patlak) plots of SPECT data from figure 3.4. Patlak analysis is

conducted by plotting the amount of ^{125}I-insulin (µCi) in the brain normalized by concentration of ^{125}I-insulin (µCi/ml) in the plasma on the x axis, and the AUC (from 0 to t) normalized by the concentration of ^{125}I-insulin in the plasma on the y-axis. Plasma concentrations of ^{125}I-insulin were obtained by simulating the sampled plasma concentrations from mice intravenously injected with 100 µCi of ^{125}I-insulin.

To quantitate rate of insulin clearance from an APP/PS1 brain, WT and APP/PS1 mice were subjected to intracerebral infusion of ^{125}I-insulin into the right hemisphere of the brain for 1 minute. Following that, brains of the animals were perfused and imaged by SPECT at 5-minute time intervals for 2 hours. At the end of the imaging period, animals were sacrificed; and brain regions and peripheral organs were extracted and analyzed for accumulation of ^{125}I-insulin radioactivity. The first order rate constant for insulin elimination from the brain, as calculated from linear regression slopes of data in Fig 3.6, was three-fold higher in APP/PS1 mice as compared to WT mice. Further, the fraction of insulin transported from the left hemisphere to the right hemisphere was significantly higher in APP/PS1 mice than in WT mice (data not shown).

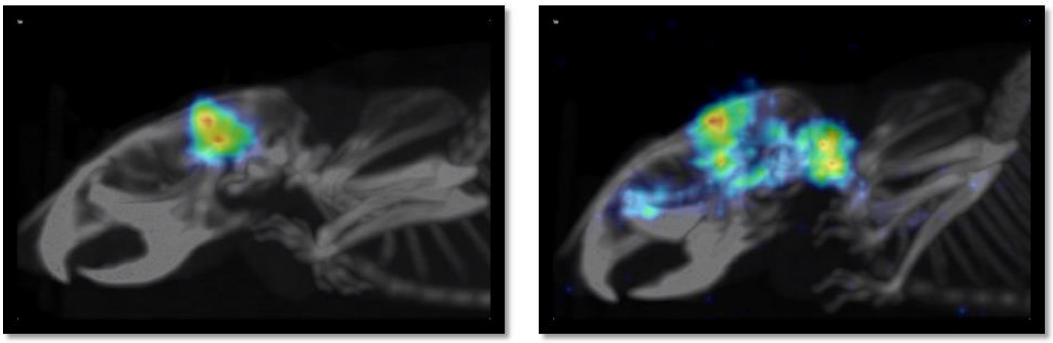

Figure 3.5. CT image of brain levels of ^{125}I-insulin 60 minutes following intracerebral injection of ^{125}I-insulin in APP/PS1 or WT mice

If clearance processes of insulin within the tissues are the same, it can be deduced that the volume of distribution in the brain was significantly lower for

APP/PS1 mice as compared to WT mice. This, in turn, suggests that the intracellular uptake of insulin in the brain is lowered in APP/PS1 mice.

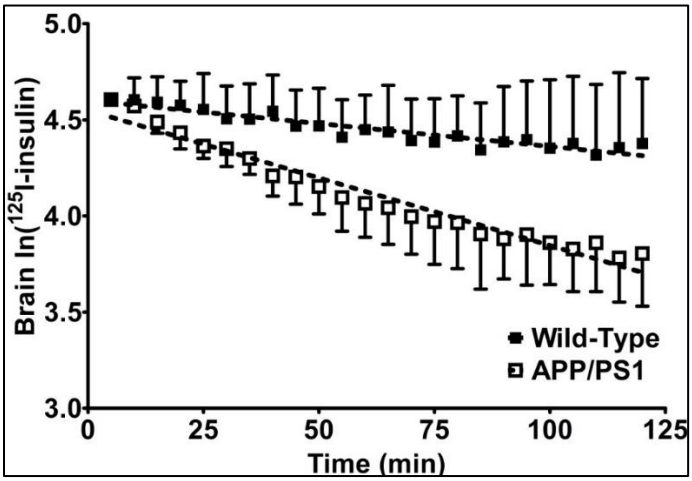

Figure 3.6. Semi-log plot of brain levels ^{125}I-insulin as measured by SPECT imaging following intracerebral injection in WT or APP/PS1 mice.

Parameter	WT	APP/PS1
k (min^{-1})	0.002	0.007
$t_{1/2}$ (min)	290.4	98.6

Table 3.2. Kinetic parameters for first-order elimination of ^{125}I-insulin from brain-to-plasma in WT and APP/PS1 mice

Following the observation of significant differences in insulin binding and its exit rate constant from the brains of the two groups of mice, we examined the effect of competing amounts of unlabeled insulin on the rate of ^{125}I-insulin influx into the brains of the two groups. ^{125}I-insulin was administered intravenously into WT or APP/PS1 mice and three minutes later, 100, 250, 500 or 1000µg of unlabeled insulin (Humulin RU100©) were injected intravenously in the mice. Plasma pharmacokinetic assays and SPECT/CT imaging were conducted in separate

groups of similar, age-matched mice by the method described in 2.2.4. Upon construction of Gjedde-Patlak plots (Patlak, Blasberg, & Fenstermacher, 1983) (Fig. 3.7), we observed that the plots of ratio of brain to plasma concentrations of ^{125}I-insulin (C_b/C_p) to its exposure time in the plasma retained linearity for a longer period in WT mice as opposed to APP/PS1 (Fig 3.8) mice.

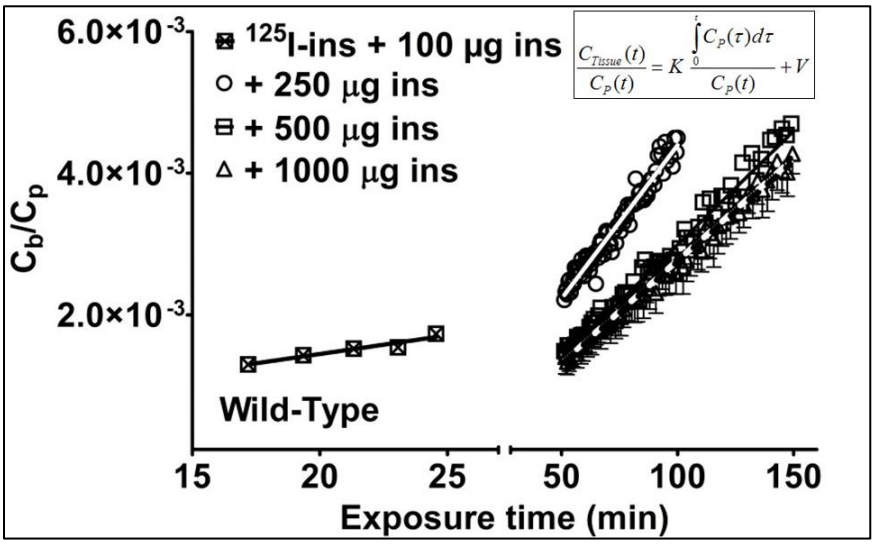

Figure 3.7. Patlak plots (Cb/Cp v/s exposure time) for WT mice administered with ^{125}I-insulin, followed by increasing amounts of unlabeled insulin after 3 minutes of injection.

Moreover, influx rate constants (slopes of regression lines in Fig. 1Ci and 1Cii) for ^{125}I-insulin at various amounts of unlabeled insulin were significantly greater for WT mice than APP/PS1 mice (Fig 3.9).

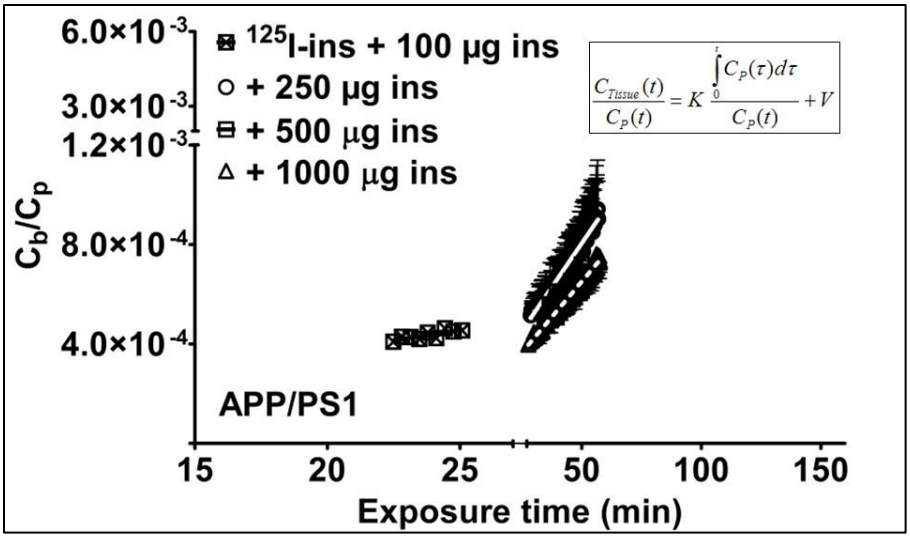

Figure 3.8. Patlak plots (Cb/Cp v/s exposure time) for APP/PS1 mice intravenously administered with ^{125}I-insulin, followed by increasing amounts (100, 250, 500 or 1000 µg) of unlabeled insulin after 3 minutes of injection.

Interestingly, the magnitude of suppression of influx rate constants for ^{125}I-insulin in the presence of increasing amounts of unlabeled insulin was more pronounced in WT mice as compared to APP/PS1 mice.

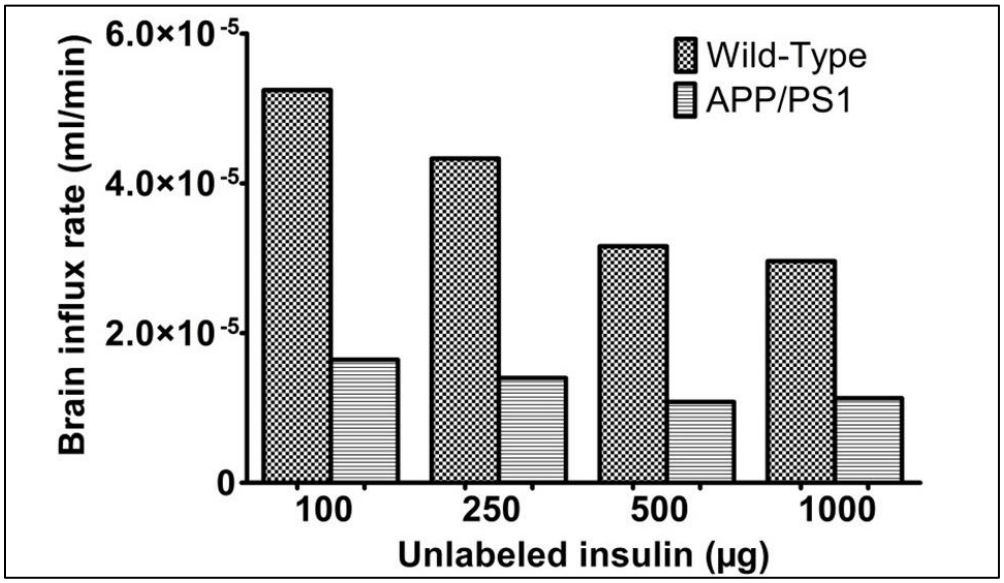

Figure 3.9. Bar graphs of brain influx rates of ^{125}I-insulin in response to administration of unlabeled insulin, derived from Patlak analyses. Slopes from linear regression lines of Patlak analyses corresponding to WT and APP/PS1 mice in Figure 2.5 and Figure 2.6 respectively, are plotted as bar graphs.

Analysis of secondary pharmacokinetic parameters (clearance, AUC) obtained from fitting data with increasing amounts of unlabeled insulin to a two-compartmental model, revealed that the rate of saturation of peripheral clearance was much faster for APP/PS1 mice than that for WT mice. Increase in peripheral clearance of insulin from APP/PS1 is in contrast with decreased clearance observed in db/db mice. It is also in contrast with the clearance in ageing mice, which also decreases significantly as compared to young WT mice.

Since APP/PS1 mice are characterized by abnormal accumulatio of Aβ40 and Aβ42, the following assay was to study ^{125}I-insulin brain uptake and kinetics in the systemic circulation in WT mice infused with 500 µg of Aβ40 and Aβ42 over 60 minutes via the internal carotid artery. The internal carotid surgery is described in chapter 2. Following the infusion, 100 µCi of insulin was injected intravenously for biodistribution experiments and 500 µCi was injected for the SPECT/CT assay.

Parameter	SALINE	Aβ42	Aβ40	Statistics
CL (Mean ± SD) (ml/min)	0.71 ± 0.09	0.55 ± 0.07	0.44 ± 0.07	**P = 0.0001, F (2,14) =18.33
AUC (Mean ± SD)	141.93 ± 17.4	172 ± 16	222 ± 29	**P < 0.0001, F (2,14) =

(µCi.min/ml)				21.6

Table 3.3 Clearance and AUC of intravenously injected ^{125}I-insulin in WT mice pre-treated via the internal carotid with an infusion (500 µg/60 mins) of Aβ40 or Aβ42. Parameter estimates for clearance and AUC were obtained from two-compartmental analyses of data averaged from the plasma concentration profile of WT pre-treated with saline (n=7) Aß40(n=5) and Aß42(n=5).

When the data was fit to a two-compartmental model on SAAMII and kinetic parameters of interest were simulated, it resulted in a discovery of differences in the clearance, AUC and the rate constants of transfer between the plasma and tissue for the two groups of mice. When data from biodistribution and SPECT/CT assays were plotted in form of a Patlak plot, we observed that the influx rate constant was decreased for ^{125}I-insulin, both when Aβ40 as well as Aβ42 were infused into the internal carotid artery.

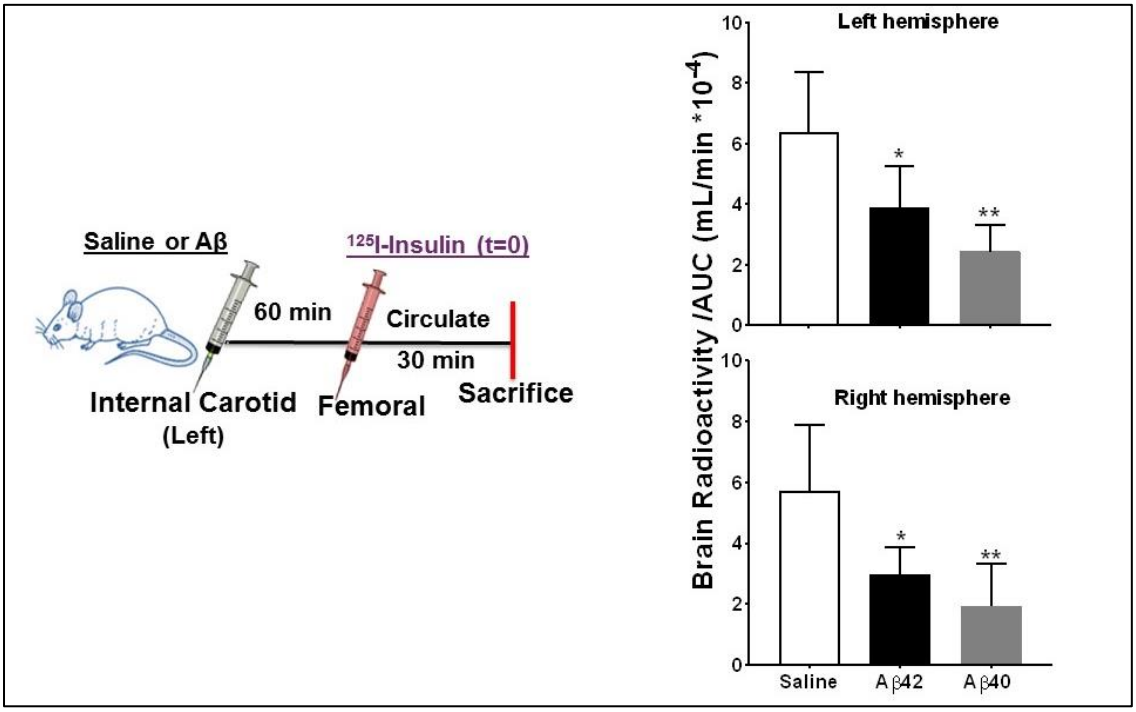

Figure 3.11. The brain radioactivity/AUC (mL/min*10^{-4}) values in WT mice following 30 minutes of an injection with ^{125}I-insulin with or without a pre-infusion (500 µg over 60 minutes) of Aß40 or Aß42 via the internal carotid artery.

Having measured insulin kinetics in brains of mice known to exhibit Aß peptides or acutely induced with Aß peptides, we wanted to probe insulin kinetics in brains of mice understood to be resistant to insulin uptake, thus serving as a positive control. To that effect, we employed leptin receptor deficient (db/db) mice which are obese and display high levels of plasma insulin. Confirming our hypothesis, db/db mice exhibited a decreased influx clearance of insulin into the brain as compared to corresponding control (db/-) mice, when analyzed through Patlak plots.

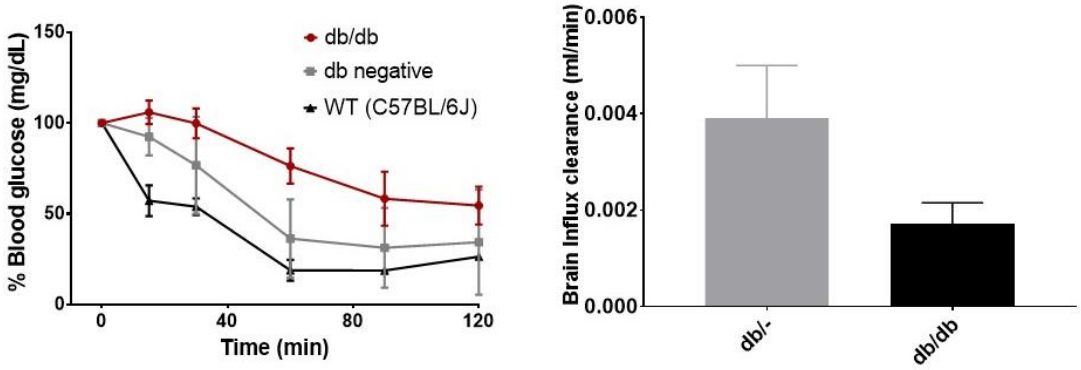

Figure 3.12. Peripheral tolerance and brain influx clearance of insulin in db/db mice in comparison with control db/- mice.

Further, simulations of the plasma data in a two-compartmental model run on initial estimates of the volume of distribution and inter-compartmental kinetic rate constants of transfer, showed that the db/db mice had a lower clearance and a higher AUC of insulin in the plasma.

Parameter	db/db	db/-
CL (Mean ± SD)	0.46 ± 0.04	0.75 ± 0.02

AUC (Mean ± SD)	202.6 ± 13.06	128 ± 2.65

Table 3.4. Clearance and AUC of intravenously injected ^{125}I-insulin in db/db and db/- mice. Parameter estimates for clearance and AUC were obtained from two-compartmental analyses of data averaged from the plasma concentration profile of db/db (n=4) and db/- (n=2) mice.

Studies have proven that aged human patients have a lower clearance of insulin from plasma compared to young patients. These results have been corroborated by our findings in mice wherein 24-month old mice depict a significantly lower clearance than the 3-month-old WT mice. Further, the AUC of insulin in the plasma was significantly higher than that for BSA and the beta half-life of insulin was significantly higher in young WT mice.

Parameter	Young	Aged
CL (Mean ± SD) (ml/min)	0.72 ± 0.05	0.41 ± 0.04
AUC (Mean ± SD) (µCi.min/ml)	116.3 ± 4.14	186 ± 7.37

Table 3.5. Clearance and AUC of intravenously injected ^{125}I-insulin in young and aged mice. Parameter estimates for clearance and AUC were obtained from two-compartmental analyses of data averaged from the plasma concentration profile of 3-month old WT (n=2) and 24-month old (n=3) mice.

3.6 Discussion

The purpose of assays conducted in this chapter was to understand the mechanistic link between peripheral distribution and brain accumulation of insulin in AD mouse models. The methodology incorporated studies with diabetic model mice and aged mice to obtain an indirect comparison between insulin distribution in AD and hyperinsulinemia.

APP/PS1 transgenic mice demonstrated significant peripheral tolerance to insulin, 15 and 30 minutes post-injection. Leptin receptor-deficient db/db mice also displayed tolerance to insulin, while published literature suggests that aging contributes to elevated plasma insulin levels and insulin resistance in mice (Templeman et al., 2017). Two-compartmental analysis of plasma concentration profile data generated from biodistribution assays proved that plasma clearance of insulin in APP/PS1 was excessively greater than that in WT mice. This suggested a distinct mechanism of a lack of peripheral insulin availability in APP/PS1 as compared to db/db mice, aged mice or mice pre-administered with Aβ40 or Aβ42.

Dynamic SPECT analysis of intravenously administered ^{125}I-insulin (Figure 3.3) revealed a decreased initial rate of uptake of insulin by brains of APP/PS1 mice. Patlak analysis of linear unidirectional uptake of ^{125}I-insulin into the brain (Figure.3.4) depicted a three-fold decrease in brain influx rate constants for ^{125}I-insulin in APP/PS1 as compared to those in WT mice. Further, the first-order exit rate constants for ^{125}I-insulin (Figure 3.7) from the brain were significantly higher for APP/PS1 mice as compared to WT mice. These indicate that the uptake mechanisms were significantly inhibited and the efflux mechanisms were significantly over-activated in the treatment mice groups.

Lowered influx coupled with increased efflux into the brain led us to speculate that uptake processes in APP/PS1, db/db and aged WT mouse brains are rapidly saturated. The fact that Cb/Cp values obtained from multiple regression analyses (Patlak plots) remained linear for a shorter period for APP/PS1 mice could be

interpreted as a compromise in the capacity of APP/PS1 brains to assimilate insulin linearly in presence of competing insulin. In summary, kinetic observations from biodistribution and brain uptake data in AD and hyperinsulinemia model mice lead to an inference that peripheral tolerance to insulin results in a decreased brain availability of insulin. The reason for the inhibited mass transfer of insulin into the brain in AD models overexpressing Aβ40 and Aβ42 could be due to an abnormal reactivity of the cerebrovascular endothelium surrounding the brain. The BBB endothelium could either be characterized by either a decreased pool of insulin receptors or a steady pool of desensitized receptors.

The impact of cerebrovascular insulin receptor sensitivity on the brain uptake of insulin will be addressed in chapters 5 and 6. Processes of insulin transport i.e. binding, receptor-mediated uptake and transcytosis will be examined in cerebrovascular endothelial cells as a function of presence of Aß peptides.

CHAPTER 4. PREDICTING BRAIN ACCUMULATION OF Aβ40, Aβ42 AND INSULIN IN MOUSE MODELS THROUGH MULTI-COMPARTMENTAL ANALYSIS

4.1 Synopsis

The previous two chapters discussed the utility of multiple-time regression analyses (Patlak plots) in measuring rates of insulin clearance into the brain. The inherent assumption of unidirectional brain tissue transfer in Patlak analysis renders it unfeasible to assess distribution of tracer from a plasma (reference compartment to peripheral tissues. Influx clearances derived from Patlak analyses only serve as initial estimates for more physiologically relevant predictions of insulin distribution. A multi-compartmental model of insulin and Aβ peptide distribution which accounts for brain as well as peripheral tissue distribution of the systemically-administered dose is required to obtain reliable estimates of distribution rate constants and pharmacokinetic parameters. It would present a structural framework to validate experimentally observed differences in organ distribution of tracer.

In this chapter, a three-compartmental model was constructed on SAAM II© to curve-fit tracer distribution (experimental data from Chapters 2 and 3) following a femoral vein administration of ^{125}I-Aβ40, ^{125}I-Aβ42 and ^{125}I-insulin. A delay compartment, representative of the BBB in-vivo, was constructed to minimize error in variance pertaining to predicted curve-fits of brain distribution data. Goodness of curve-fits were evaluated by diagnostic and visual predictive checks, and mean estimates of rate constants pertaining to predicted compartmental distribution values were input into Stella© to plot differences in tracer accumulation at the BBB, brain and peripheral tissues of respective mouse

groups. Results helped confirm graphically-derived patterns regarding the influence of insulin on Aβ40 and Aβ42 trafficking as well as the inhibition of insulin availability in the brain in all groups of insulin-resistant (APP/PS1, db/db, aged WT and Aß40 or Aß42 pre-treated WT) mice. Predicted brain AUC of ^{125}I-Aβ40 was 19% higher when mice were pre-treated with 1IU of insulin whereas that for ^{125}I-Aβ42 was 10% lower. Predicted brain AUC of ^{125}I-insulin was 98 %, 65%, 72% and 49% lower in db/db, aged WT, Aß40 treated and Aß42 pre-treated mice, respectively, in comparison with control mice groups. APP/PS1 mice were characterized by a decrease in brain AUC of intravenously-administered ^{125}I-insulin until 10 mins, however the data displayed significant scatter after 10 minutes, hence it is not reported in this chapter. Intriguingly, a decrease in brain AUC for insulin in insulin-resistant mouse groups was correlated with a peripheral tissue AUC for insulin, implications for which need to be investigated in future studies. Additionally, AUC of ^{125}I-insulin, ^{125}I-Aβ40 and ^{125}I-Aβ42 at the BBB increased proportionately with an increase in brain AUC, likely due to application of insignificantly different delay parameters in analysis of brain data for transgenic/treated and control mice. The impact of BBB on the brain accumulation will be delineated in further detail in-vitro.

4.2 Rationale: Insulin regulates glucose metabolism, cell proliferation, growth, lipid metabolism and cognition in the brain. The brain is a highly-perfused organ and receives systemically produced insulin through receptor-mediated transport across the microvascular endothelium, which is referred to as the blood-brain barrier (BBB) (Duffy et al., 1987). Intranasal insulin administration also assists in

reducing Aβ deposits in Alzheimer's disease patients. Chapter 2 of this thesis has described the mediatory effects insulin on Aβ40 and Aβ42 peptide trafficking from the plasma-to-brain and vice versa. Variations in insulin-mediated metabolism are understood to trigger pathophysiological complications such as insulin resistance, a precursor to Type-2 diabetes or Alzheimer's disease (AD). Research from the last decade has shown that brain insulin levels in AD patients at progressive stages of the disease are significantly reduced relative to the brains of age-matched non-demented individuals (Rivera et al., 2005; Talbot et al., 2012). This decrease can be attributed either to a decrease in insulin trafficking from the periphery to brain via the BBB, or due to a decline in the capacity of certain brain regions to synthesize insulin. The insulin-synthesizing capacity of the brain remains unresolved (conflicting evidence on the translation of insulin mRNA found in brain regions), however the mechanistic link between systemically administered insulin and the brain appearance of insulin was delineated in chapter 3 of this thesis. It unequivocally demonstrated that brain availability of insulin in insulin-resistant AD model mice and Aβ-treated WT mice is due to decreased rate of influx from the peripheral circulation and increased rate of efflux from the brain. It is therefore likely that the BBB dysfunction in the AD brain restricts insulin supply to the brain.

In general, AD models are characterized by the over-accumulation of amyloid-beta (Aß) peptides in the plasma as well as in the brain parenchyma (Mawuenyega et al., 2010). Previous publications have underscored the significance of the BBB in maintaining the dynamic equilibrium of Aß proteins in

brain and plasma compartments (Kandimalla KK et al., 2005). The BBB dysfunction is believed to shift this equilibrium and trigger anomalous amyloid accumulation in the AD brain. Based on these evidences, it can be hypothesized that Aß isoforms modulate interactions of insulin with the BBB endothelium, thereby affecting its subsequent transcytosis into the brain parenchyma. Hence, to fully resolve the mechanisms of brain insulin resistance, it is critical to investigate trafficking and signaling mechanisms of insulin at the BBB, in context of enhanced Aß peptide exposure.

However, a critical pre-requisite to understanding the effects of Aß peptide exposure of insulin uptake would be development and validation of a model for observations concerning Aβ peptide and insulin transport into the brain tissue in healthy and insulin-resistant mouse models. This would assist in identifying rate-limiting steps to several processes involved prior to appearance of insulin in the brain. Inferences drawn from sensitivity analyses of these rate-limiting steps would assist in informing design for future studies focused on the effect of Aß peptides on insulin transport and vice-versa, into the brain in AD models.

The methodology of studying brain uptake in chapter 2 and 3 was through a derivation of SPECT/CT data for ^{125}I- insulin, ^{125}I-Aβ40 or ^{125}I-Aβ42 following injection via the femoral vein. Now, the femoral vein transports blood to the heart, which pumps blood to the left and right cerebral hemispheres of the brain via the internal carotid artery. It does not ensure uninhibited transfer of peptide into the brain due to the possibility of metabolism of fractional doses by the liver. The SPECT/CT data provided information on transient kinetics of insulin in AD versus

Wild-Type mice brains. Patlak plots or two-compartmental models of tissue transfer were constructed in chapter 3, to calculate the unidirectional rate constants of brain uptake. The unidirectional rate constants of brain uptake were significantly lowered in mouse models of insulin resistance. Urayama et al have conducted multiple-time regression or Patlak analysis to prove that the influx clearance values for insulin in obese mice is significantly lower than in thin mice. Moreover, as described in chapter 2 and 3, Swaminathan et al, 2017 have applied Patlak analysis to obtain influx clearance values for Aß40 and Aß42 into the brain. Unidirectional fluxes into the tissue compartment of two-compartmental models are useful measures of brain levels for a given compound administration when the brain data is available and analyzed. They are not accurate predictors, however, of tissue accumulation in the context of a multi-compartmental model.

In this chapter, multi-compartmental models with bidirectional rate constants would be constructed to fit the brain and plasma pharmacokinetic data emerging from studies described in Chapter 3. This would be to determine differences in the bidirectional rate constants of brain and tissue uptake between young and aged WT mice, APP/PS1, db/db mice and WT mice infused with pathological amounts of Aβ40 and Aβ42. The model for insulin kinetics in this report would be developed based upon the protocol for the in-vivo SPECT/CT experiment described above. The results gained from simulations of this model would be used to predict amounts of insulin in the brain over an extended time frame. Based on the results, possible mechanisms for differences observed in the brain,

tissue and plasma concentration profiles simulated from the SPECT/CT and plasma pharmacokinetic studies, respectively, will be discussed.

4.3. Aim: To understand the relation between organ distributional rate constants obtained by three compartmental model simulations of plasma and brain insulin disposition data in various groups of mice (young WT, aged WT, APP/PS1, db/db, db negative). The objective is to simulate the brain accumulation over 45 minutes by using influx parameters obtained from 3 compartmental analyses.

4.4. Method of simulation:

4.4.1 Construction of the three-compartmental model: Simulation, analysis and modeling (SAAM2) software was used to construct a three-compartmental model as follows:

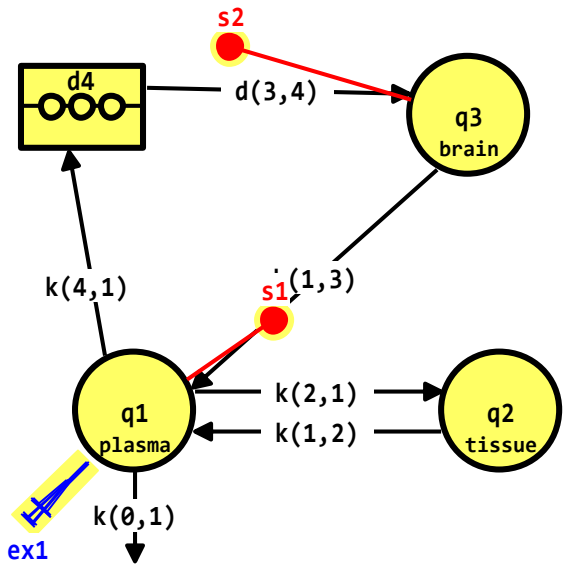

Figure 4.1. Compartmental model on SAAM II© depicting the exchange of tracer between plasma, tissue and brain.
The in-built SAAM II© equations for this model are :

d(3,4) = 1.0

k(3,4) = d(3,4) * (delay time)/(no. of delay compts)

flux(3,4) = k(3,4) * d4/(no. of delay compts)

flux(4,1) = k(4,1) * q1

flux(1,2) = k(1,2) * q2

flux(1,3) = k(1,3) * q3

flux(2,1) = k(2,1) * q1

flux(0,1) = k(0,1) * q1

ex1.bolus = 0.0

ex1.infusion = 0.0

s2 = q3

s1 = q1/V

The rate of change of concentration within each compartment is as follows:

1. $\frac{dCp}{dt} = k(1,2) * Ct - k(2,1) * Cp + k(1,3) * Cp - k(4,1) * Cp - k(0,1) * Cp$

2. $\frac{dCt}{dt} = k(2,1) * Cp - k(1,2) * Ct$

3. $\frac{dD4}{dt} = k(4,1) * Cp - k(3,4) * d4$

4. $\frac{dCb}{dt} = k(3,4) * \frac{d4}{no,of\ delay\ compts} - k(1,3) * Cb$

The rate constants are defined such that the first number inside the parentheses denotes the receiving compartment and the second number inside the parentheses denotes the donor compartment.

The parameter k(1,2) denotes the tissue to plasma rate of mass transfer. k(2,1) denotes the rate of transfer from the plasma to the tissue compartment. k(3,1) denotes the rate of transfer from the plasma to the brain. k(0,1) represents the rate constant of elimination from the central compartment. k(4,1) represents the

transfer rate constant into the delay compartment, denoted as d4. k(0,3) did not lead to good estimates of Cb or brain uptake curves, hence they were eliminated from the further iterations of model fits.

The delay compartment is utilized to curve-fit data which progresses at a slower rate than that accounted for by a two-compartmental transfer rate constant. The internal transfer coefficient and the delay width are calculated by the SAAM II© program from the inputs assigned for number of supposed internal compartments and delay time. Increasing the number of compartments leads to a decrease in the delay width i.e. it approximates a true delay by improving the resolution of the delay; however more the number of compartments, greater is the time required to solve the equations and reach convergence. With respect to computational settings, the number of calculation intervals was fixed at 500 and the experimental time was set to 30 or 40 minutes depending upon the goodness of fit. The Rosenbrock integrator was selected as the differential equation solver and a relative variance model was chosen. The convergence criterion was set to 0.000001.

4.4.2 Normalization of SPECT/CT brain distribution data: As measured total brain amounts (µCi) are a sum of the radioactivity arising from parenchymal and vascular components, final tracer radioactivity data for ^{125}I-insulin, ^{125}I-Aβ40 or ^{125}I-Aβ42 were corrected to exclude the residual vascular component in the brain ROI. This was achieved by multiplying predicted plasma concentrations at each time point by a scaling factor (accounts for the volume of distribution in the vasculature of a given mouse). In the current studies, the newer SPECT

instrument was employed. The scaling factor was applied such that the resultant brain parenchymal amount at time zero, obtained by subtracting the vascular amounts from the total amounts at time zero, would be a value approximately equal to zero. Scaling of the data by this technique ensured that the brain parenchymal amounts converged with the observed total brain amounts at later time points. It is to be noted that due to better accuracy of post-perfusion ROI measurement in the old SPECT/CT instrument at Mayo Clinic), vascular volume of distribution for figure 3.3 was calculated by dividing the brain vascular amount (obtained by subtracting post-perfusion parenchymal amount from total amount at last measured time point).

4.4.3 Assumptions: The assumptions underlying this model were:

1. A reversible exchange of insulin and Aβ40/42 occurs between the plasma, tissue, and brain.

2. Delay compartment is assumed to represent the BBB in a physiological scenario. Mass exiting the BBB is completely transferred to the brain unless a minimization of error in variance (weighted residuals) required the application of a fractional egress into the plasma compartment

3. The rate constants are derived from first order rate equations

4. The initial estimates for k(1,2), k(2,1) and Vp were obtained from a priori information generated from curve-fitting the plasma decline of administered ^{125}I-insulin. Influx clearances obtained from Patlak plots of data from WT, APP/PS1, aged WT, db/db, and Aß40 or Aß42 pre-treated

mice were divided by the volume of distribution to generate initial estimates for k (4,1). Elimination rate constants obtained following intracerebral injection of ^{125}I-insulin were used to set initial parameters for k (0,1).

5. The compartments are either homogenously distributed, as is the assumption with Patlak analyses.

6. There is negligible metabolism of the ^{125}I-tagged insulin in the time frame of plasma sampling. Moreover, the insulin is tagged to the ^{125}I-iodine with an efficiency greater than 90% in the time-frame of sampling. Hence no correction to the data was done.

7. There is a constant variance between observations (homoscedasticity)

4.4.4 Diagnostics for the compartmental model: Goodness of fit is determined by the following measures: Akaike Information Criterion (AIC), Bayesian Information Criterion (BIC) and Coefficient of Variation (CV) of the predicted parameters. Lower AIC, BIC and CV signify a better fit to the data. The variance in the data points is assessed by observing diagnostic plots of the sum of squared residuals and the weighted sum of squared residuals.

4.5 Results

^{125}I-Aβ40 and ^{125}I-Aβ42 distribution in response to insulin administration in WT mice: With respect to ^{125}I-Aβ40 trafficking from plasma to brain, predicted parameters displayed a significant increase for k(4,1) i.e. the BBB uptake rate constant, when mice were pre-treated with 1IU of insulin over a period of 15 minutes. Similarly, k(2,1) i.e. the peripheral tissue uptake rate constant was

higher for a ^{125}I-Aβ40 flux in response to insulin administration. k(1,3), k(1,2) and k(0,1) were not significantly different between the insulin and saline pre-treated groups. These findings confirmed the patterns suggested by two-compartmental biodistribution analyses as well as Patlak analyses of unidirectional rate of transfer of ^{125}I-Aβ40 from the plasma to the brain (figure 2.1 and figure 2.3). The curve-fits from brain and plasma data for the ^{125}I-Aβ40 study analyses are plotted in figure 4.2.

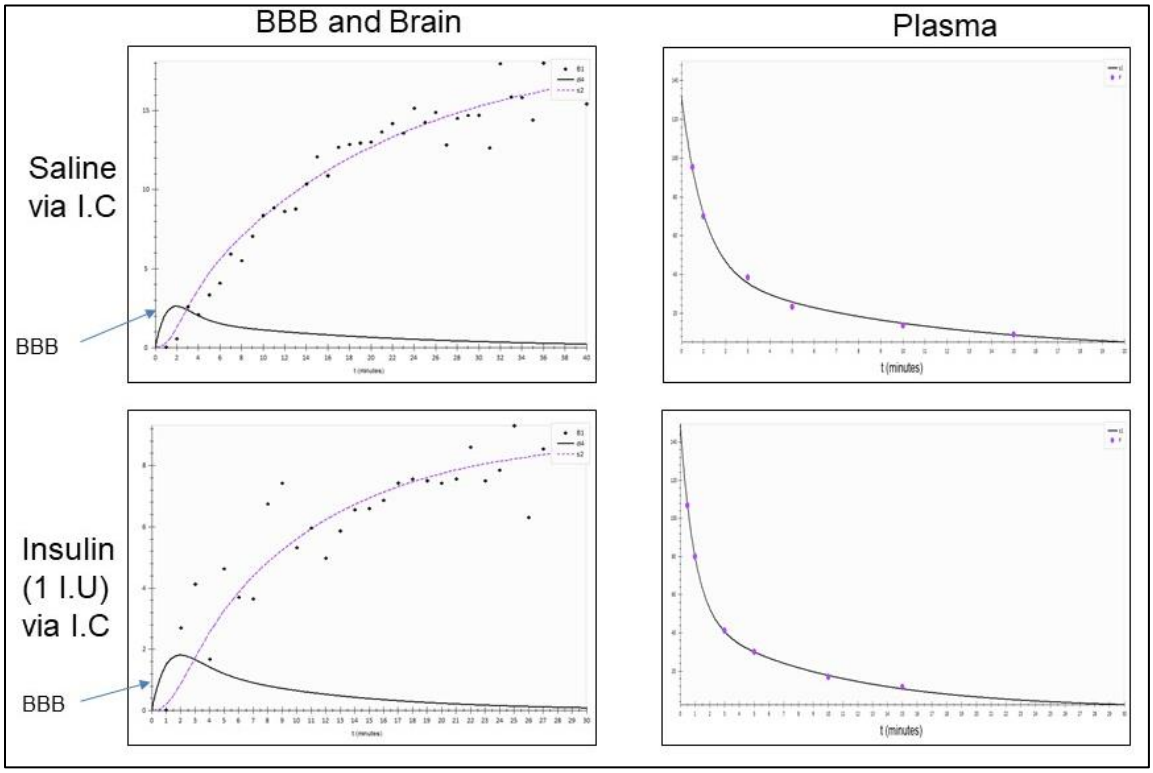

Figure 4.2: Representative curve-fits of observed values of ^{125}I-Aβ40 BBB, brain and plasma distribution following a pre-treatment with either saline or insulin (1 I.U) via the internal carotid. The connecting curve is the predicted curve fit and the closed circles represent the observed values.

In case of ^{125}I-Aβ42, the predicted parameters revealed that k(4,1) was significantly lower for insulin pre-treated mice as compared to the saline-treated control WT mice. Moreover, rate constants for tissue distribution (k(2,1)) and

elimination from the plasma compartment (k(0,1)) were significantly lowered for the insulin pre-treated group. These results agree with two-compartmental analyses of biodistribution and Patlak analyses of brain influx clearance of ^{125}I-Aβ42 demonstrated in figure 2.1 and figure 2.3. BBB, brain and plasma concentration-time profile for observed and predicted values for the saline or insulin pre-treated ^{125}I-Aβ42 groups are plotted in figure 4.3. The differences in accumulation of the tracer in the BBB, brain and tissue are evident upon quantification of the AUC, as tabulated further in this chapter.

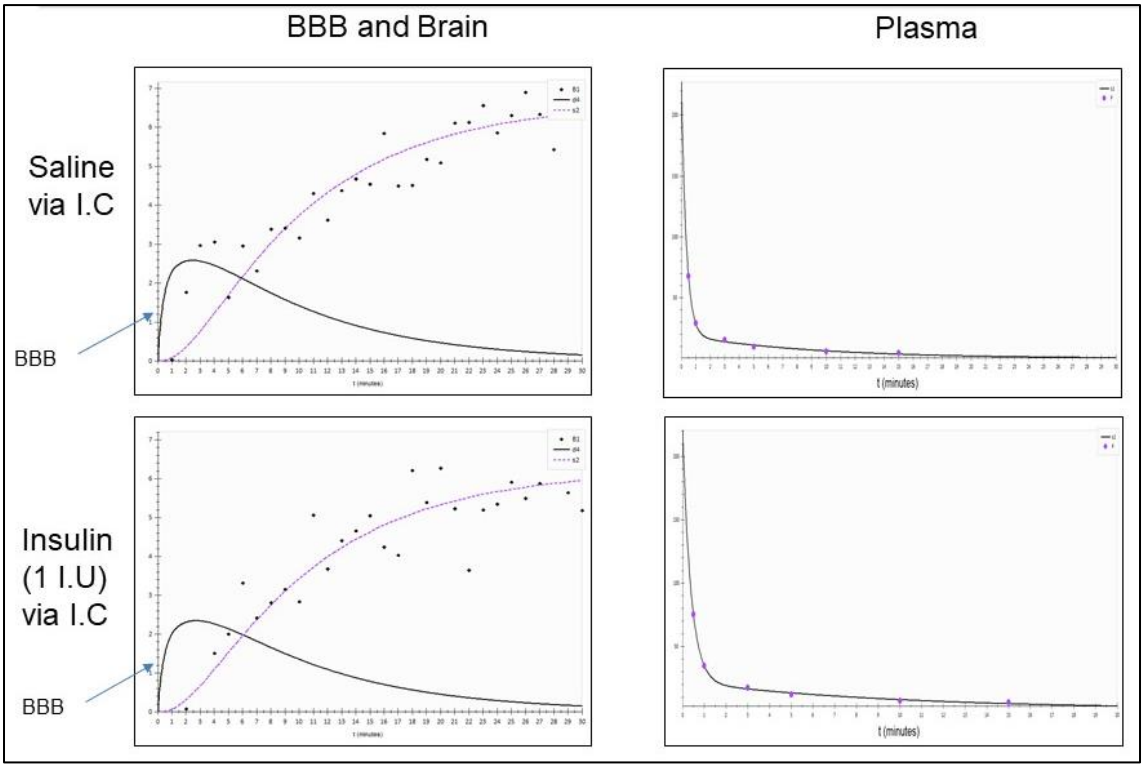

Figure 4.3: Representative curve-fits of observed values of ^{125}I-Aβ42 BBB, brain and plasma distribution following a pre-treatment with either saline or insulin (1 I.U) via the internal carotid. The connecting curve is the predicted curve fit and the closed circles represent the observed values

Tabulated format of Stella©-derived predicted values (table 4.1) for ^{125}I-Aβ40 and ^{125}I-Aβ42 distribution in saline or insulin pre-treated WT groups prove that the

tissue AUC for ^{125}I-Aβ40 is decreased by 49.25%, whereas that for ^{125}I-Aβ42 is increased by 18% in insulin-treated WT mice. On the other hand, AUC in the brain tissue for ^{125}I-Aβ40 is increased by 19% while that for ^{125}I-Aβ42 is decreased by 10% in insulin-treated WT mice.

	^{125}I-Aβ40			^{125}I-Aβ42		
PARAMETERS	*Saline*	*Insulin*	Stats	*Saline*	*Insulin*	Stats
k(4,1) (min^{-1})	0.004	0.006	N.S	0.012	0.009	**, P<0.01
k(1,3) (min^{-1})	1e-09	1e-09	N.S	1e-09	1e-09	N.S
k(2,1) (min^{-1})	0.45	0.46	N.S	1.72	1.48	***,P<0.001
k(1,2) (min^{-1})	0.26	0.4	N.S	0.36	0.35	N.S
k0,1) (min^{-1})	0.22	0.25	N.S	0.95	0.75	**,P<0.01
AUC(plasma) (µCi.min)	532.22	489	n/a	203	230.3	n/a
AUC(tissue) (µCi.min)	745.57	453	n/a	494	583	n/a
AUC(brain) (µCi.min)	56.54	74.81	n/a	48.5	38.4	n/a
AUC(blood-brain barrier) (µCi.min)	3.44	4.27	n/a	6.18	5.7	n/a

Table 4.1. Estimated rate constants from SAAM II© , predicted amounts and AUC (0 to 45 mins) for plasma, tissue, BBB and brain for 125I-Aβ40 and 125I-Aβ42 administered through the femoral vein WT mice pre-infused with saline or 1IU of insulin via the internal carotid artery. The dose administered is 100 µCi through the plasma compartment.

Brain amounts predicted on Stella© over a period of 45 minutes based on the mean values of estimates for rate constants obtained from SAAM II© are plotted for ^{125}I-Aβ40 and ^{125}I-Aβ42 in figure 4.6. Brain profiles suggest an enhancement of brain AUC as observed from the predicted AUC values for insulin pre-treated WT mice administered with ^{125}I-Aβ40. For ^{125}I-Aβ42, the brain amount profiles reflect a smaller yet distinct separation, which is in alignment with the brain AUC values calculated over 45 minutes.

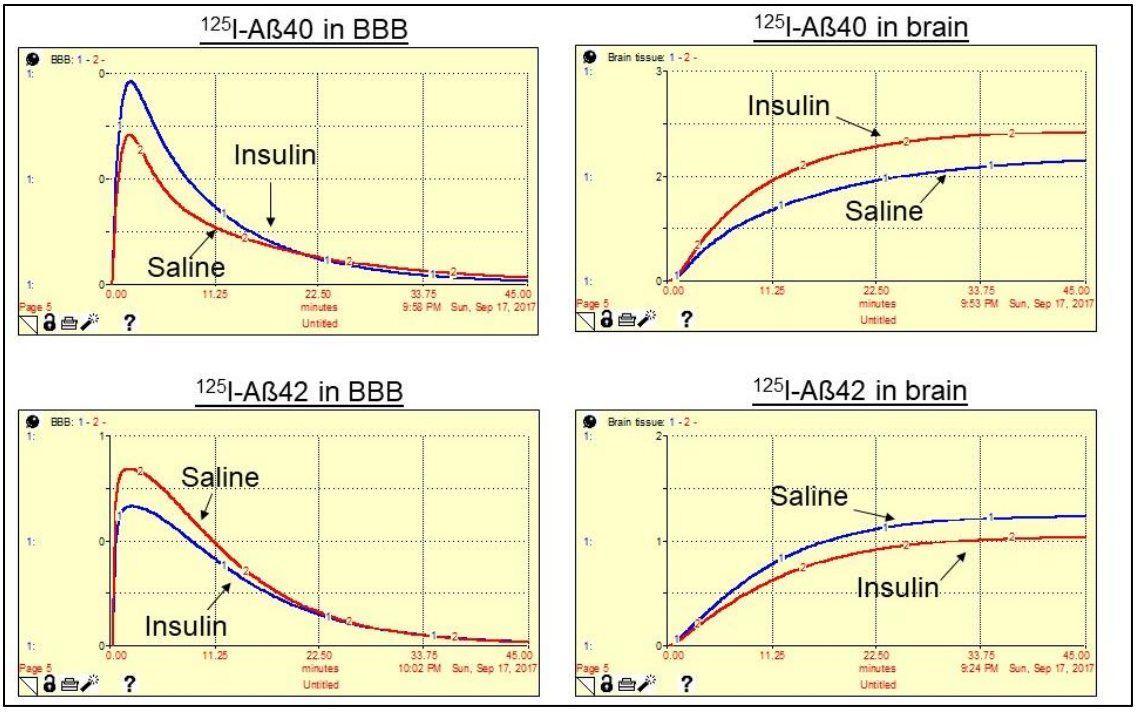

Figure 4.4: Predicted BBB and brain amount differences for ^{125}I-Aβ40 (left) and ^{125}I-Aβ42 (right) in saline or insulin-pre-treated WT mice following administration of 100 µCi into the plasma compartment of a 3-compartmental model (Stella©)

Insulin distribution in insulin-resistant mice: Insulin kinetics were predicted in four groups of mice: a) young v/s aged b) WT v/s APP/PS1 c) db/db vs db/- d) saline v/s Aβ40 or Aβ42 treated WT mice. For the first group (young vs aged WT mice), data from the plasma pharmacokinetic studies and brain SPECT of ^{125}I-insulin femoral administration in young (4-month old mice) and aged (24-month old mice) was simulated.

Intriguingly, in agreement with the Patlak linear regression analysis of the data from the same study as described here, the brain uptake rate constant (k(3,1)) was significantly decreased in aged mice as compared to that in young mice.

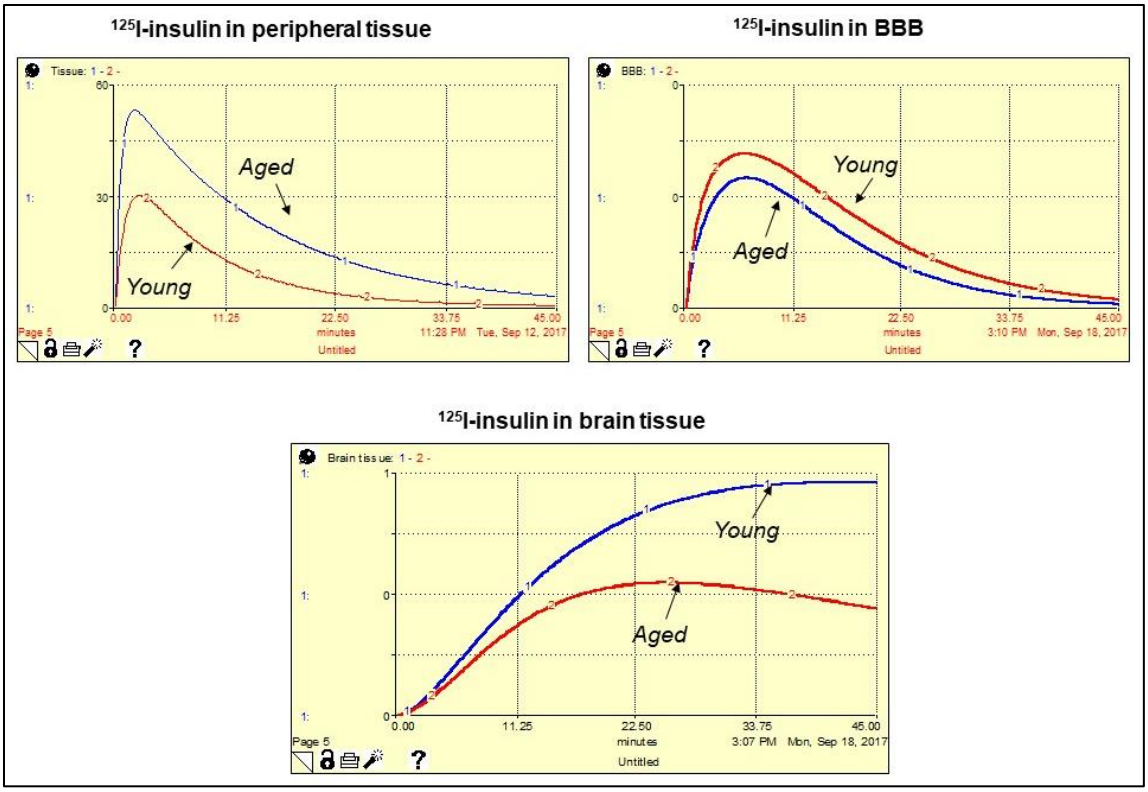

Figure 4.5: Predicted BBB, brain and tissue amount differences between aged and young mice following insulin administration (100 µCi) into the plasma compartment of a 3-compartmental model (Stella©)

Similarly, the k(1,3) for insulin elimination from brains of young mice was significantly lower than that compared to aged mice. Intriguingly, the tissue uptake rate constant (k(2,1)) was significantly higher for older mice as compared to young mice.

In the second group (WT vs APP/PS1), simulations for time points greater than 10 minutes were marked by excessive variability, therefore only the brain AUC comparison between WT and APP/PS1 for the time period until 10 minutes is depicted in the appendix section.

In the third group (db/- vs db/db), k(4,1) was higher for db/- mice whereas k(2,1) and k(1,3) were significantly higher in db/db mice. k(0,1) and k(1,2) were not

significantly different between these groups. The curve-fits for brain, BBB and plasma for db/- and db/db mice are displayed in the appendix section.

Predicted brain amount profiles for db/db mice (figure 4.11) described a slower uptake, attributable to a lower k (4,1). It displays a clearance mechanism as time progresses until 45 minutes owing to an increased brain elimination rate and increased tissue distribution rate constants as compared to the db/- mice.

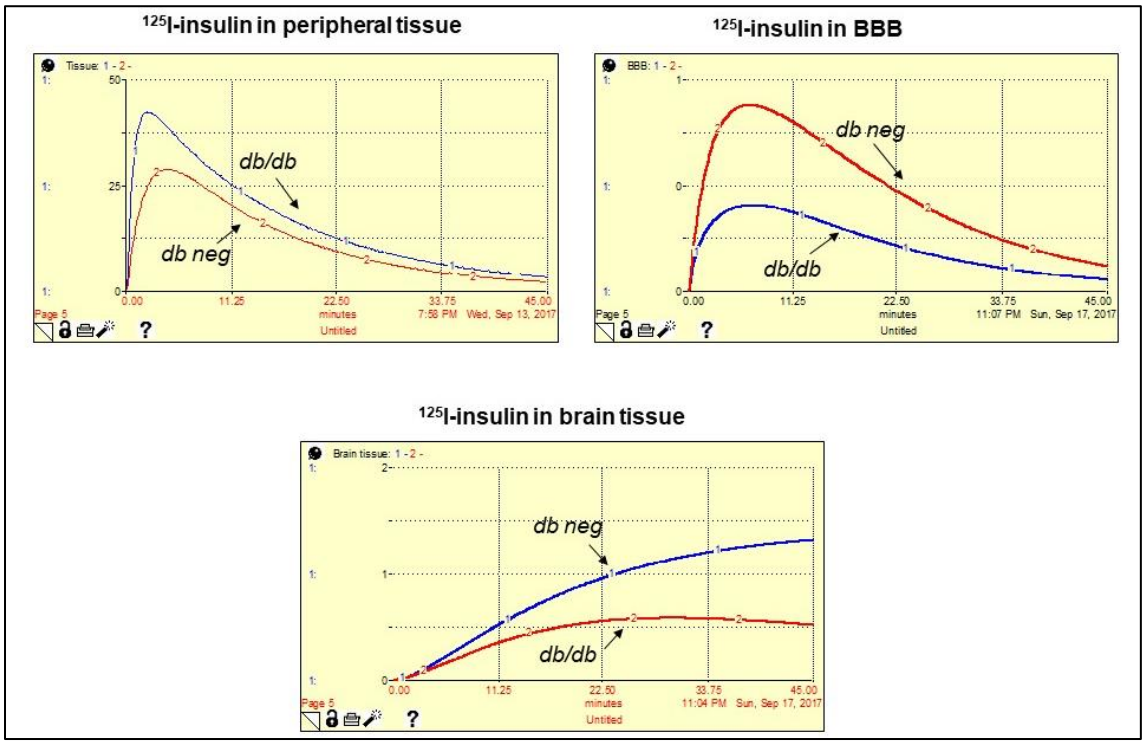

Figure 4.6. Predicted BBB, brain and peripheral tissue amount profiles for ^{125}I-insulin in db/db and db/$^{-}$ mice following administration of 100 µCi into the plasma compartment of a 3-compartmental model (Stella©)

In the fourth group (Saline pre-treated vs Aß40 or Aß42 pre-treated), k(3,1) and k(2,1) were significantly higher while k(1,3) and k(1,2) were significantly smaller for saline-treated WT mice in comparison with Aß40 pre-treated WT mice.

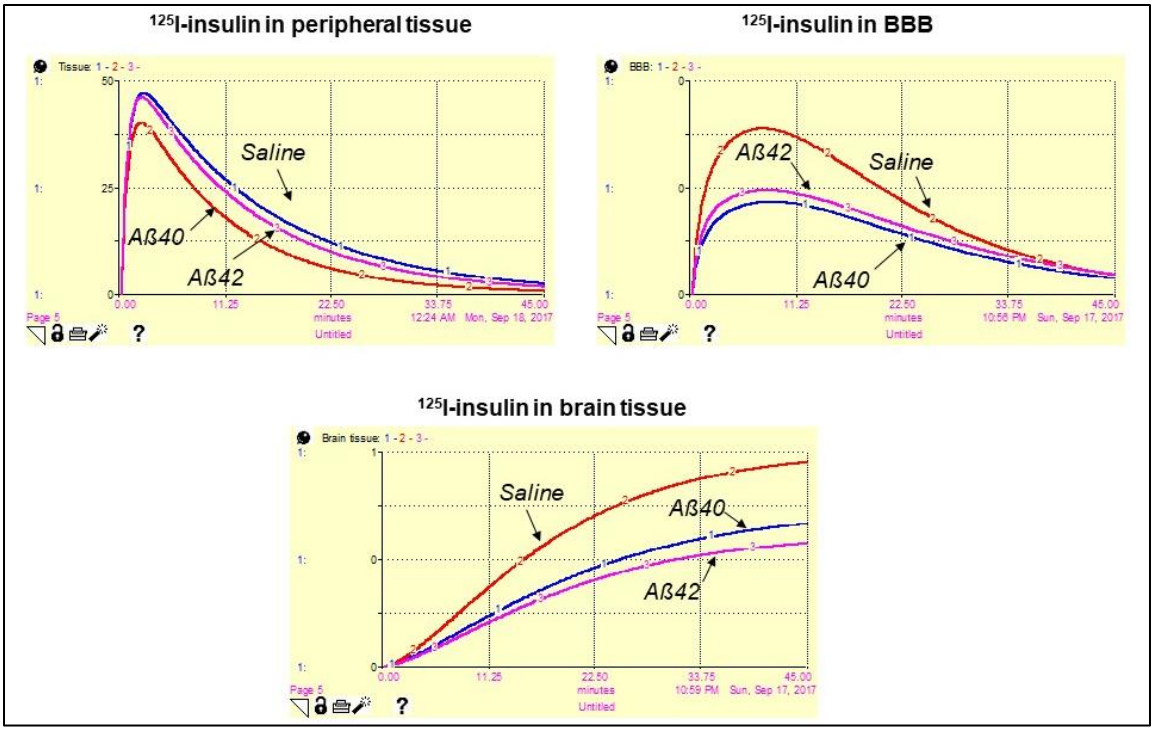

Figure 4.7: Predicted brain and tissue amount differences between WT pre-treated with saline or Aβ40 followed by insulin administration (100 µCi) into the plasma compartment of a 3-compartmental model (Stella©).
In case of Aß42 pre-treated mice, ^{125}I-insulin did not portray significantly different k(1,3), k(1,2) or k(2,1) as compared to the controls, but the k(3,1) was significantly lower as observed with db/db and aged mice.

Representative plots for the observed versus predicted fits, the sum of squares of residuals for predicted fits for plasma and brain distributions are displayed in the appendix section of this thesis. The estimated rate constants are tabulated in tables 4.1 through 4.5.

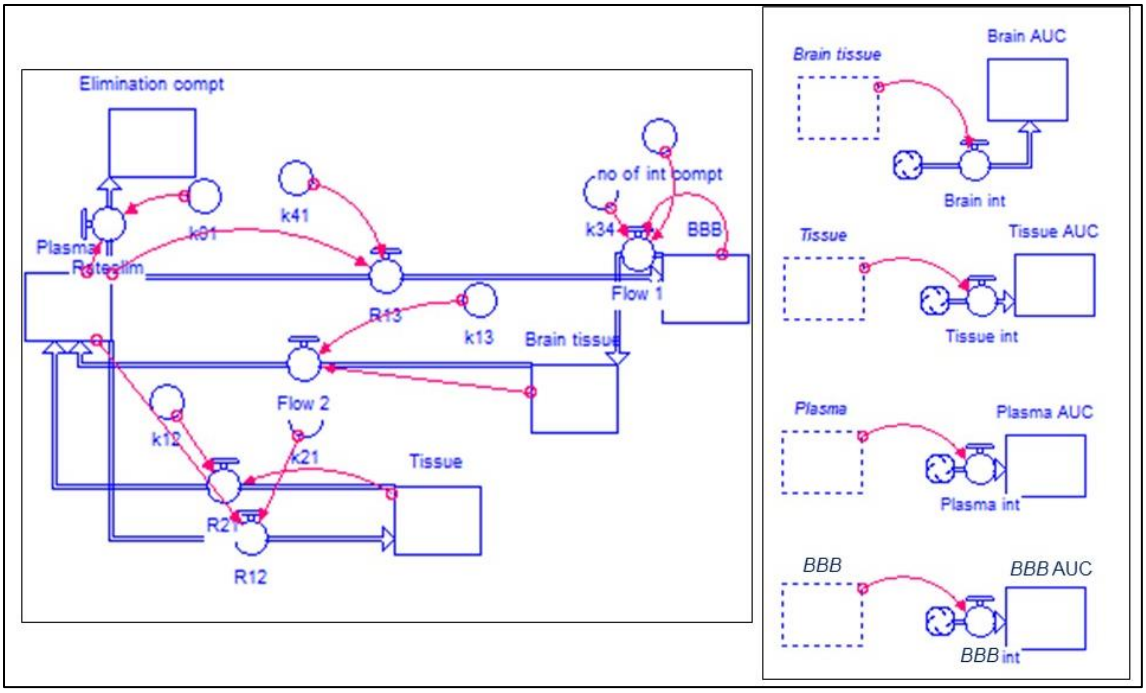

Figure 4.8. Image on the left is a four-compartmental (including BBB and excluding the elimination compartment) model on Stella©. Image on the right are processes constructed to integrate the plasma, tissue, BBB and brain amounts to calculate their respective AUCs.

Built-in equations characterizing the Stella© compartmental model displayed in figure 4.14 are specified in the appendix. Estimated rate constants appropriate for a given group of mice were input into the Stella© model and the model was run on a Euler's integration method with a plasma dose of 100 μCi until t=45 minutes, and at intervals (DT) of 0.2 minutes. Predicted plasma amount profiles for all groups intriguingly showed that the control mice eliminated insulin faster than the insulin-resistant db/db, aged or Aβ40/Aβ42 treated mice (figure 4.8).

Brain amounts for young WT mice suggested a higher k(3,1) and a lower k(1,3) in agreement with the predicted values from SAAM II©. For aged WT mice, the brain amounts were visibly dictated by slower k(3,1) and faster k(1,4), whereas in the case of saline-treated mice in the fourth group, the steady increase in brain

levels over 90 minutes were governed by an almost negligible elimination rate from the brain.

Brain AUC for respective groups are tabulated in tables 4.2 through table 4.4. Tabulated values for rate constants serve to obtain a measure of the relation between brain AUC and corresponding brain uptake rate constants. It can be observed that differences in brain AUC between treatment/disease or control groups do not correlate accurately with values for k(3,1) and k(1,3). Brain AUC levels depend on the values for tissue distribution rate constants as well as the brain distribution rate constants.

PARAMETERS	YOUNG WT(n=3)	AGED WT(n=4)	STATISTICS
k(4,1) (min^{-1})	0.0014	0.0011	*, P<0.05
k(1,3) (min^{-1})	0.004	0.019	*, P<0.05
k(2,1) (min^{-1})	0.35	0.89	***, P<0.001
k(1,2) (min^{-1})	0.39	0.40	N.S
k(0,1) (min^{-1})	0.26	0.26	N.S
AUC (plasma) (µCi.min)	486	476.26	n/a
AUC (tissue) (µCi.min)	343	722.8	n/a
AUC (brain) (µCi.min)	15.56	9.38	n/a
AUC (BBB) (µCi.min)	4.31	3.21	n/a

Table 4.2. Estimated rate constants from SAAM II© , predicted amounts at the 45^{th} minute and AUC (0 to 90 mins) for plasma, tissue, brain for young or aged WT mice. The insulin administration is 100 µCi through the plasma compartment.

PARAMETERS	DB/- (n=5)	DB/DB (n=3)	STATISTICS
k(4,1) (min^{-1})	0.0023	0.0014	N.S
k(1,3) (min^{-1})	0.00026	0.023	*, P<0.05

k(2,1) (min^{-1})	0.20	0.62	****, P<0.0001
k(1,2) (min^{-1})	0.22	0.59	***, P<0.001
k(0,1) (min^{-1})	0.16	0.14	*P<0.01
AUC (plasma) (µCi.min)	520.66	725.88	n/a
AUC (tissue) (µCi.min)	680	863.52	n/a
AUC (brain) (µCi.min)	37.63	18.98	n/a
AUC (BBB) (µCi.min)	10.64	6	n/a

Table 4.3. Estimated rate constants from SAAM II© , predicted amounts at the 45th minute and AUC (0 to 90 mins) for plasma, tissue, BBB and brain for db— and db/db mice. The insulin administration is 100 µCi through the plasma compartment.

PARAMETERS	SALINE(n=3)	Aß40 PRE-INFUSED(n=3)	STATISTICS
k(4,1) (min^{-1})	0.0018	0.0011	* (one-tailed t-test), p<0.05
k(1,3) (min^{-1})	0.00001	0.0005	***, p<0.01
k(2,1) (min^{-1})	0.57	0.67	NS
k(1,2) (min^{-1})	0.39	0.37	**, p<0.01
k(0,1) (min^{-1})	0.29	0.26	NS
AUC (plasma) (µCi.min)	438.16	472.48	n/a
AUC (tissue) (µCi.min)	517.26	633.04	n/a
AUC (brain) (µCi.min)	17.56	10.21	n/a
AUC (BBB) (µCi.min)	4.69	2.86	n/a

Table 4.4. Estimated rate constants from SAAM II© , predicted amounts at the 45th minute and AUC (0 to 90 mins) for plasma, tissue, BBB and brain for saline and Aß40 pre-treated mice. The insulin administration is 100 µCi through the plasma compartment

PARAMETERS	SALINE(n=3)	Aß42 PRE-INFUSED(n=3)	STATISTICS

k(4,1) (min^{-1})	0.00177	0.0012	*, p<0.05)
k(1,3) (min^{-1})	0.00001	0.00001	NS
k(2,1) (min^{-1})	0.57	0.63	NS
k(1,2) (min^{-1})	0.39	0.30	NS
k(0,1) (min^{-1})	0.291	0.27	NS
AUC (plasma) (µCi.min)	438.16	497.84	n/a
AUC (tissue) (µCi.min)	517.26	833.1	n/a
AUC (brain) (µCi.min)	17.56	11.76	n/a
AUC (BBB) (µCi.min)	4.69	3.29	n/a

Table 4.5. Estimated rate constants from SAAM II© , predicted amounts at the 45th minute and AUC (0 to 90 mins) for plasma, tissue, BBB and brain for saline, Aß42 pre-treated mice. The insulin administration is 100 µCi through the plasma compartment

4.6. Discussion

A reduction of insulin uptake into brains of insulin-resistant obese mice and a reversal of this trend by prior starvation of the mice was reported by (Urayama & Banks, 2008). The authors applied multiple-time regression (Patlak) analyses to measure unidirectional clearance of insulin into the brain. In general, Patlak analyses are suitable for a reductionist two-compartmental understanding of molecular transport into tissues. However, utility of parameters obtained from Patlak analyses fails when translated to a physiologically-based pharmacokinetic scenario due to the presence of peripheral organs and backflows from these organs. Therefore, more holistic approaches of pharmacokinetic analyses are required to correlate the predicted parameters with a physiologically relevant set up.

There has been no report heretofore, about mass distribution of Aβ40 or Aβ42 in a multi-compartmental model or insulin based on insulin-resistant subjects. Findings in this chapter confirm the graphical multiple-time regression analyses obtained from studying the kinetics of plasma and brain distribution of Aβ peptides in response to insulin administration (chapter 2) and that of insulin itself (chapter 3), in various groups of mice disposed to insulin resistance by means of a 3-compartmental model analysis. The model was constructed on SAAM II© interface to calculate brain and distribution rate constants following an administration of the tracer via the peripheral circulation. The distribution rate constants were then input as fixed parameters on the Stella© interface to predict the 3-compartmental distribution of insulin over an extended period.

Deriving predicted values for plasma and brain distribution profiles through a process which generated minimal CV, AIC, BIC and randomly distributed scatter for weighted residuals necessitated the construction of a delay compartment. Number of internal compartments and delay time for the delay compartment were specified individually to optimize goodness-of-fit for each animal. The utility of a delay compartment leads us to speculate that it mimics the neurovascular unit in-vivo, which is a rate-limiting step for transport of tracer in the brain parenchyma. Intriguingly, the predicted AUC at the BBB compartment for every mouse group was in proportion with the predicted brain AUC. An inhibition of insulin availability in the brain correlated with a decreased AUC in the BBB compartment. This positive correlation stems from delay parameters, which were assigned similar values for control and treatment groups. Therefore, the rate of efflux from the

BBB was identical for control and treatment groups, resulting in proportional changes to brain AUC values. To test the accuracy of this observation, BBB microvessels require to be probed in future studies for the accumulation of systemically-administered tracer compounds. The resulting data may be incorporated in a mass distribution model as the one employed in this chapter to correlate values from the delay period with counts in the BBB.

Intravenously-administered ^{125}I-Aβ40 and ^{125}I-Aβ42 displayed higher and lower AUC in the brain in response to insulin administration. This buttresses the implication from graphical multiple-time regression analyses (chapter 2) that Aβ40 is disposed to be retained in the brain for a longer period than Aβ42 due to modulated influx and efflux clearances. These simulations provide a framework or future protocols to examine the effect of various doses of insulin on endogenous amounts of these peptides in an AD brain at several stages, through measurements of the rate of brain-to-plasma trafficking, enzymatic degradation and clearance through other pathways.

In insulin-resistant mice groups (db/db, aged, Aβ40/Aβ42 pre-treated mice), predicted plasma AUC (μCi.min) values were significantly higher than those predicted from control mice administered with 100 μCi of insulin via the peripheral circulation. Further, predicted brain AUC (μCi.min) 45 minutes post-insulin administration via the peripheral circulation is comparatively lesser than that for healthy, control mice. Multi-compartmental analysis showed that APP/PS1 mice showed similar decrease in brain AUC for intravenously-administered insulin, however the effect was only observed until 10 minutes

(appendix). APP/PS1 mice are characterized by peripheral insulin resistance (increased clearance of insulin- Figure 3.2 and Table 3.1), however multi-compartmental simulations do not agree with the other insulin-resistant mouse groups in a time frame beyond 10 minutes. The implications of this discrepancy require to be understood through a replication of the current study in an age-matched group of APP/PS1 mice administered with the same doses of insulin as done in chapter 2.

The hypothesis of experimental studies in chapter 2 was that an AD phenotype leads to decreased brain availability due to a tolerance of peripheral tissues to insulin. Simulations of insulin distribution in Aβ40/Aβ42-treated WT mice confirm this hypothesis and align with simulations from insulin-resistant db/db mice and aged mice. Yet, simulations in this chapter also intriguingly reveal that peripheral tissue AUC of insulin was higher for insulin-resistant groups as compared to age-matched control mice groups. These observations are not in agreement with measurements of ^{125}I-insulin in post-perfused tissues which showed no differences between treatment/transgenic and control groups. Now, interestingly, db/db mice display significantly lesser glucose utilization as compared to control db/- mice. The measured tissue amounts and simulated amounts therefore signify a crucial paradox in that excess availability of insulin in tissues need not translate to a proportional increase in insulin-mediated glucose utilization and other therapeutic functions. This paradoxical finding requires to be tested for significance through measurements of plasma glucose utilization in aged WT and

Aβ40/Aβ42-treated mice as well as through FDG-PET assays in all groups of insulin-treated mice.

CHAPTER 5. Aß40 AND Aß42 IMPAIR INSULIN TRANSPORT PROCESSES ACROSS BLOOD-BRAIN BARRIER ENDOTHELIAL CELLS IN-VITRO

5.1 Synopsis

Having discovered in the previous chapter that the brain availability of insulin in mice displaying an AD phenotype is impaired, the aim in this chapter was to adopt a reductionist approach to investigate the underlying mechanisms. Insulin availability in the brain following a systemic administration is contingent on its transport across the BBB. Therefore, in-vitro BBB endothelial cell models were employed to assess the various sequential processes of insulin transport under conditions mimicking AD. The receptor-mediated binding, uptake, transcytosis and exocytosis of insulin across human cerebrovascular microendothelial cells (hCMEC/D3) were investigated following a pre-exposure to pathological concentrations of Aβ40 and Aβ42.

It was found that the binding of insulin to hCMEC/D3 was not altered by a 1 hour pre-exposure to 3.1 μM of Aβ40 and Aβ42. However, the Vmax and Km of insulin uptake into hCMEC/D3 was significantly inhibited after pre-treatment with 3.1 μM of Aβ40 for 1 hour. The luminal-to-abluminal (L-A) permeability of insulin across polarized hCMEC/D3 monolayers was significantly lowered following exposure to 0.625, 1.56 and 3.1 μM of Aβ40 and Aβ42 on the luminal side. This observation was confirmed by conducting the insulin permeability assay in human brain microendothelial cells derived from induced pluripotent stem cells and pre-exposed to 3.1 μM of Aβ40 and Aβ42 on the luminal, abluminal or both sides of the hCMEC/D3 monolayer. Similarly, the abluminal-to-luminal (A-L) permeability of insulin across hCMEC/D3 was significantly lowered following exposure to 3.1 μM of Aβ40 and Aβ42. The rate of exocytosis of insulin from the luminal end of

hCMEC/D3 was found to significantly enhanced by pre-incubation with 3.1 μM of Aβ40 and Aβ42. This finding aligned with the observation that pre-exposure of the luminal end of hCMEC/D3 to Aβ40 and Aβ42 increased the A-L permeability of insulin. In summary, findings from studies in this chapter prove an inhibition of insulin transcytotic processes by Aβ peptides across the BBB endothelium in-vitro, and are critical to gain an understanding of insulin distribution in AD brains in-vivo.

5.2 Introduction: Findings from the previous two chapters of this thesis revealed a significant inhibitory role of Aß40 and Aß42 in the kinetics of insulin influx and efflux from brains of mice. It was also found that insulin significantly affects the plasma-to brain and brain-to-plasma kinetics of Aß40 and Aß42. These findings provided sufficient experimental evidence to infer that insulin and Aß peptides in the plasma and brain interact with each other resulting in a perturbation of their own kinetics of brain influx and efflux. For the purposes of this thesis, the effects of Aß peptides on insulin transport into the brain will be investigated in further detail. To do, the dynamic mechanisms by which circulating insulin gets trafficked into the brain tissue need to be understood and studied in the context of Aß exposure.

Insulin delivered into the capillaries serves as a recruiter of more capillaries. It also helps increase the blood flow through the capillaries. Capillary availability and subsequent action can be considered as the first step of transcytosis or in other words, a pre-requisite to its appearance in the tissue bed. The second stage of transcytosis occurs at the downstream end of the capillaries where the

microvascular bed is situated (Lee & Klip, 2016). A single layer of endothelial cells lines this bed and it acts as a second layer for the insulin to traverse before it exits the circulation and enters the tissue bed. It is unclear whether limited insulin entry into the tissue bed is due to lack of blood perfusion or a lack of its transit through the microvascular bed. Papers investigating the role of microvascular transit of insulin in-vivo have discovered that the rate-limiting step to insulin resistance in the brain is the microvasculature surrounding the brain. A few other studies have found a crucial role for the factor of tissue perfusion in insulin appearance and subsequent resistance in the brain. Therefore, the evidence from the previous two chapters notwithstanding, there is yet to be a consensus on the rate-limiting factor for transport of insulin into the brain in-vivo. However, in-vitro studies conducted in endothelial cells derived from animals or humans unanimously suggest that the brain resistance of insulin can be associated with a lack of its permeability across endothelial cells. Hence, connecting these pieces of information from literature with findings from chapter I and II of this thesis, it was hypothesized that an inhibition of insulin transport into the brain was caused by Aß peptides at the BBB endothelium.

In this chapter, studies examining effect of Aß peptides on processes of cerebrovascular microendothelial transport of insulin will be studied in a secondary cell line of brain endothelial cells derived from humans, as well as in primary cells derived from human induced pluripotent stem cells (hIPSC).

5.3 Materials and Methods:

5.3.1 Effect of Aß40 and Aß42 on ^{125}I-insulin binding to the hCMEC monolayer**:** The binding of ^{125}I-insulin to hCMEC/D3 monolayer at 4ºC was measured as a function of Aß40, Aß42 and AG1024 (insulin receptor inhibitor) pre-incubation at either 4ºC or 37ºC for 1 hour. Following pre-incubation with inhibitory molecules, media in the luminal compartment was replaced by cold 1% FBS-D3 media containing ^{125}I-insulin and the Transwells were incubated at 4ºC for 1 hour. Thereafter, the cells were washed twice with cold HBSS and lysed with RIPA buffer. Radioactivity counts per minute were measured on the gamma counter.

5.3.2 Effect of Aß40 and Aß42 on ^{125}I-insulin exocytosis through hCMEC monolayers: The steady state efflux of insulin to the luminal or abluminal side of hCMEC/D3 was studied in presence of Aß40 and Aß42. hCMEC/D3 were grown as a monolayer on 12 mm Transwells. On the 7th day, after incubation in D3 media containing 1% FBS, cells were incubated with ^{125}I-insulin for 1 hour on L and A sides. Then the media was replaced by fresh 1% FBS-D3 media containing 3.125 µM of Aß40 and Aß42 on both, L and A sides. Samples (50 µl each) were collected from the L and A compartments at 2, 10, 20, 30, 45 and 60 minute time points.

5.3.3 Effect of Aß40 and Aß42 on insulin endocytosis in hCMEC/ D3 cells***:*** Human cerebrovascular microendothelial cells (hCMEC/D3) were obtained as a gift from Dr. Pierre-Olivier Couraud at Institut Cochin in Paris, France. The cells were seeded as a monolayer (150,000 cells per well) on 6-well plates and cultured in endothelial basal medium (EBM) supplemented with 5% fetal bovine

serum, 1 ng/ml bovine fetal growth factor and 1 nM lithium chloride. The cells were transfected with 1.5 µg/ml of wild-type insulin receptor (IR) DNA one day prior to the experiment. Then the cells were moved to low serum (1%) medium overnight, pre-incubated with Aß40 and Aß42 for 30 minutes, and then treated with various concentrations of fluorescein isothiocyanate (FITC) conjugated-insulin for 30 minutes. Flow cytometry analysis was conducted to compare mean fluorescence in the treatment cells to the control cells. The fold change in fluorescence uptake of FITC-insulin in the presence of Aß proteins was fit to a Michelis-Menten uptake model.

5.3.4 Insulin permeability through hCMEC/ D3 cells in presence of Aß40 or Aß42*:* The hCMEC/D3 monolayers were cultured on 12-mm Transwell™ dishes. On the day of the experiment, following a media change to 1% FBS, the cells were treated with 3.1 µM of Aβ40 and Aβ42 (n=6) on luminal, abluminal, or both sides of the Transwell™ and incubated for 30 minutes at 37°C. Then, 10 µCi of **^{125}**I-Insulin was then added to the donor compartment and the receiver solution was sampled at various intervals for 90 min. The **^{125}**I radioactivity in the samples and in the hCMEC/D3 monoalyers was assayed in a gamma counter. In a parallel assay, to determine the effects of exposure to lower concentrations of Aβ40 and Aβ42 on insulin permeability from the L-A side of the Transwell™, 0.375, 0.75 and 1.5 µM of Aβ40 and Aβ42 were incubated with hCMEC/D3 cells for 1 hour prior to **^{125}**I-Insulin addition to the luminal compartment. The L-A and A-L ^{125}I-Insulin permeability was calculated by normalizing the ^{125}I-Insulin flux

(change in amounts in the receiver compartment with time) by the Transwell surface area and initial concentration in the donor compartment.

$$\frac{Amounts\ in\ receiver\ compartment}{time} = P \times S \times (Conc\ in\ donor\ compartment)$$

Where P is the permeability of insulin in cm/min and S is the surface area (cm^2) of the Transwell surface.

5.3.5 Insulin permeability through human iPSC-derived BMEC in presence of Aß40 and Aß42: Human induced pluripotent cells (iPSC) were cultured and basal micro-endothelial cells were derived from its differentiation by members of Dr. Samira Azarin's laboratory (Lippmann et al, 2012). BMEC were cultured as a monolayer on 12 mm Transwell plates and generously gifted to Dr. Kandimalla's laboratory. Permeability of ^{125}I-insulin through the BMEC monolayer in presence of 3.1 µM of Aß40 and Aß42 was assessed by the method described in the preceding section.

5.4 Results

Switching from an in-vivo examination of emergent characteristics of insulin transport in AD, we constructed a reductionist model in-vitro to test the causative influence of predominantly expressed biomarkers in AD i.e. Aß40 and Aß42 on insulin transport. To that effect, we employed a polarized hCMEC/D3 monolayer to investigate perturbations in sequential processes of insulin transcytosis through the BBB endothelium in presence of Aß40 and Aß42. Since the APP/PS1 transgenic mouse model expresses Aß40 and Aß42 in significantly higher amounts as compared to WT mice, we designed our in-vitro experiments

with higher amounts of Aß40 and Aß42, albeit within physiologically toxic concentrations.

First, we examined the effects of Aß40 and Aß42 on binding of insulin at 4 ºC to an hCMEC/D3 monolayer. Interestingly, we did not see differences in hCMEC binding between ^{125}I-insulin controls and Aß40 or Aß42-pretreated samples. This result prompted us to monitor differences between treatments in the next theoretical step in insulin transport i.e. its receptor-mediated endocytotic uptake. We measured uptake of FITC-insulin into hCMEC/D3 transfected with either model wild-type human IR (hIR) or mutant hIR, subsequent to incubation at either 37 ºC or 4 ºC. It was observed that FITC-insulin uptake into cells transfected with hIR at 37 ºC was higher than that in cells transfected with mutant IR at 37 ºC or 4 ºC (fig. 5.1). This, along with the observation that uptake of FITC-insulin into hCMEC/D3 is linear until 45 minutes of incubation (data not shown), proved that insulin uptake is energy and temperature-dependent and the process of receptor-mediated endocytosis is not saturated within the treatment timeframe. Thus, using this evidence, we examined the effects of 6.2 µM Aß40 and Aß42 on insulin uptake at 37 ºC in hCMEC transfected with hIR. We observed that in presence of Aß40, the V_{max} (maximum steady-state rate of uptake) and K_m (substrate concentration at which the rate of uptake is half the maximum rate of uptake) of saturable FITC-insulin uptake in hCMEC was found to be significantly decreased when fit to a Michelis-Menten kinetic model on Graph Pad Prism 6 Inc. (Table. 5). The uptake of FITC-insulin into BBB endothelium at higher concentrations of FITC-insulin was significantly decreased in presence of Aß42.

However, the effect of Aß42 could not be modeled by a Michelis-Menten nonlinear equation owing to high variability in the estimates for V_{max} and K_m.

The Vmax and Km of insulin uptake decrease simultaneously in presence of Aß40. This is suggestive of uncompetitive inhibition of insulin uptake by the insulin receptor since uncompetitive inhibition occurs when a molecule does not inhibit the Vmax and Km of the substrate uptake by binding to the receptor; rather, the inhibitor molecule binds to the substrate-receptor complex downstream of the receptor. The reason for high variability in fitting a nonlinear regression model to FITC-insulin uptake following Aβ42 incubation could be due to an unsteady structure of the Aß42 peptide, which is given to assume beta-sheet forms. Therefore, the interactions of Aß42 with IR at the given dose and incubation period, and its effects on the affinity and capacity of IR for insulin could vary drastically depending on its adopted structure.

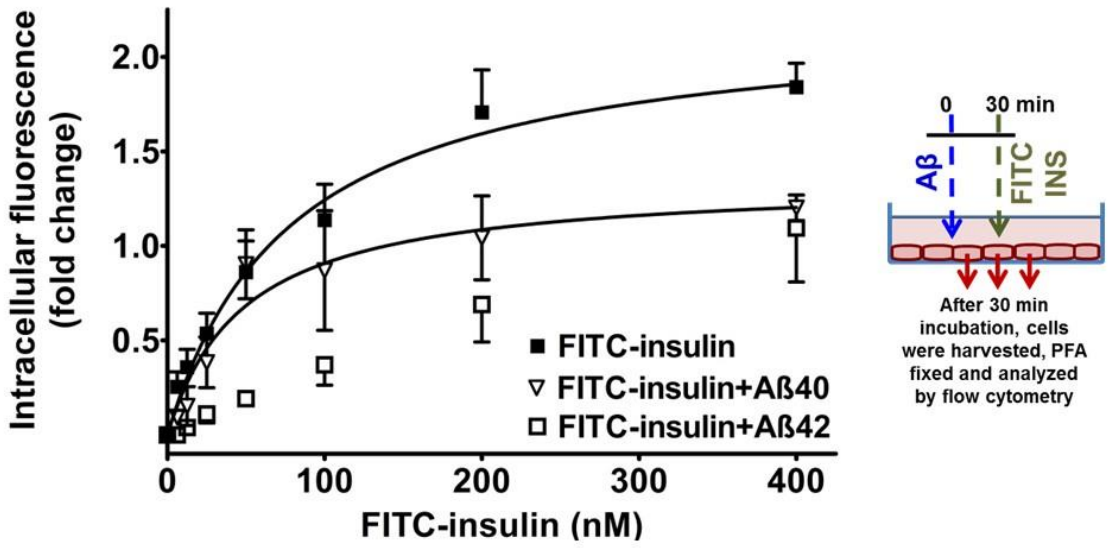

Figure 5.1: Uptake of FITC-insulin into hCMEC/D3 with or without pre-treatment with Aβ40 and Aβ42, as measured by Flow Cytometry. Median fluorescence

intensity of FITC-insulin uptake in hCMEC/D3 monolayers overexpressed with either Wild-Type IR or mutant IR at 37 ^{o}C or 4 ^{o}C. Fig. B. Following pre-incubation with or without Aβ proteins (6.2 μM) for 30 min at 37 ^{o}C, the IR-hCMEC/D3 monolayers were incubated with various concentrations of FITC-insulin for 30 min. The cells were removed from the substrate by gentle trypsinization and then the intracellular fluorescence was assessed by flow-cytometry. Fluorescence intensity fold-change compared to the untreated control was plotted against FITC-insulin concentrations. Data concerning FITC-insulin uptake in presence of Aß40 (inverted triangles) fit to a Michelis-Menten uptake model and the parameter estimates are specified in a table in Fig. B (ii). FITC-insulin uptake in presence of Aβ42 (open squares) did not fit to a Michelis-Menten uptake model.

Estimates	FITC-insulin	FITC-insulin +Aβ40	p-value
Vmax	2.22 ± 0.21	1.35 ± 0.17	0.004 (**)
Km (nM)	78.59 ± 19.78	48.62 ± 19.69	0.03 (*)

Table 5: The estimates of Vmax and Km from Michelis Menten curve-fitting of data regarding the effect of Aβ40 on FITC-insulin uptake in hCMEC/D3 cells.

Having discovered a different mechanism of insulin uptake into the BBB endothelium because of Aß peptide exposure, the aim was to examine whether the modulated uptake mechanism led to differences in permeability of insulin across the BBB endothelium. Therefore, hCMEC/D3 cells were cultured on Transwell® inserts such that it resulted in polarization into luminal and abluminal ends. ^{125}I-Insulin was selected as the tracer molecule for the permeability assay. After spiking 10 μCi of ^{125}I-insulin onto the luminal end of the hCMEC/D3 monolayer or the donor compartment, the fluxes through the abluminal end or into the receiver compartment of the Transwell® were measured over 6 intervals in a period of 120 minutes. Calculated mean L-A permeability for ^{125}I-insulin was

1.2 X 10^{-4} cm/min, whereas that following a pre-incubation with 3.1 Aβ40 or Aβ42 on the L, A, or both L and A sides for 30 mins, were significantly lower, as shown in Figure 5.2. Similarly, on conducting an A-L permeability assay, the mean permeability of 125I-insulin from the A-L side was found to be significantly reduced when Aβ40 or Aβ42 were incubated on the A or L&A sides. Intriguingly, we also observed that incubation with 3.1 μM of Aβ40 or Aβ42 on the luminal side significantly increased the A-L permeability of ^{125}I-insulin through the hCMEC/D3 monolayer.

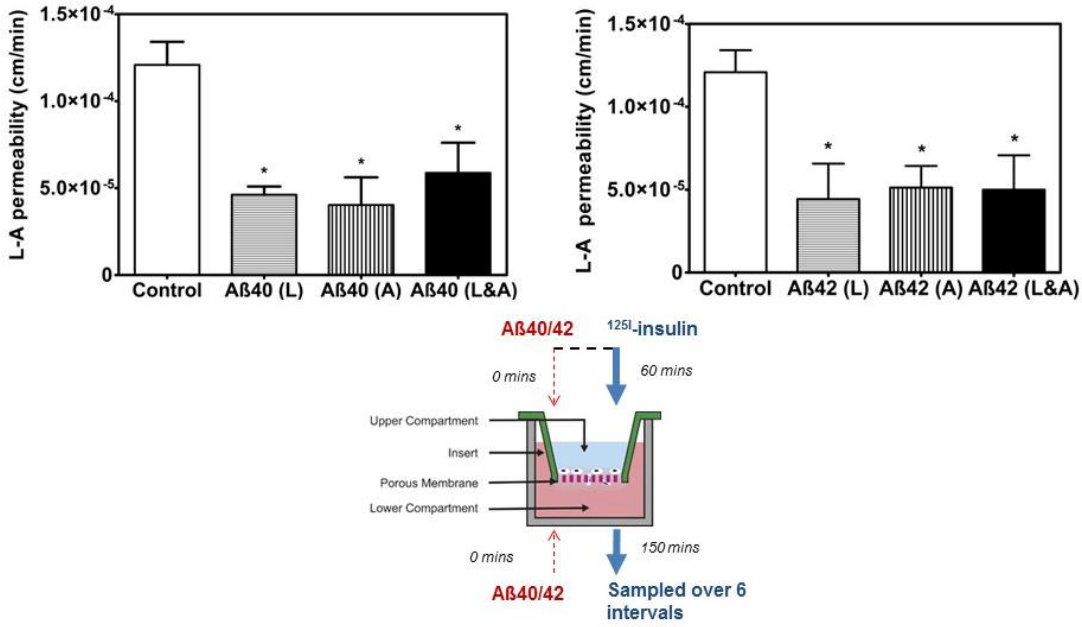

Figure 5.2 ^{125}I-insulin permeability across hCMEC/D3 monolayers was determined in the luminal-to-abluminal (L-A) with or without (control) Aß peptide exposure. The monolayers were pre-incubated for 30 min with either Aß40 or Aß42 on the luminal side (L), the abluminal side (A), or on both sides (L&A). Figures on the left and right depict the L-A ^{125}I-insulin permeability after incubation with Aß40 or Aß42 pre-incubation, respectively, on the L, A or on the L&A sides.

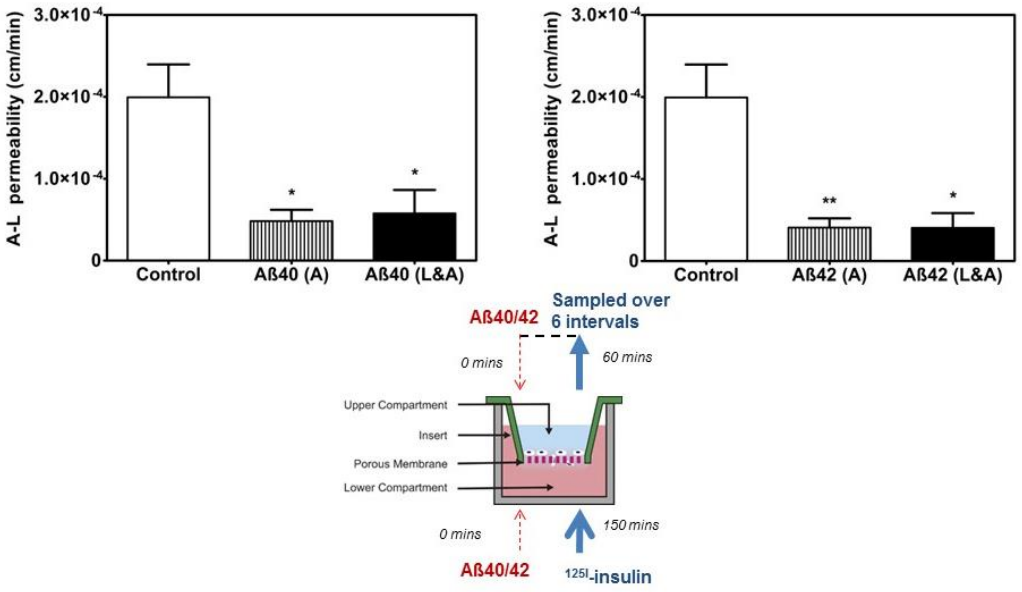

Figure 5.3 ^{125}I-insulin permeability across hCMEC/D3 monolayers was determined in abluminal-to-luminal (A-L) directions with or without (control) Aß peptide exposure. The monolayers were pre-incubated for 30 min with either Aß40 or Aß42 on the luminal side (L), the abluminal side (A), or on both sides (L&A). Fig. C (i) and C (ii) depict depict the A-L ^{125}I-insulin permeability.

Next, the effects of lower concentrations (0.3, 0.9 and 1.56 μM) of Aß40 and Aß42 on the L-A permeability of ^{125}I-insulin across hCMEC/D3 was assessed.

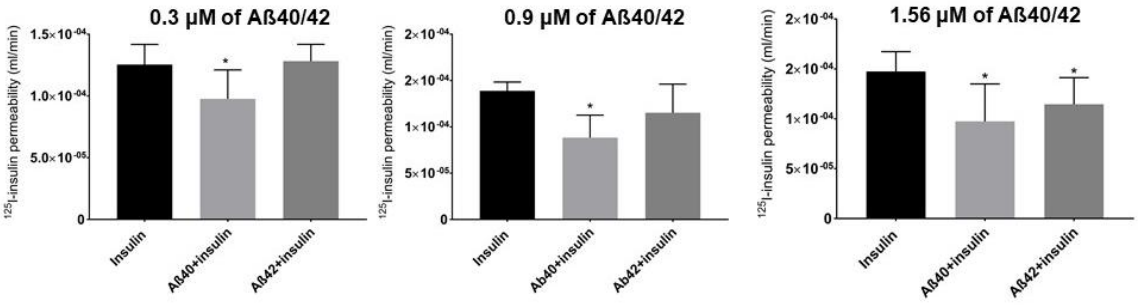

Figure 5.4. ^{125}I-insulin permeability from the L-A side of hCMEC/D3 following pre-treatment with 0.3, 0.9 and 1.56 μM of Aß40 and Aß42 for 1 hour.

Interestingly, Aß40 significantly reduced the L-A permeability of ^{125}I-insulin at 0.3, 0.9 and 1.56 μM. Aβ42 significantly reduced the L-A permeability of ^{125}I-insulin at 1.56 μM.

A secondary cell line of hCMEC/D3 exhibits a TEER value which is 25-30-fold lower than the TEER value of the BBB in-vivo. Thus, our permeability assays were confounded by the limited integrity of the cell monolayer. To assess the effects of Aβ40 and Aβ42 on insulin permeability across the BBB endothelium characterized by physiologically equivalent TEER values, BMEC derived from iPSC was employed as the cell line. Permeability assays with ^{125}I-insulin were conducted in BMEC in the presence of 3.1 μM of Aβ40 and Aβ42. It was discovered that the L-A permeability of 125I-insulin through BMEC was 9-fold than that through hCMEC/D3. However, pre-treatment with Aβ40 and Aβ42 for 1 hour significantly decreased the L-A permeability of 125I-insulin across BMEC (Figure 5.7).

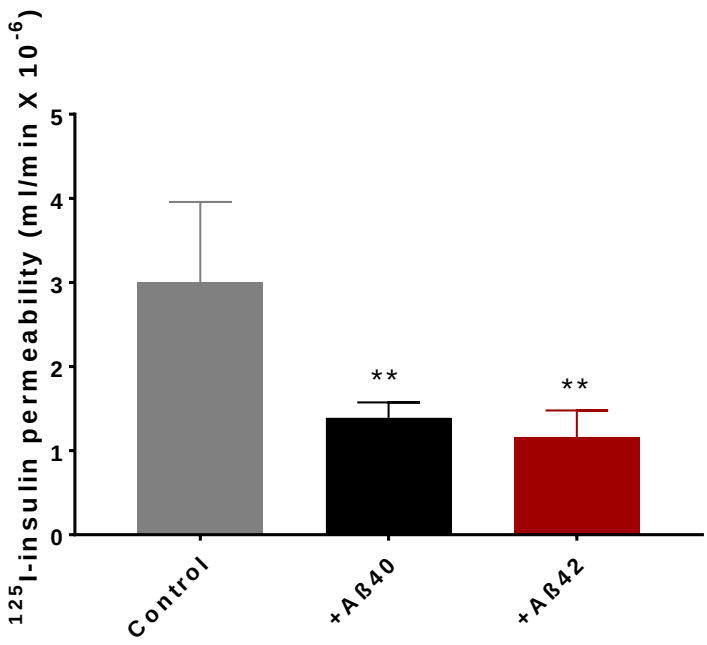

Figure 5.7. ^{125}I-insulin permeability from the L-A side of human BMEC derived from iPSC following pre-treatment with 12.5 µg of Aß40 and Aß42 for 1 hour.

When the capacity of ^{125}I-insulin to exocytose through the luminal end of hCMEC/D3 was assessed, it was found that Aβ40 and Aβ42 significantly increased the luminal exocytosis of ^{125}I-insulin (Figure 5.8)

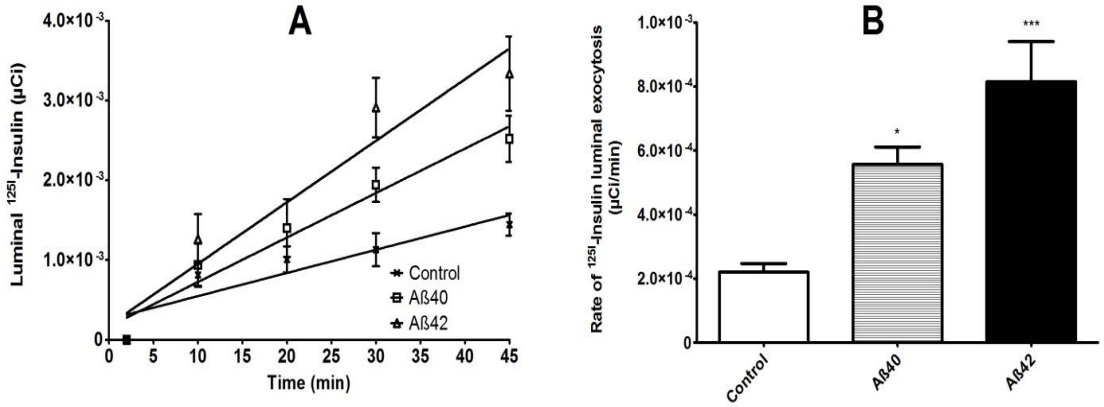

Figure. 5.8 Effect of Aß40 and Aß42 on luminal exocytosis of ^{125}I-insulin from an hCMEC monolayer**.** In (A), luminal amounts of ^{125}I-insulin (µCi) in hCMEC/D3

monolayers treated with either Aß40 or Aß42 (3.12 μM for 1 hour) on both, luminal and abluminal sides, is plotted. In (B), rate of ^{125}I-insulin exocytosis (μCi/min) to the luminal side in presence of Aß40 or Aß42 peptide isoforms, calculated from slopes in plot A, is depicted.

5.5 Discussion

Current understanding of insulin resistance in an AD brain has evolved from studies proving that signaling mechanisms downstream of the insulin receptor are impaired in presence of Aß peptides. These studies have however been conducted in post-mortem AD brains or neuronal models. Now, insulin in the systemic circulation can enter the brain only via an IR-mediated transcytotic pathway in the microvasculature of the brain. Previously conducted research has neither measured insulin transport through cerebrovascular microendothelial cells nor has it assessed impact of Aß peptides on variations in its transport into the brain. Blood-brain barrier microvascular endothelial cells are phenotypically different from endothelial cells in the periphery, in that, they lack intracellular cleft junctions and fenestrae and express tight junctions with significantly higher transendothelial resistance. While mechanistic aspects of insulin uptake and transcytosis through large or small peripheral endothelial cells have been understood (Azizi et al., 2015), (Wang et al, 2011), they have not been studied at the level of the BBB microvasculature, considered a rate-limiting barrier to insulin transcytosis into the brain parenchyma. Particularly in dynamic neurodegenerative disease states such as LOAD, which is characterized by drastically low levels of insulin in the brain and impaired Aß peptide clearance from the BBB, examination of kinetic and dynamic interactions of insulin with the BBB endothelium has largely been neglected. This chapter report leads us to speculate that brain uptake of insulin is significantly lower in double transgenic

(APP/PS1) AD model mice due to an inability of BBB endothelial cells, incubated with Aß peptide isoforms (Aß40 and Aß42), to endocytose and transport insulin into the brain parenchyma. Through our in-*vitro* and in-*vivo* study models, we attempted to mimic the pathophysiology of Aß-mediated insulin resistance by employing supra-physiological concentrations of insulin or Aß isoforms, whilst limiting other confounding factors such as endogenous presence of insulin and induced hypoglycemia.

Our hypothesis that amyloid peptides inhibit insulin transcytosis across the brain microvascular endothelium was predicated on the assumption that insulin binds to IR on the luminal surface of the cerebrovascular endothelium. The bound insulin forms a complex with the IR. The IR-complex then releases insulin into the intracellular space where it escapes lysosomal degradation to shuttle through to the abluminal surface. The IR is finally degraded or recycled back to the plasma membrane.

In this chapter, sequential processes of insulin transport across the BBB endothelium were examined under conditions mimicking the early stage of AD. Findings from the studies described in this chapter provide novel insight into molecular details underlying the observation of lowered insulin in brains of AD patients. These molecular details were delineated by conducting experiments with monomeric forms of Aβ40 and Aβ42 and FITC or ^{125}Iodine-labeled insulin in BBB endothelial cells in-vitro. First, it was established that insulin uptake into BBB endothelium is receptor-mediated by showing that over-expression with mutant IR did not enable the uptake of FITC-insulin into hCMEC/D3 monolayers

(Figure A13; Appendix). It was then shown that 3.1 μM of Aβ40 significantly perturbed the kinetics of Michelis-menten uptake of FITC-insulin across hCMEC/D3. In fact, the Vmax and Km of FITC-insulin were both significantly lowered, indicative of an uncompetitive inhibition of FITC-insulin uptake by Aβ40. This is the first proof in literature, of an alternate mechanism of insulin uptake into cells, in AD conditions.

Next, permeability of insulin across polarized BBB endothelial monolayers were examined as a function of increasing concentrations of Aβ40 and Aβ42. Expectedly, inhibitory effects of Aβ40 and Aβ42 were more pronounced with increasing concentrations, as evidenced by an increased extent of permeability inhibition with 3.1μM as compared to 0.3, 0.9 or 1.56 μM of Aβ40 and Aβ42. hCMEC/D3 exhibit lower TEER values as compared to BMEC derived from iPSC. This difference in monolayer integrity, however, did not affect the capacity of Aβ40 and Aβ42 to inhibit the permeability of insulin, as proven by a significant decrease in permeability of ^{125}I-insulin across BMEC in presence of Aβ40 and Aβ42. This result is promising in that it serves as a segue into further studies concerning effects of Aβ40 and Aβ42 on insulin trafficking and signaling in BMEC, which closely resembles the BBB in-vivo. Lastly, it was observed that the exocytosis of insulin across the luminal end of the hCMEC/D3 monolayer was enhanced by the Aβ peptides. This result corroborates the finding that the permeability of 125-insulin from the A-L end was increased when Aβ peptides were pre-incubated on the luminal side. The physiological implication of these observations are that insulin could be disposed to exit the BBB endothelial cells

and re-enter the plasma in presence of excessive amounts of circulating Aβ peptides.

CHAPTER 6. Aβ40 AND Aβ42 MODULATE THE DYNAMICS OF THE INSULIN RECEPTOR AT THE BLOOD-BRAIN BARRIER IN-VITRO

6.1. Synopsis

The previous chapter delineated the inhibition of IR-mediated uptake, permeability and exocytosis of insulin from hCMEC/D3 cells exposed to pathological concentrations of Aβ40 and Aβ42. It also described the inhibitory effects of increasing concentrations of Aβ40 and Aβ42 on insulin permeability across hCMEC/D3 as well as a iPSC-derived BMEC cell line. The plasma membrane fraction of IR in hCMEC/D3 undergoes lateral diffusion and gets endocytosed into the cytosol upon insulin exposure; the cytosolic fraction of IR is exocytosed to the plasma membrane surface and internalized thereafter, in response to insulin. IR also initiates signal transduction via either, the PI3K or MAPK pathways in response to insulin exposure.

In this chapter, the kinetics of IR, lateral diffusion, endocytosis, exocytic recycling were assessed and the phosphorylation of key events in the MAPK and PI3K pathway were mapped as a consequence of Aβ40 or Aβ42 exposure to hCMEC/D3 cells. Spinning-disc confocal microscopic images revealed that Aβ40 and Aβ42 delayed the insulin-mediated IR endocytosis. A FRAP/FLIP imaging protocol helped discover that the half-lives of IR of a combination of lateral diffusion and exocytic recycling or only exocytic recycling were increased as a result of Aβ40 and Aβ42 exposure to hCMEC/D3 cells. This signifies that the trafficking of IR is perturbed in response to Aβ peptide treatment of cererbrovascular endothelial cells. Western blot revealed that insulin-mediated phosphorylation of AKT (ser473) was significantly decreased whereas the phosphorylation of IR-β (Tyr 1162/1163) was increased due to Aβ40 and Aβ42.

Moreover, Reverse Phase Protein Array (RPPA) analysis revealed that MAPK1 was increased, whereas caveolin-1 expression was decreased following Aβ40 and Aβ42 treatment.

6.2 Background:

6.2.1 Endocytosis and signaling: The primary process by which extracellular ligands are internalized into the interior of the cell is endocytosis. (Birtwistle & Kholodenko, 2009) succinctly explained a two-step process of endocytosis wherein, following the attachment of the ligand to the plasma membrane, an invagination is created in the plasma membrane. A vesicle containing the extracellular ligand pinches off through this invagination leaving the membrane surface intact. Through a network of organelles such as early, middle and late endosomes, the ligand accesses the interiors of the cell to initiate changes to regulatory functions of the cell. The authors also asserted that endocytosis is a mechanism by which signal can be distributed to the intracellular regions that are not accessible through a slow diffusion process characterized by signal attrition. They delineate with assistance by way of literature evidence and mathematical models, that for signaling pathway activation initiated by certain receptor tyrosine kinases such as EGFR and VEGF, endocytosis is a critical step. It is important not only to distribute signal to endosomal structures but also to distant regions such as the nucleus, to avoid the loss due to diffusion. This has been evidenced in case of nerve growth factor, which requires endocytosis for long distance (10-100μm) transfer of signal from the distant axons to the soma. The transfer of

signal is mediated by molecular motor driven trafficking in the endosomal structures (Irannejad, Tsvetanova, Lobingier, & von Zastrow, 2015).

In the review (Birtwistle & Kholodenko, 2009), it is emphasized that the relation between endocytosis and signaling is bi-directional in that signaling is equally an important pre-requisite to endocytosis. The authors prove this assertion by citing the example of EGF-mediated activation of EGFR, after which occurs a propagation of signal through the endosomes, limited only by phosphorylation dependent recruitment of substrates downstream of the pathway.

6.2.2 Regulation of endocytosis of receptor tyrosine kinases (RTK): RTK are known to internalize constitutively and recycle back to the plasma membrane. The pathways assumed by the internalized receptors within the cell interior influence signaling mechanisms and vice versa. Several ligand-associated factors such as ligand concentration, exogenous stress, stimuli, cell adhesion etc. affect the internalization of receptors (Goh & Sorkin, 2013). With respect to ligand concentration, (Goh & Sorkin, 2013) review an example of EGFR activation, wherein low concentrations of epidermal growth-factor results in a clathrin-mediated endocytosis of EGFR, whereas high concentrations lead to a clathrin-independent endocytosis. This, in turn, affects the recycling rates of EGFR and its accumulation on the plasma membrane needed for a continuation of the cycle of ligand-mediated activation. In the upcoming sections, the detailed mechanisms of endocytosis and signaling pertaining to the insulin receptor will be reviewed. The importance of the dynamics of the insulin receptor in context of AD will also be discussed.

6.2.3 Endocytosis of insulin receptor (IR): Insulin binds to the receptor beta subunit situated on the plasma membrane. IR is a heterotetrameric transmembrane RTK which is synthesized in the endoplasmic reticulum (ER). It is structured to contain two extracellular α subunits and two transmembrane β-subunits which are connected by disulphide bonds. Following synthesis in the ER, it diffuses to the Golgi apparatus and is transported to the plasma membrane. The IR accumulates on the surface in response to insulin stimulation and consequently diffuses into the interior. Upon internalization, the insulin-receptor complex is sequestered in clathrin-coated pits or caveolae (dependent upon the cell type). Following its formation, the receptor complex is shuttled to a family of endosomes, wherein the receptor complex is posited to break up to separate insulin and receptor; and IR are recycled to the membrane or transported to the lysosomes to undergo degradation. Similar to other RTK, the residence time of IR on the surface can be estimated based on the nature of the cells, its rates of internalization, degradation and recycling. The turnover time for RTK can be as high as 20hr, based on a paper by (Stoscheck & Carpenter, 1984) and reviewed by (Goh & Sorkin, 2013). (Marshall, 1985) conducted kinetic experiments in adipocytes and observed that insulin mediated an accumulation of receptors within the cell in 30 seconds and a half-life of 2.7 mins. The author concluded that there was no net loss of receptors owing to a recycling capacity of the receptor within a time frame of 6 minutes. Another important conclusion derived from experiments with receptor recycling inhibitors such as chloroquine

was that in absence of recycling, receptors were directed to a degradative pathway, thereby resulting in a degradative receptor loss.

Considering that RTK are characterized by a strong correlation between endocytic activities and signaling frameworks, it is important to investigate the regulation of IR endocytosis under various ligand-associated factors such as stress factors and high concentration. No studies concerning the effect of insulin receptor internalization on its signaling and vice versa have heretofore been conducted.

Aß peptides interact with insulin receptors by inhibiting the intracellular propagation of signal at several junctions in the PI3K pathway, as evidenced from immunohistochemical analyses of post-mortem brains of patients at advanced stages of AD. They have also shown to compete with insulin for binding to the insulin receptor in neurons. Mechanisms by which they regulate the dynamics of insulin receptor endocytosis are not clearly understood. Since endocytosis of IR regulates the distribution of activated signal to the nucleus, which in turn is required to process regulatory function, it is important to ascertain the temporal and spatial distribution of IR in response to Aß peptides.

Numerous studies have unequivocally proven that the protein caveolin-1 residing within the caveoloe is essential to the actions of insulin within vascular cells. Lipid environment in membranes is divided into unsaturated phospholipid regions and microdomains flush in cholesterol and saturated phospholipids (Cordy, Hooper, & Turner, 2006). These ordered microdomains, known as lipid rafts, contain enzymes responsible for post-processing of the amyloid-precursor protein. This

has resulted in conflicting findings regarding the role of lipid raft containing cholesterol in the progression of Alzheimer's disease. Unpublished results from Dr. Kandimalla's lab suggest that internalization of Aβ42 peptides into in-vitro human brain microvascular endothelial cells is dependent on the stability of lipid rafts. Separately, literature is abounding with evidence regarding the influence of lipid raft caveolae (Morino-Koga et al., 2013; Sanchez-Wandelmer et al., 2009) in the activation of the insulin receptor. Disruption of caveolae in lipid rafts has been shown to suppress insulin receptor-mediated signaling in peripheral cells. Evidence in this chapter suggests that ablation of cholesterol in lipid rafts through specific chelating agents significantly inhibits insulin uptake into in-vitro human brain microvascular endothelial cells. These results are indicative of an influence of Aβ peptide isoforms on the dynamics of insulin receptor signaling at the BBB through a lipid-raft mediated membrane disruption. Lipid-rich caveolae domains are therefore crucial in stabilizing the insulin receptors on the plasma membrane and in communicating cargo as well as signal from the plasma membrane to the interiors of the cell.

6.2.4 Signal transduction by insulin receptor tyrosine kinases: Activated signal from the insulin receptor is required to diffuse through the interiors of the cell to initiate phenotypic changes associated with insulin action. As described earlier, signaling occurs in conjunction with endocytosis for several GPCR receptor subtypes. However, it is still unclear whether insulin receptor signaling is indeed a pre-requisite for the endocytic actions of insulin. IR-β subunit is autophosphorylated at three tyrosine residues (Tyr-1158, Tyr-1162 and Tyr-

1163) following a conformational change in the intracellular portion of one of the β subunits which is induced by insulin molecules bound to IR on the plasma membrane of a cell. Thereafter, signal transduction from the tyrosine kinase occurs through molecular effectors either in the phosphatidyl inositol-3 (PI3K) pathway or the mitogen activated kinase (MAPK) pathway. This differential routing of signal transduction is experimentally proven to be strongly associated with the nature of activation of docking proteins such as the IR substrate protein, which binds to the activated IR-β subunit. Insulin receptor substrate (IRS-1) proteins (1,2,3,4) is recruited to the surface as a response to IR-β conformational change and activation. IRS-1 is phosphorylated at the threonine residues, leading to further activation of signaling intermediates downstream in the PI3K pathway. Transduction of signal through the PI3K pathway leads to metabolic and ant-apoptotic effects induced by the bound insulin. When phosphorylated at the serine residues, IRS-1 recruits effectors in the MAPK pathway, activation of which is understood to be correlated with mitogenic and apoptotic effects. These effects are important in the context of AD as the BBB vasculature is vulnerable to atypical and/or aberrant signaling in presence of Aß peptides. Experimental methods probing this phenomenon of Aβ peptide-induced cross talk will be described in this chapter and questions arising from the results will be addressed and discussed.

6.2.5 Modulation of insulin receptor dynamics: There are at least three mechanisms by which the trafficking of insulin receptors can be modulated:

a. Perturbation of internalization of the receptor

b. Modulation of the recycling and degradation dynamics of the receptor

c. Modification of the signaling capacity of receptors within endosomes.

Perturbation of IR receptor dynamics can result in the following changes in cell activity:

a. Change in short-term and short-range intracellular signaling

b. Modification of the transcriptional response through a modulation of events in one or more of numerous signal transduction pathways (Brankatschk et al., 2012).

c. Perturbation of the transcytosis of peptides in specific cell types. E.g. insulin, transferrin and Aß peptides at the vasculature.

6.2.6 IR dynamics in AD: Expression, function and signaling dynamics of IR have been examined in brains of AD patients, mouse models and cell-cultures. Up-regulation or down-regulation of IR or certain key intermediary signaling molecules in the PI3K or MAPK pathways mediated by IR, seem to conflict based on a review of results from these studies (Stanley et al, 2016). For example, (Steen et al., 2005) depicted that mRNA levels of IR in AD patients undergoes a reduction with a progressive escalation of BRAAK stage, whilst (Hoyer, Lee, Loffler, & Schliebs, 2000) documented that patients greater than 65 years of age express higher levels of IR protein than age-matched normal patients. More recent studies such as those by (Talbot et al., 2012) have shown no differences in brain IR expression between AD and normal patients.

Discrepancies in IR activation in post-mortem AD brains likely arise because the stage of AD occurrence in subjects differs between studies and disposition of the Aß peptides residing in post-mortem brain samples between studies is highly variable. Assays which are conducted to ascertain the extent of mRNA expression cannot be correlated to the amount of protein expression. Moreover, significant amount of post-processing of samples is involved i.e. the activation of IR pathways are not examined in real-time. These caveats notwithstanding, IR-mediated signal transduction is inherently variable owing to differences in expression in brain regions.

No publications have yet documented the impact of early-stage AD conditions on dynamics of IR at the vasculature, given that IR at the BBB vasculature is responsible for shuttling the insulin cargo from the periphery into the brain parenchyma. It is difficult to non-invasively generate real-time information about receptor dynamics at the BBB. Nonetheless, it can be achieved through a deconvolution of data generated by conjugating a PET or SPECT probe to peripherally administered ligand of interest and targeting it toward ROI in brains of willing subjects.

6.3 Examination of intracellular IR distribution: A typical method of determining the extent of receptor distribution in different regions of the cell is by subcellular fractionation. This provides evidence for protein accumulation within organelles such as the plasma membrane, early, middle and late endosomes, and the nucleus. Antibodies against the receptor are applied to semi-quantitatively assess the receptor distribution by Western Blots. Tracking co-

localization of receptors within clathrin-coated pits or caveoloe, or within the early, middle or late endosomes with help of specific antibodies against proteins of interest serves to confirm intracellular areas within which the receptors are distributed. Radioactively labeling receptors and measuring their distribution in cell organelles proves to be another method of quantitation. It must be noted that receptor endocytosis and recycling phenomena occur within a matter of seconds and the methods described above do not retain all the information related to subcellular dynamics since they are time-consuming and destructive toward cells. Confocal imaging serves as a non-invasive procedure to precisely target receptor movement. Fluorescently-tagged receptors can act as surrogates to the movement of unlabeled receptors. They are amenable to spatial perturbation via exposure to lasers at various wavelengths and intensities. Measuring the mobility of the perturbed receptors yields information which approximates their physiological response capacity and kinetics within the cell. In this chapter, kinetics of the insulin receptor at the BBB were measured from tracking the recovery of fluorescently-tagged receptors after photobleaching. Results from this study will be discussed in context of conditions mirroring the physiological state in early-stage AD.

6.4 Examination of IR signaling: Signal transduction induced by IR at the plasma membrane and at several intracellular junctions in different pathways is studied in cells treated with a desired concentration of effector ligands. Activation of time-dependent intracellular events is typically studied through the application of receptor-specific antibodies to cell or tissue lysates subjected to Western

Blots. Western blots are applied to assess the disposition of a few proteins at once, however, to study the activation of several proteins at once, an antibody array is a recent technique which has emerged into focus. The standard protocol to study protein expression and activation by means of an array is to affix the requisite primary antibodies onto a custom membrane surface and expose them to analytes of interest. It is then conjugated with the secondary antibodies and a signal is attained and visualized by means of a colorimetric reaction.

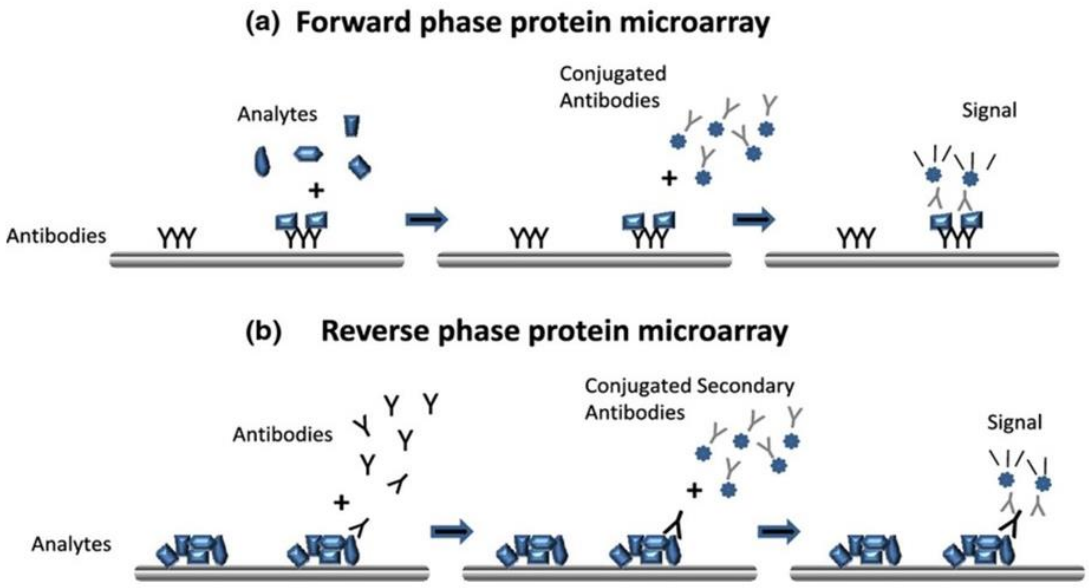

Figure 6.1. Schematic of differences between forward and reverse phase protein microarray (RPPA).

A modification of this protocol is one wherein the analytes of interest are affixed to a surface and respective antibodies are added to it at a desired concentration and time. With this modification, it is possible to tag an analyte with multiple antibodies at once; signal is attained, amplified and probed by means of a colorimetric reaction. This technique is commonly known as reverse-phase

protein array (RPPA). In this chapter, RPPA will be a technique applied to study IR induced signal transduction as applicable to BBB in AD.

Specific aims of this chapter:

1. To image the impact of Aß peptides on the internalization of the insulin receptor
2. To evaluate IR activation through Western Blots of treated hCMEC/D3 cell lysates
3. To assess effect of Aß peptides on exocytic recycling and lateral diffusion of IR-GFP through FRAP assays in Nikon Super-resolution microscope
4. To measure the effect of Aß peptides on signal transduction in PI3K and MAPK pathways by RPPA

6.5 Materials and methods:

6.5.1 Effect of Aß peptides on the intracellular trafficking of IR: Having established that Aß peptides impair the uptake capacity of IR for insulin (chapter 4), we wanted to examine the effect of Aß peptides on the intracellular trafficking of IR. To that effect, we conducted a preliminary assay to qualitatively image the time-dependent expression of IR on the surface. hCMEC/D3 cells plated as monolayers (35,000 cells per dish) on 35mm cover-slip glass bottomed dishes, were transfected with 1.5 µg/ml of IR-GFP three days after initiation of culture. Transfection of hCMEC with IR-GFP DNA was conducted with help of a Lipofectamine LTX transfection reagent. Following 12 hours of exposure to the DNA construct, the endothelial basal media was replaced with that containing

fresh 5% Fetal Bovine Serum. Cells were serum starved 4 hours prior to experiment. The expression of IR-GFP on the plasma membrane of live hCMEC/D3 cells as a function of insulin and/or Aß peptides treatment was examined by spinning disc confocal microscopy. 25 µg/ml of Aß40 and Aß42 and 250nM of insulin were the concentrations employed for the experiment. Cells were exposed to Aß peptides 1 hour prior to treatment with insulin.). A laser power of not more than 20% and a 100X oil immersion objective was used. The excitation and emission of GFP was set at 488 nm and 510 nm filter sets respectively.

Each dish was placed separately inside the microscope incubation chamber at 37 ºC and 5% CO_2. Cells displaying surface expression of IR-GFP were chosen for further imaging after treatment. 250 nM of Novolin (100 mU/ml) was added to the cells and the surface IR-GFP expression in a single control cell was imaged until 20 minutes. Similarly, single cells were imaged for expression of IR-GFP before or after treatment of Aß40 or Aß42, followed by treatment with insulin. The images were processed with identical magnitude of change in brightness and contrast.

6.5.2 Effect of Aß peptides on insulin-mediated signal transduction in the PI3K pathway: hCMEC/D3 cells were seeded as a monolayer (150,000 cells per well) onto 6-well plates and cultured in Endothelial Basal Medium supplemented with 5% fetal bovine serum, 1 ng/ml bovine fetal growth factor and 1nM lithium chloride. The cells were transfected with 1.5 µg/ml insulin receptor DNA 36 hours prior to the experiment. On the 7^{th} day, serum-starved confluent cell monolayers

were treated with 25 µg/ml of Aß40 or Aß42 and incubated for 30 minutes. Insulin was then added to the cells at a concentration of 100nM and cells were incubated for 20 minutes at 37°C. Cells were harvested in Hanks' Balanced Salt Solution containing protease inhibitor and phosphatase inhibitor cocktail (1:100). The harvested cells were lysed in 50 µl RIPA (Sigma-Aldrich, St Louis, MO) buffer and the protein content within the sampled cells was analyzed by a BCA assay. Samples were loaded onto 4-15% pre-cast, tris-glycine SDS-PAGE gels and electrophoresed initially for 100V for 15 minutes and then 150 V for 45 minutes. The gel was transferred onto a 0.2 µm nitrocellulose membrane (Bio-Rad, Hercules, CA) through a transfer process at 100 V for 1 hour. After blocking for 1 hour, the blot was incubated overnight with 1:200 and 1:100 dilutions of of Akt and p-Akt (Ser-473) (Santa Cruz Biotechnology, Inc) polyclonal IgG respectively. After rinsing the blot with Tris-buffered saline, it was incubated with a 1:2000 dilution of a HRP- conjugated secondary antibody toward Akt and p-Akt for 1 hour and then developed with SuperSignal Enhanced Chemiluminescent substrate (Thermo Scientific, Rockford IL). The levels of Akt and phosphorylated Akt (p-Akt) protein kinases were analyzed by densitometry on the Western Blot. Similarly, the insulin-mediated phosphorylation of the insulin receptor ß subunit (p-IR) was examined in presence of Aß40 and Aß42 in IR overexpressed cells. Densitometric analysis was conducted to normalize the p-IR values to the basal levels of IR.

6.5.3 Effect of Aß peptides on insulin-mediated mobility of IR on hCMEC/D3 plasma membrane

Human cerebrovascular microendothelial cells (hCMEC/D3) were seeded as a monolayer on 35mm coverslip bottomed-dishes. In order to study diffusion of the GFP-tagged insulin receptor, monolayers were transfected with 0.7 µg IR-GFP DNA per dish. On the 5^{th} day, monolayers were washed and observed at 60 X magnification under a Nikon A1Rsi Confocal w/ Sim Super Resolution microscope. Regions of interest (ROIs) of 5µM each were demarcated on individual cells and selected ROIs on the membrane surface were stimulated with 2 loops of 100% intensity of 488nM laser for 2 secs. Thereafter, one image per second was acquired for fluorescence recovery in the photobleached regions for 60 secs. The FRAP data was normalized to the first data point following the photobleaching phase. The lateral diffusion of the IR was distinguished from the exocytic recycling by the way the ROI was bleached. If a central ROI on the plasma membrane was bleached and followed by FRAP, the recovery of IR-GFP in the bleached ROI was attributed to the lateral diffusion coupled with exocytic recycling of IR. If regions flanking the central ROI were bleached, then the recovery of IR-GFP in the central ROI was attributed exclusively to the phenomenon of exocytic recycling. Data from the recovery phase was analyzed by nonlinear one-phase recovery equation on regression on Graph Pad Prism. Half-lives were calculated from the first-order rate constants ($t_{1/2}$= 0.693/k) derived from one-phase exponential recovery fits for each cell. Half-lives were averaged and the mean values are tabulated in tables 6.1 and 6.2. The diffusion

coefficient was calculated from the derived half-lives by the following equation:

$$D = \frac{\pi\, x\, d^2}{4t_{half}}$$

6.5.4 Effect of Aß peptides on insulin-mediated signal transduction in the PI3K and the MAPK pathway: Lysates obtained from treating hCMEC/D3 cells in a similar treatment design as followed in the Western Blot analysis, were diluted and arrayed on nitrocellulose-coated slides. RPPA samples were then probed with 305 antibodies by tyramide-based signal amplification approach and visualized by DAB colorimetric reaction. Slides were scanned and density was quantified by Array-Pro analyzer. Relative protein levels for each sample was determined by interpolation of each dilution curves from the standard curve (supercurve) of the slide (antibody).

Supercurve is constructed by a script in R developed by RPPA core laboratory in MD Anderson. All the data points were normalized for protein loading and transformed to linear value, designated as Normalized Linear values. Normalized Linear expression values were used for differential analysis.

6.6 Results

Binding of insulin to a cell surface leads to phosphorylation of the IR at the tyrosine residues of the ß-subunit. The autophosphorylation of the IR ß-subunit promotes further downstream phosphorylation and activation of signaling cascades which consequently impact mechanisms of insulin transcytosis across the endothelium. It is contended that the internalization and distribution of activated receptors within the cell influences the above mechanisms. The spatial

path followed by the internalized IR complex affects the initiation of signaling in substrates downstream of IR. The kinetics of localization of the activated receptor complexes within endosomal compartments affects the activation of different signaling pathways and thereby, the mitogenic or metabolic actions of insulin within the cell and its transcytosis across the cell.

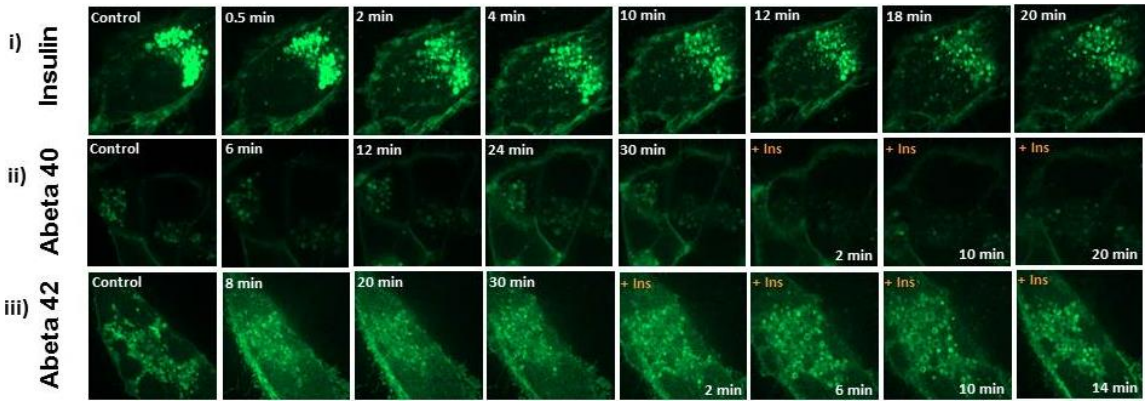

Figure 6.2 Confocal imaging of IR-GFP in hCMEC/D3 monolayers following insulin, Aß40 or Aß42 treatment**.** (i) hCMEC/ D3 monolayers over-expressed with an IR-GFP Wild-Type DNA construct were stimulated with insulin (i), with or without prior exposure to Aß40 (ii) and Aß42(iii). Following treatment, single cells were imaged live under a spinning-disc confocal microscope (100X oil-immersion objective) at brief intervals until 20 minutes. The expression of IR-GFP on the membrane surface of the imaged cell was observed.

Interestingly, we observed that insulin triggered the cell surface expression of IR-GFP within 2 minutes of exposure (figure 6.2). The surface expression remained intact until 12 minutes following which the expression declined. In presence of Aß40, the surface expression of IR-GFP increased however there was no observable change to the magnitude of surface IR-GFP expression following insulin treatment to the same cell. In the presence of Aß42, the surface expression of IR-GFP declined after 30 minutes. Further, when exposed to insulin, the cell surface did not depict any changes in IR-GFP expression.

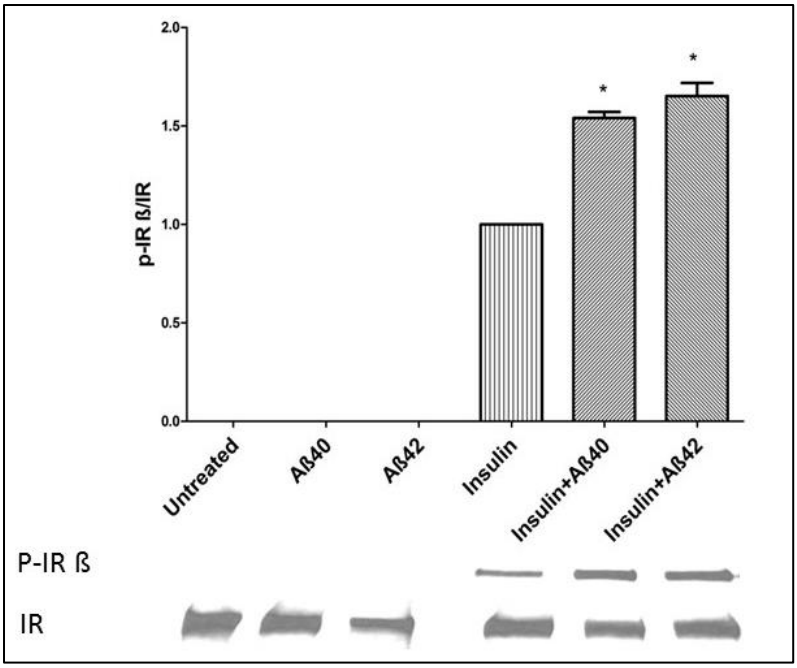

Figure 6.3. Activation of p-IRβ in the PI3K pathway in hCMEC/D3 monolayers treated with insulin, Aß40 or Aß42**.** Modulation of. insulin receptor beta subunit phosphorylation at Tyr1162/1163 by Aβ proteins in IR-overexpressed hCMEC/D3 cells was measured after pre-incubation with 6.2 μM Aβ40 or Aβ42 for 30 min, the hCMEC/D3 cells were treated with 100 nM insulin for 5 min to assess the extent p-Irβ activation. The Western blot analyses of hCMEC/D3 cell lysates followed by densitometry have shown that the p-Irβ/Irβ of insulin-treated hCMEC/D3 cells increased significantly in the presence of both Aβ40 ($p<0.05$) and Aβ42 ($p<0.01$)

The transport arm of my theis investigation in chapter 5 unearthed critical changes in the behavior of insulin in its transcytotic passage across the hCMEC/D3 monolayer. Following that, we probed the phosphorylation of critical events in the phosphatidylinositol-3-kinase (PI3K) pathway which regulates the downstream metabolic actions of insulin. Insulin binds to the insulin receptor-ß subunit thereby triggering the binding and activation of downstream substrate proteins and molecules in the PI3K pathway. It leads to the phosphorylation of the Akt (protein kinase B) molecule which functions as a fork-out event for the metabolic and transcriptional activities mediated by insulin. We discovered that

pre-incubation with Aß peptides, Aß40 and Aß42 resulted in an increase in the phosphorylation of the insulin receptor-ß subunit after 5 minutes of insulin treatment. Further, phosphorylation of the Akt molecule was inhibited following Aß40 incubation and significantly enough, following Aß42 incubation.

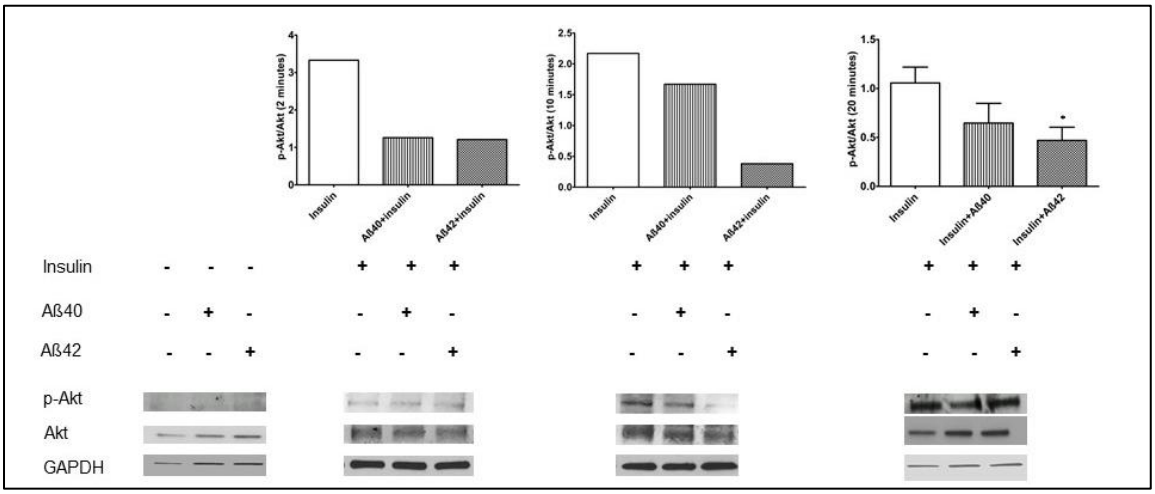

Figure 6.4. Activation of pAkt in the PI3K pathway in hCMEC/D3 monolayers treated with insulin, Aß40 or Aß42**.** Modulation of Akt (Protein kinase B) phosphorylation at Ser473 by Aβ proteins in IR-overexpressed hCMEC/D3 cells was assessed following pre-incubation with 6.2 μM Aβ40 or Aβ42 for 30 min, the hCMEC/D3 cells were treated with 100 nM insulin for 2, 10 or 20 min to assess the extent p-Akt activation. The Western blot analyses of hCMEC/D3 cell lysates followed by densitometry have shown that the p-Akt/Akt increased significantly 20 minutes following insulin treatment in cells incubated with Aβ42 ($p<0.05$)

Figure 5.4 depicts the changes in fluorescence recovery after photobleaching for unstimulated insulin receptors, insulin treated, Aß40 treated, Aß42 treated, insulin treatment after Aß40 preincubation.

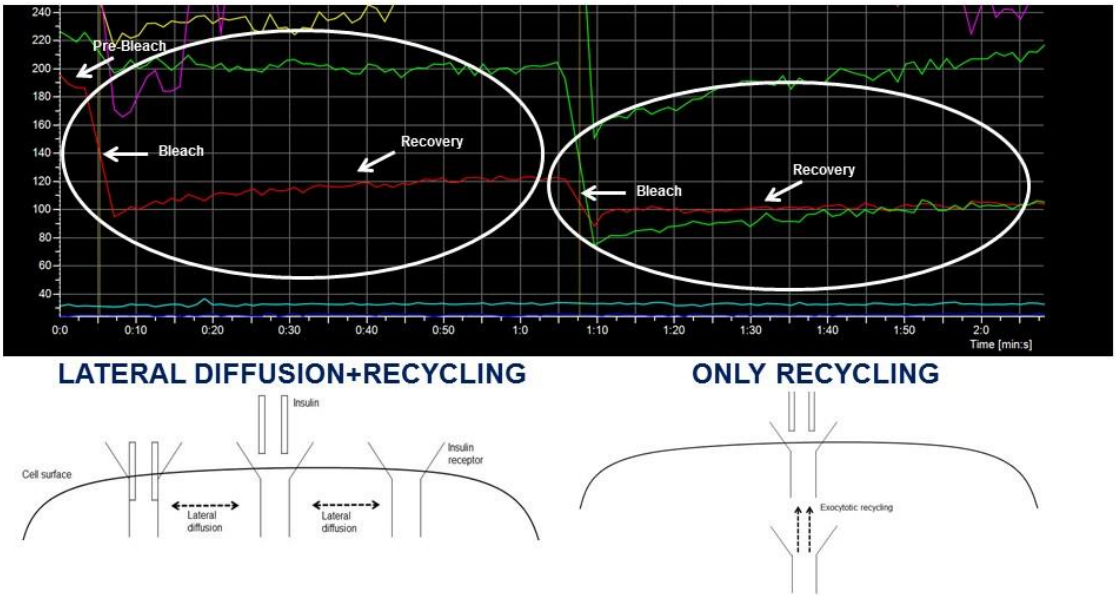

Figure 6.5: Example of a FRAP/FLIP measurement obtained from the Nikon Super Resolution imaging software**.** On the FRAP/FLIP readout, the y-axis denotes the IR-GFP intensity and the x-axis denotes the time (mins). The diagrams ('Lateral diffusion & recycling' and 'only recycling') explain the purported molecular mechanisms underlying the labeled acquisition phases in the readout.

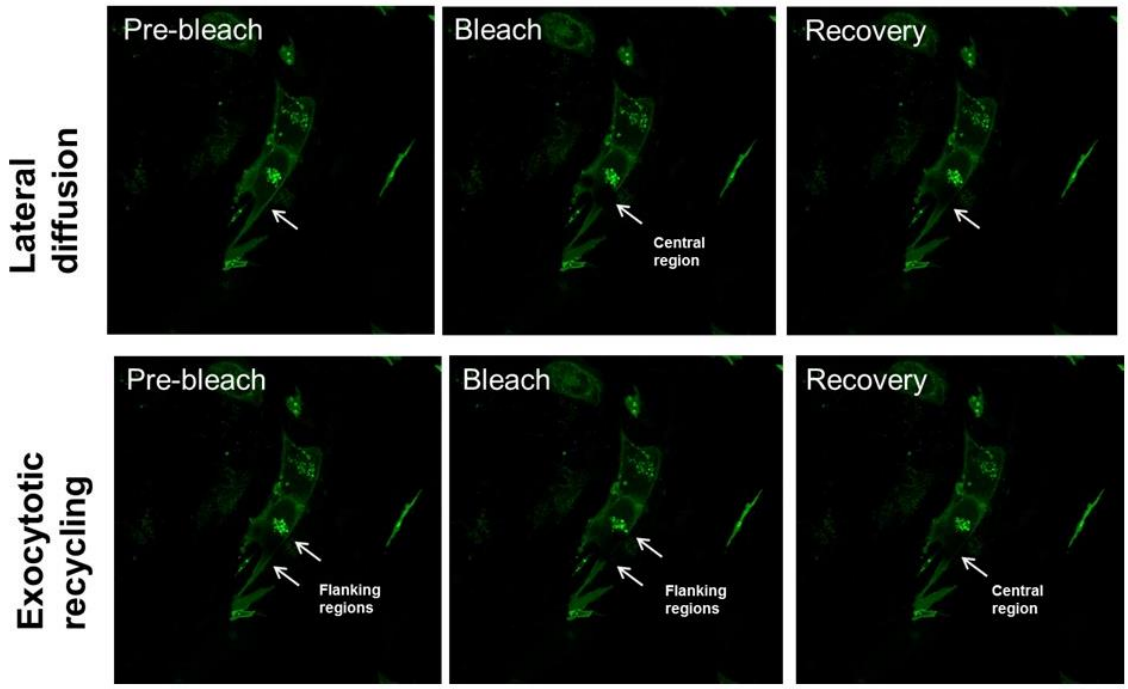

Figure 6.6: FRAP/FLIP protocol for imaging lateral diffusion and exocytic recycling of IR-GFP in hCMEC/D3. Images in the upper panel describe a FRAP protocol of selecting a central ROI, acquiring fluorescence intensity prior to bleaching for 5 secs (left), photobleaching the central ROI for 2 secs (center) and acquiring fluorescence intensity post bleaching for 60 secs recovery. Images in the lower panel describe the FLIP protocol in which, following the FRAP acquisition, two ROIs flanking the bleached central ROI are chosen. Fluorescence intensity of the selected flanking regions are measured for 60 more seconds in a similar sequence as the FRAP mode i.e. pre-bleach, bleach and recovery phases.

The corresponding table shows the estimates for the half-time and the diffusion coefficient derived from fitting the one-phase recovery equation to the sample data on Graph Pad Prism.

LATERAL DIFFUSION combined with RECYCLING

	Untreated	Insulin	Aß40	Aß42	Aß40+insulin	Aß42+insulin
Half life	26.35	17.10	26.90	23.42	22.96	21.534
Diffusion coefficient ($\mu m^2/s$)	3.23	4.99	3.17	3.64	3.71	3.96

Table 6.1: Kinetic parameters of IR mobility as a function of peptide treatment. The mean half-time of lateral diffusion was derived from fitting mono-exponential recovery curves to the FRAP analysis of IR-GFP overexpressed hCMEC/D3 monolayers. Diffusion coefficient was calculated by the formula ($D = \pi\, x \frac{d^2}{4X\ thalf}$)

ONLY RECYCLING

	Untreated	Insulin	Aß40	Aß42	Aß40+insulin	Aß42+insulin
Half life	36.12	17.29	50.75	35.99	20.1	30.64
Diffusion coefficient ($\mu m^2/s$)	2.36	4.93	1.68	2.37	4.24	2.78

Table 6.2: Kinetic parameters of IR mobility as a function of peptide treatment. The mean half-time of exocytic recycling was derived from fitting mono-exponential recovery curves to the FRAP analysis of IR-GFP overexpressed hCMEC/D3 monolayers. Diffusion coefficient was calculated by the formula ($D = \pi\, x\, \frac{d^2}{4X\ thalf}$)

When the IR-GFP transfected cells were treated with an agonist (insulin), the region of interest was bleached rapidly. The fluorescence in the bleached region recovered at a faster rate upon insulin exposure than the untreated controls or the Aß40 or Aß42 pre-treated samples. The half-time of IR-GFP recovery by lateral diffusion (figure 6.7) was significantly higher for hCMEC/D3 exposed to 250nM insulin than for hCMEC/D3 monolayers treated with the same concentration of insulin following a pre-exposure to 25µg/ml of Aβ42 ($p<0.05$) and Aβ40 ($p<0.01$; one-tailed t-test). This clearly demonstrates that the insulin-mediated IR-GFP in hCMEC/D3 were significantly more mobile those incubated with Aβ peptides. Aß40 and Aß42 pre-treatment for 1 hour caused the insulin receptor to recover at a rate similar to the untreated cells. To demonstrate that newly-synthesized IR-GFP did not contribute to recovery in fluorescence, a region of interest in the nucleus was tracked for changes in fluorescence intensity and used as a control to normalize the resultant recovery. Next, to account for the component of exocytic recycling, flanking regions adjacent to the central ROI was bleached and FRAP was conducted. Half-times of IR-GFP exocytic recycling for insulin or Aβ peptide-treated hCMEC/D3 cells derived from the one-phase recovery curves were not significantly different from the untreated controls. This proved that lateral diffusion is a significant component of IR recycling and is perturbed by prior exposure of BBB endothelial cells to Aβ40 and Aβ42.

Images from spinning disc confocal microscopy (Figure 4.1) provided qualitative evidence to the conclusion that, in presence of Aß40 and Aß42, stimulated IR-GFP to be expressed at the plasma surface at a slower rate than the insulin-treated cells. The FRAP data correlate with the results in from the spinning disc confocal microscopy and provide a quantitative measure of the diffusion coefficient and the half-life.

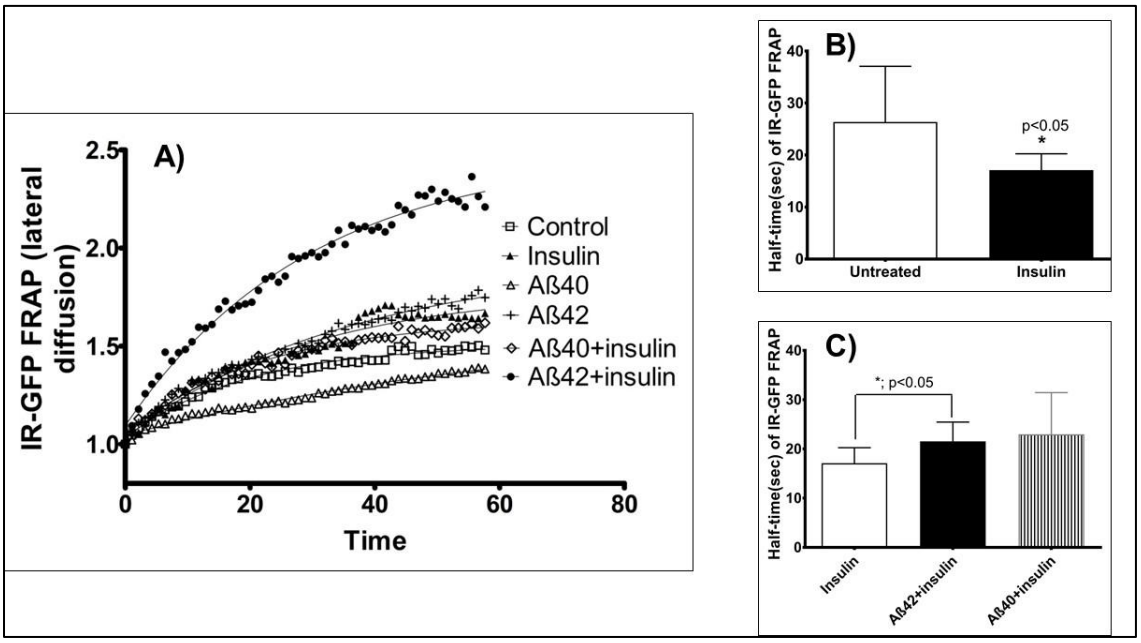

Figure 6.7. FRAP curves and half-times for lateral diffusion coupled with exocytic recycling of IR-GFP in hCMEC/D3 monolayers treated with insulin with or without 1 hour pre-exposure to Aβ40 or Aβ42. Fig. A) FRAP one-phase exponential recovery curves depicting IR-GFP lateral diffusion, coupled with exocytic recycling in hCMEC/D3 treated with insulin with or without pre-exposure to Aβ40 or Aβ42. Fig B) Half-time (sec) (mean+S.D) of lateral diffusion of IR-GFP in untreated (n=9) hCMEC/D3 monolayers is significantly higher than for hCMEC/D3 monolayers treated with 250nM insulin (n=8); $p<0.05$ Fig C) Half-time (sec) of lateral diffusion of IR-GFP in hCMEC/D3 monolayers treated with insulin (250nM) is significantly lower than those pre-exposed to 25 µg/ml of Aβ42 (n=5); $p<0.05$, two-tailed t-test; and lower than hCMEC/D3 exposed to 25µg/ml of Aβ40 (n=4); $p<0.1$; one-tailed t-test. Statistical comparisons were conducted through t-tests on Graph Pad Prism 7©.

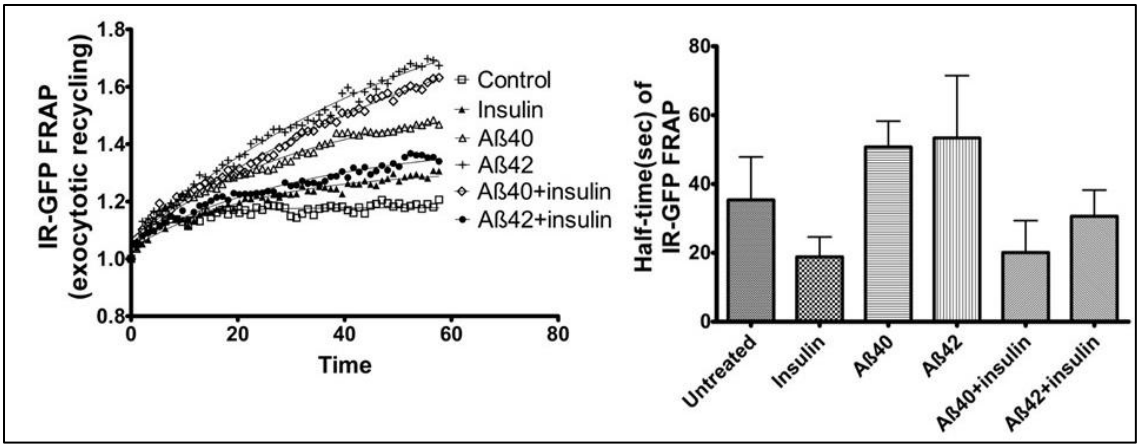

Figure 6.8. FRAP curves and half-times for exocytic recycling of IR-GFP in hCMEC/D3 monolayers pre-treated for insulin in presence of Aβ40 or Aβ42. Figure on the left depicts FRAP one-phase exponential recovery curves describing IR-GFP exocytic recycling in hCMEC/D3 treated with insulin with or without pre-exposure to Aβ40 or Aβ42. Figure on the right is a plot of the half-time (sec) of lateral diffusion of IR-GFP for all treatments. Statistical comparisons conducted through one-way ANOVA (corrected for multiple comparisons) and t-tests on Graph Pad Prism 7© confirmed that observed differences in half-times (mean+S.E) for IR-GFP in hCMEC/D3 exposed to various treatments were insignificant.

Diffusion coefficients reveal that the mobility of insulin receptor is decreased within the cytoplasm in presence of insulin. However, it is further decreased in presence of Aß40 and Aß42. Further, Aß40 pre-incubated sample decreases the diffusion coefficient more than with samples with no exposure to the inhibitory peptides.

Caveolin-1 microdomain within the caveolae domains are essential for IR endocytosis because it binds to the IR following phosphorylation of its tyrosine residues. In the state of insulin resistance, tyrosine phosphorylation of caveolin-1 is inhibited, leading to a movement of IR away from the binding domain of caveolin-1, as represented in the following figure (Kabayama et al., 2007).

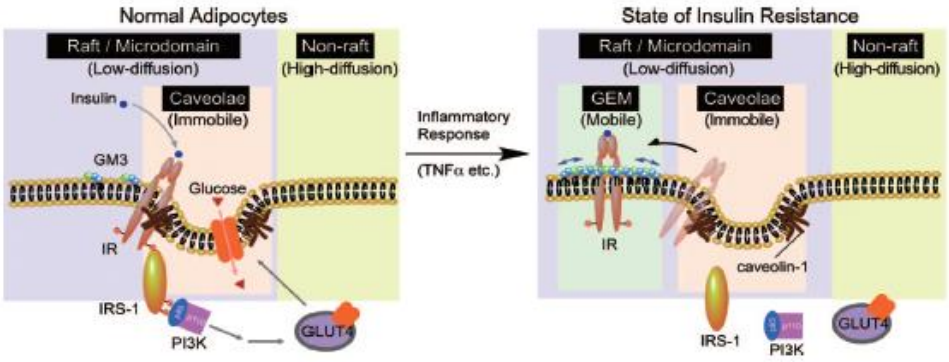

Figure 6.9. Schematic representation of the role of caveolin-1 in the development of an insulin resistant state in cells (Kabayama et al., 2007)

MβCD (Methyl beta-cyclodextrin) depletes cholesterol within the cell and thereby disrupts signaling in the lipid rafts (Kabouridis PS, 2000). We assessed the uptake of FITC-insulin (100 nM) in hCMEC/D3 cells pre-incubated for 1 hour with 5 mM of MβCD. Interestingly, we found that MβCD significantly inhibits the uptake of FITC-insulin within the cells. This assay proved that lipid raft signaling is critical for insulin uptake into cells.

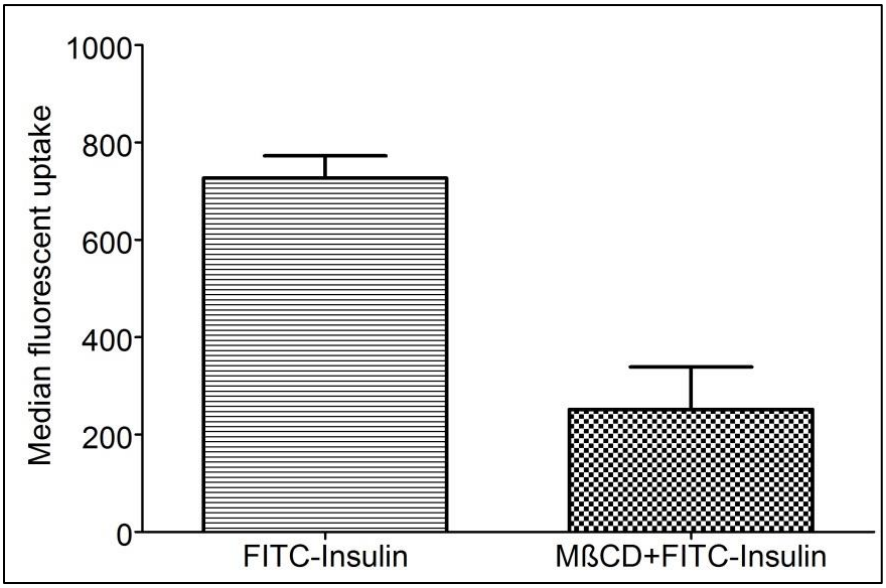

Figure 6.11 Median fluorescent uptake of FITC-insulin in hCMEC/D3 following incubation with MβCD (5mM for 1 hour)

The purpose of the RPPA assay was to analyze the activation of several proteins, in addition to cav-1, as a function of Aß peptide exposure followed by insulin treatment in hCMEC/D3 cells.

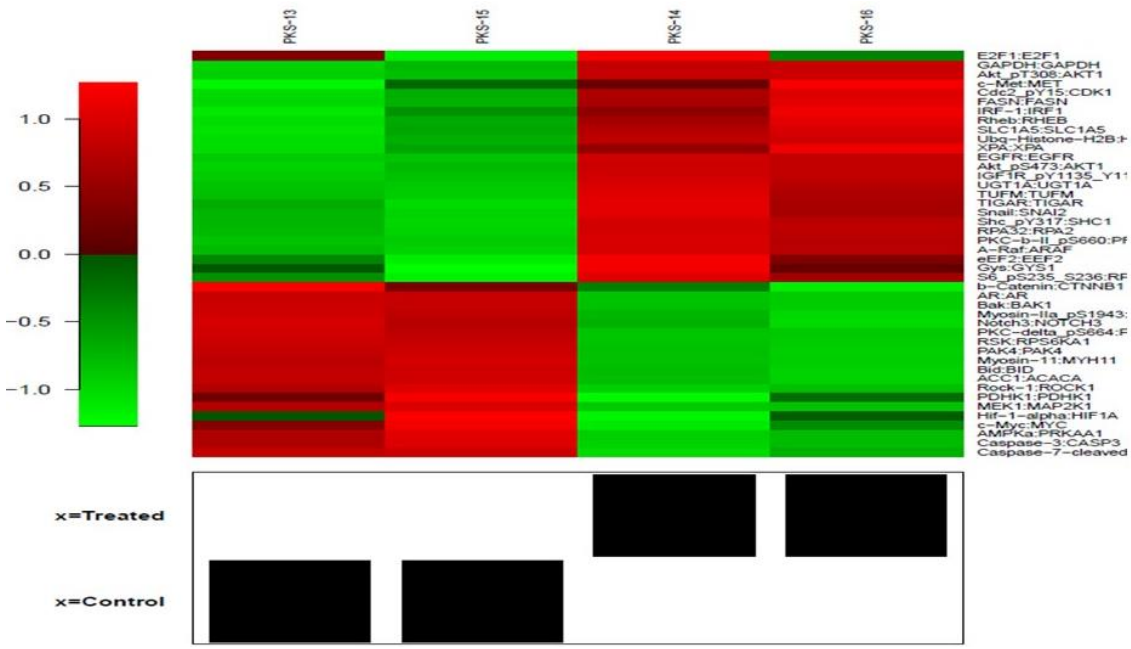

Figure 6.12 Heat map of the effects of insulin treatment on activation of important genes in hCMEC/D3.

Gene Name	**Antibody Name**	**pvalue**
CDK1	Cdc2_pY15	0.002502
SHC1	Shc_pY317	0.012704
AKT1	Akt_pT308	0.018852
PRKCD	PKC-delta_pS664	0.020122

MYO2A	Myosin-IIa_pS1943	0.021321
PRKCB	PKC-b-II_pS660	0.033947
IGF1R	IGF1R_pY1135_Y1136	0.035282
RPS6	S6_pS235_S236	0.04909
AKT1	Akt_pS473	0.049154

Table 6.3: List of genes significantly expressed following insulin treatment of hCMEC/D3.

Paired t-test was used to identify differentially expressed proteomic signatures (protein and phosphorylation sites) post insulin treatment. We identified about 35 protein sites and 9 phosphorylation sites that were significantly different between control and insulin-treated groups. Further, hierarchical cluster analysis was performed using a set of dissimilarities for the top 44 significant phospho-proteomics signatures. Dissimilarity matrix(D) was calculated using the formula D=1-correlation. Initially, each object was assigned to its own cluster and then the algorithm proceeds iteratively, at each stage joining the two most similar clusters, continuing until there is just a single cluster. At each stage distances between clusters are recomputed by the Lance–Williams dissimilarity update formula per the "*complete"* clustering method. *"Complete linkage"* clustering method finds similar clusters.

6.7 Discussion

Findings from this chapter represent the first reported examination of dynamics of IR within the BBB endothelium under conditions mimicking early stage AD. It helped answer crucial questions regarding perturbation of trafficking and

signaling pathways of IR at the BBB endothelium as a consequence of Aβ peptide exposure. Answers were derived by applying variations of confocal imaging and blotting techniques to investigate the impact of Aβ peptides on signaling and trafficking processes of IR at the BBB endothelium, with or without insulin treatment.

To visualize the surface expression and intracellular trafficking of IR as a response to insulin treatment, we conducted spinning disc confocal microscopy of single cells overexpressed with IR-GFP. The protocol employed for the imaging assay afforded a dynamic and resolute examination of endocytosis of IR-GFP within few minutes of insulin treatment. Figure 5.1 proved that insulin exposure induces an increased expression of IR on the plasma membrane surface and rapid endocytosis of IR-GFP in hCMEC/D3. It firmly contrasted the images depicting the limited insulin-induced surface expression of IR when preceded by an incubation with 3.1 μM of Aβ40 or Aβ42 for 1 hour. Intriguingly, Aβ40 and Aβ42 induced IR-GFP expression on the plasma membrane surface of hCMEC/D3, albeit at a time point later than that observed following insulin treatment. This train of evidence leads us to infer that Aβ40 and Aβ42 possibly inhibit the intracellular events regulating the insulin-induced mobility of IR. It lends credibility to the evidence-based suggestion of an uncompetitive inhibition of IR in hCMEC/D3 by Aβ40 (from chapter 4).

Following a qualitative visualization of IR mobility from the hCMEC/D3 plasma membrane to cytosol and vice-versa, we decided to quantitatively dissect the mechanisms of IR movement within hCMEC/D3 on a premise that this approach

contained a two-pronged significance. First, it would enable us to visually distinguish lateral diffusion of IR on the plasma membrane from its exocytic recycling in the cytosol of hCMEC/D3. Second, data obtained from these two processes of movement could be modeled to provide us with the half-life and diffusion coefficient of IR in response to Aβ peptides treatment.

To that extent, we devised a FRAP-FLIP protocol based on a method described by Hildick et al, 2012. The process of lateral diffusion combined with recycling was delineated from the FRAP segment of the protocol. FRAP data of a marked central ROI on the plasma membrane of peptide-treated IR-GFP over-expressed hCMEC/D3 were normalized to the extent of photobleaching of the ROI. The phenomenon of exocytic recycling was dissected by a sequence of FRAP followed by FLIP. FLIP method was employed by bleaching two regions adjacent to the central ROI to obviate lateral diffusion of IR into the central ROI, thereby ensuring the diffusion of only IR undergoing exocytosis from within the cytosol. Modeled data revealed that the half-life of insulin for the phenomenon of lateral diffusion and recycling was lower than that for hCMEC/D3 treated with insulin after 1 hour exposure to Aβ40 and Aβ42. Similarly, the diffusion coefficients for insulin in the above case were higher than those for cells treated with the AD peptides. These findings imply that Aβ peptides increase the time required for surface expression as well as exocytosis of IR at hCMEC/D3. It corroborates the spinning disc confocal microscopic observation of a delayed Aβ peptide-induced surface expression of IR.

Studies of signaling pathway activation were performed to provide a biochemical basis for the observation of perturbed IR dynamics following Aβ exposure. Western Blots and RPPA techniques were employed to assess the activation of intracellular signaling pathways in hCMEC/D3 as a response to Aβ peptide treatment. Western Blot analysis of IR-β subunit revealed that a 1 hour pre-exposure to 3.1 μM of Aβ peptides significantly increased the insulin-induced phosphorylation of IR-β after 5 minutes of treatment. Similarly, a 1 hour pre-incubation with 3.1 μM of Aβ40 and Aβ42 significantly reduced the activation of Akt in the PI3K pathway at 5 and 20 minutes following insulin treatment.

Modulation of activation of critical molecular regulators in the PI3K pathway prompted us to conduct an RPPA assay to simultaneously assess the disposition of several key molecular players in the PI3K as well as the MAPK pathway. RPPA analysis revealed that caveolin-1 phosphorylation was reduced and MAPK3 expression was increased in in hCMEC/D3 cells in response to Aβ40 and Aβ42 treatment. The observation of reduced caveolin-1 expression as a function of Aβ40 and Aβ42 treatment aligns well with the finding that insulin uptake into hCMEC/D3 is lowered following a pre-incubation with 5mM of MβCD, a lipid raft disruptor. Since caveolin-1 is a protein expressed with lipid rafts, these pieces of evidence emphasize the significance of caveolin-1 in lipid raft signaling. It implies the fact that disruption of caveolin-1 is likely associated with the disruption of IR trafficking within lipid rafts, an event critical for the uptake of insulin. The effect of Aβ peptides on insulin-induced IR trafficking within lipid rafts, however, remains to be studied in finer subcellular detail.

CHAPTER 7. CONCLUSIONS AND SCOPE FOR FURTHER RESEARH

7.1 Summary of findings: The pathogenesis of Alzheimer's disease (AD) remains unclear, however there is strong evidence that the blood-brain barrier (BBB) is a key contributor to the cascade of neurological damage. The cerebrovasculature, a component of the BBB, is understood to be a significant portal for the clearance of Aß peptides, Aß40 and Aß42, the primary biomarkers for AD. The BBB endothelium also serves as a structural barrier to the passage of insulin into the brain, where insulin regulates glucose uptake and maintains cognitive levels in its capacity as a growth factor. Findings from Chapter 2 of this thesis (summarized in Figure 7.1) established that insulin administered into the systemic circulation enhances the trafficking of Aβ40 into the brain and the trafficking of Aβ42 out of the brain, thereby suggesting that a therapeutic Aβ40: Aβ42 ratio could be maintained with sustained insulin action. The trends suggested by the influx clearance and brain amounts for Aβ40 and Aβ42 in response to insulin administration were confirmed by three-compartmental model (SAAM II©, Stella©) based predictions of brain uptake of the peptides. Swaminathan et al, 2017 have further demonstrated that the insulin-mediated Aβ trafficking occurs via the BBB endothelium through significant modulations in BBB membrane receptor-mediated trafficking, permeability and exocytosis of Aβ40 and Aβ42.

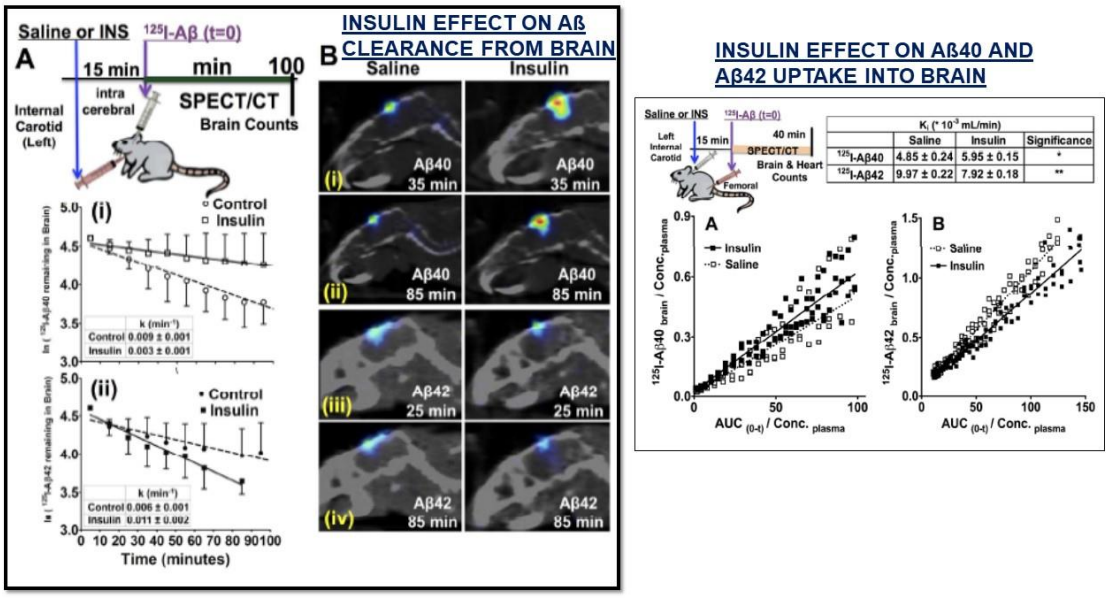

Figure 7.1. Insulin regulates the brain-to-plasma clearance of Aß40 and Aß42: The figure on the left shows that a 15-minute infusion of 1 IU of insulin via the left internal carotid artery increases the flux of ^{125}I-Aß40, but not of ^{125}I-Aß42 from the brain to plasma. The figure on the right depicts the influx clearance of ^{125}I-Aß40and ^{125}I-Aß42 as calculated from Patlak analyses. The influx clearance of ^{125}I-Aß40 and ^{125}I-Aß42 are significantly increased and decreased in response to administration of 1IU via the internal carotid.

Considerable research from the last decade has, however, generated a consensus that brain regions displaying an excessive accumulation of Aβ plaques are strongly associated with low expression of insulin and an impairment of insulin-mediated signal transduction. It is also known that peripheral hyperinsulinemia is a risk-factor for the development of neuritic plaques in AD. There exists a strong likelihood that hyperinsulinemia affects the BBB phenotype which in turn, modulates the clearance of Aβ peptides and exacerbates the pathophysiology and symptoms of AD. Intranasally administered insulin ensures the availability of insulin in the CSF and alleviates deficits in memory processes associated with mild-cognitively impaired (MCI) patients. However, it is possible that chronic exposure of insulin-resistant brains to intranasal insulin may negate

positive outcomes. Besides, there is no reported data on the effective BBB response or causal effect of Aβ peptides on the brain availability of insulin from trials through this route of administration. The aim of my thesis was to primarily assess the relation between peripheral and brain levels of insulin as a function of Aβ peptide exposure in the systemic circulation and brain. This relation was initially assessed in APP/PS1 transgenic mice, which are characterized by abnormal levels of Aβ40 and Aβ42. Our preliminary investigations demonstrated that APP/PS1 transgenic mice display a peripheral resistance to insulin. Moreover, the clearance of insulin is significantly increased in APP/PS1 mice. Further, the influx of insulin into the brain and its accumulation was significantly decreased in APP/PS1 and verified in db/db mice, which are also characterized by a resistance to insulin. The first-order elimination of ^{125}I-insulin was significantly increased in APP/PS1 mice upon an intracerebral administration (summarized in Figure 7.2). These results indicated that a resistance to insulin in the periphery modulates its plasma-to-brain kinetics and lowers brain levels of insulin in mice displaying AD-like characteristics. 3-compartmental model simulations of these findings predicted a decrease in the brain AUC of insulin in APP/PS1, db/db and ageing mice thereby corroborating results from Patlak multiple-regression analyses.

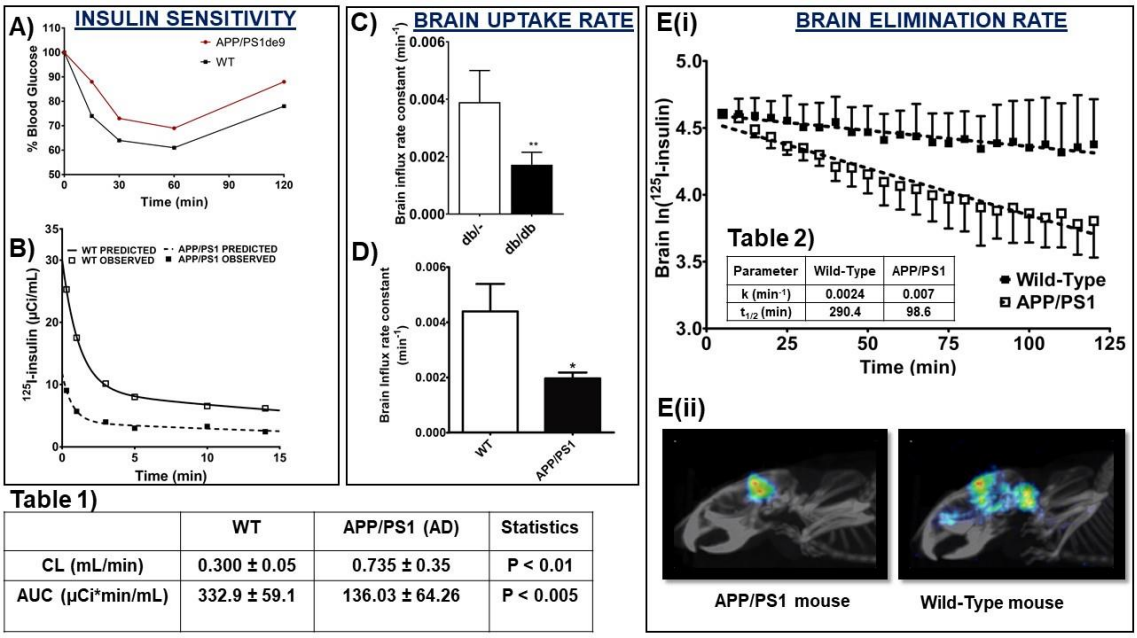

Table 1)

	WT	APP/PS1 (AD)	Statistics
CL (mL/min)	0.300 ± 0.05	0.735 ± 0.35	P < 0.01
AUC (µCi*min/mL)	332.9 ± 59.1	136.03 ± 64.26	P < 0.005

Figure 7.2. Resistance to insulin in the periphery leads to a decrease in the brain uptake of insulin in AD transgenic (APP/PS1) mice: Fig 1A) In response to an insulin injection (0.6 mU/g) into mice, db/db mice levels of glucose are higher over the time period as compared to db negative and WT mice, indicating a lack of peripheral insulin sensitivity. Fig 1B) Brain influx rate constant of insulin is significantly lower for APP/PS1 mice compared to WT mice. Fig 1C) Brain influx rate constant (min^{-1}) of insulin (ml/min) is significantly lower for db/db mice as compared to db/db mice. Fig 1D) Reduction in brain influx rate constants is corroborated by an increased clearance of ^{125}I-insulin from the plasma in APP/PS1 mice, accompanied by a reduction in AUC (Table 1) in the plasma. Fig 1Ei) Following intracerebral injection, the decline in ^{125}I-insulin in APP/PS1(n=5) brains with time is significantly faster (Table 2) as compared to that from WT mice. Fig 1Eii) SPECT/CT scans of the brain ROI in APP/PS1 and WT mice following 50 mins of intracerebral administration of ^{125}I-insulin indicate a significant reduction in intensity of ^{125}I-insulin in APP/PS1 brains

Having established that peripheral resistance to insulin translates to a lowered availability in the APP/PS1 brain through modulation of influx, efflux and tissue distribution kinetics, the role of Aβ peptides in this kinetic modulation was investigated. To that effect, WT mice were exposed to higher dose infusions (500 µg/60 mins) of Aβ40 and Aβ42 and the peripheral and brain distribution of 100 µCi of ^{125}I-insulin was calculated. Findings from this study negated the

presumption that increased levels of peripheral insulin should translate to increased brain levels by proving that AUC of insulin in the plasma was

Figure 7.3. Aß40 and Aß42 disrupt peripheral pharmacokinetics and reduce brain availability of insulin. Fig. 3A. Schematic depicting saline or Aß peptide infusion via the left internal carotid artery for 60 minutes, followed by an 125I-insulin bolus via the femoral vein and extraction of brain tissue. Fig. 3B. The brain radioactivity of 125I-insulin normalized to the AUC is significantly lower for mice pre-infused with Aß40 and Aß42. Table 3) Plasma PK analysis of mice subjected to the same experiment as depicted in A(i) revealed that the clearance of ^{125}I-insulin in presence of Aß40 and Aß42 is decreased and the AUC is increased, suggesting that Aß peptides disrupt both the peripheral pharmacokinetics of insulin.

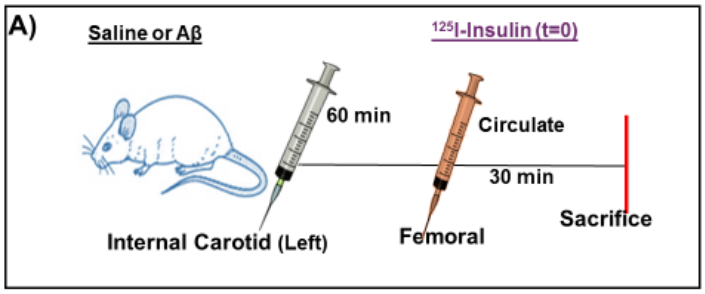

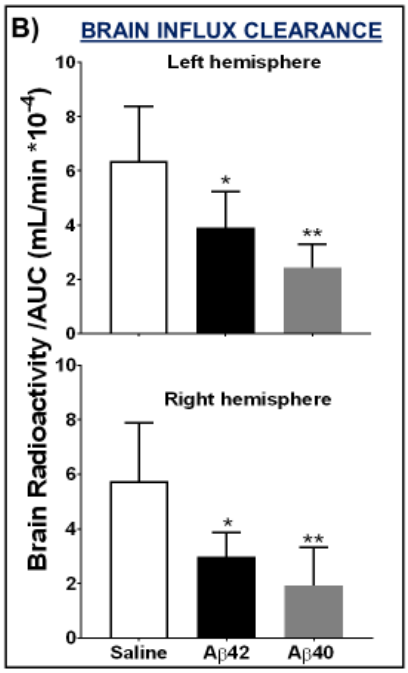

Table 3)

	SALINE	Aβ42	Aβ40	Statistics
CL (Mean ± SE)	0.725 ± 0.09	0.577 ± 0.07	0.435 ± 0.07	P < 0.0001, F (2,14) = 19.6
AUC (Mean ± SE)	137.93 ± 17.33	173.25 ± 20.72	229.81 ± 37.50	P = 0.0001, F (2,14) = 18.87

excessively increased in contrast to brain levels (normalized to plasma AUC) which were decreased due to Aβ40 and Aβ42 peptide exposure. In other words, the influx clearance was decreased, in agreement with the observation in APP/PS1 mice. The implications of these findings in context of brain accumulation of insulin over a period of 45 minutes were predicted on SAAM©. The brain AUC was predicted to be lowered in response to an experimentally-

derived mean parameter input specific to the influence of Aβ peptide administration uptake.

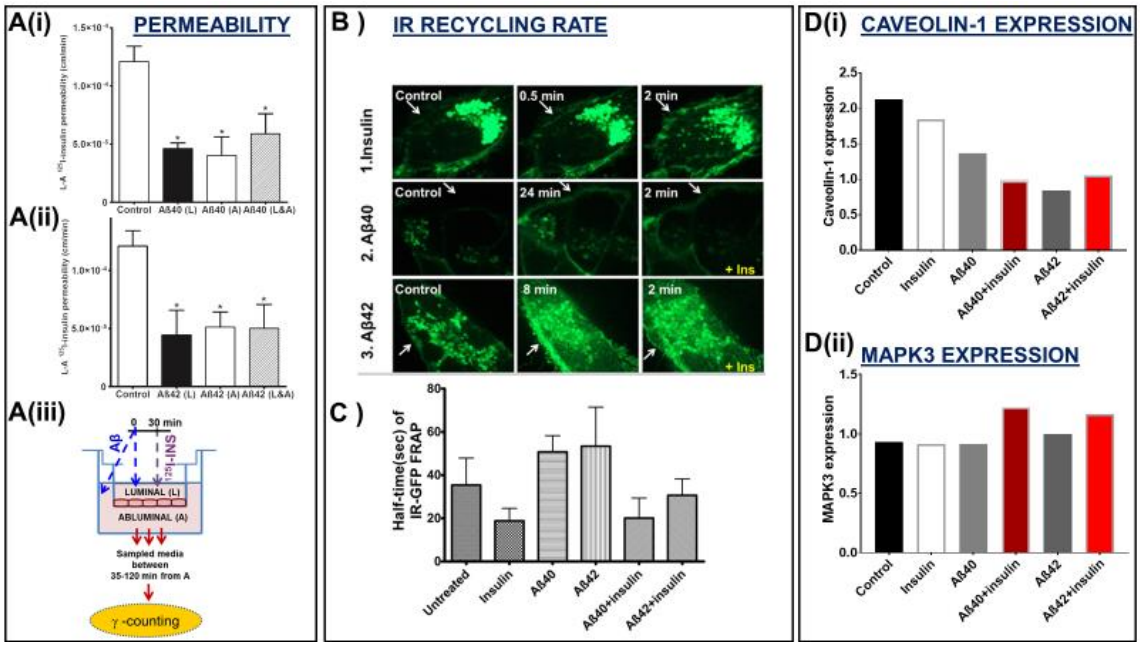

Figure 7.4. Aß40 and Aß42 perturb insulin receptor (IR)-mediated trafficking and signaling mechanisms at the cerebrovascular endothelium. **Fig. 4.** In A(i) and A(ii), Aβ40 and Aβ42, respectively, decrease the luminal-to-abluminal permeability of ^{125}I-Insulin in hCMEC/D3 cells. A(iii) represents a schematic of the permeability experiment setup. In fig. B, the first panel shows that the expression of IR-GFP on the surface of hCMEC/D3 cells is increased, 2 minutes following insulin addition to the cell monolayer. The middle panel shows the effects of Aß40, wherein it increases the expression of IR, albeit at a time point longer than that compared to insulin treatment in the first panel. Intriguingly, when treated with insulin, IR-GFP expression on the surface remains the same. In the lower panel, Aß42 again, increases the surface expression of IR-GFP, but when treated with insulin, surface expression decreases. These results are corroborated from results from a FRAP assay shown in Fig. C wherein the half-life of IR-GFP exocytosis through hCMEC/D3 following insulin treatment is lower than that for the untreated sample; whereas in presence of Aß40 and Aß42, the half-life is higher than that for untreated samples. The half-lives of IR-GFP exocytosis decrease when insulin is added following a pre-exposure to Aß40 or Aß42. In fig. D, a Reverse Phase Protein Array (RPPA) assay was conducted to examine the activation of 300 molecules in the IR signaling pathway. Fig. D (i) shows the caveolin-1 expression for all treatments following RPPA. The caveolin-1 expression decreases when pre-incubated with Aß40 or Aß42, and does not differ when insulin is added following the pre-exposure. Fig. D(ii) displays MAPK3 expression for all treatments following RPPA. Expression of MAPK3 increases for insulin treatment only when pre-treated with Aß40 and Aß42.

A lack of proportional increase in the brain in response to high levels of peripheral insulin, coupled with no significant difference in insulin elimination between groups (compartmental model predictions) suggested that the BBB endothelium could possibly restrict insulin permeability in Aβ-treated groups. Since the phenotype of the BBB in-vivo is not amenable to non-invasive examination, I undertook a reductionist approach and utilized an immortalized BBB endothelial cell line to test the hypothesis that Aβ exposure reduces insulin flux into the brain. I discovered that the IR-mediated uptake and permeability are decreased, whereas the rate of luminal exocytosis for insulin is significantly increased due to a 1 hour incubation of hCMEC/D3 cells with 6.2 μM of Aβ40 and Aβ42. I also found that Aß40/42 impair the insulin receptor (IR)-mediated endocytosis processes regulated by caveolin-1, and modulate the molecular cross-talk between PI3K (lowered p-Akt after 20 minutes) and MAPK signaling (increased MAPK3 after 10 minutes) pathways downstream of IR at the BBB.

7.2 Scope for further research: This dissertation establishes that insulin availability in the brain is imperative for regulation of Aβ40 and Aβ42 fluxes from brain-to-plasma and vice versa. The scope of these in-vivo findings lies in the capacity of ongoing or upcoming pre-clinical protocols to examine the trafficking of Aβ peptides in insulin-resistant mouse models. Studies could also assess the efficacy of IR sensitizing molecules on the regulation of insulin availability and subsequent Aβ trafficking and clearance and measure its association with tolerance of peripheral tissues to insulin. An important consideration will be the assessment of brain AUC values as a function of dose escalation for insulin and

Aβ from a normal to abnormal dose range, through various routes (intravenous, intraperitoneal, internal carotid). This relationship can possibly be correlated with glucose response, behavioral test results, and Aβ and Tau load in various brain regions. It is equally imperative to assess the structural integrity, receptor expression and signal transduction at the BBB vasculature through non-invasive techniques such as functional MRI or PET. Generation of baseline information from all of these segments pertaining to insulin resistance and AD progression will help form a robust framework for pre-clinical and clinical trials pertaining to IR sensitizing agents or combination molecular therapy.

Building on the intriguing in-vitro findings from chapters 5 and 6, studies examining the following associations between Aβ exposure, intra-endothelial trafficking of insulin and its flux into an AD brain will be crucial to understand the molecular mechanisms perpetuating the pathophysiological link between impaired amyloid clearance and lowered brain insulin availability.

A. Whether perturbation of lipid rafts by Aß peptides affects the endosomal signaling machinery.
B. Whether perturbation of endosomal signaling machinery affects the transcriptional response of cerebrovascular endothelium, and impacts the transcytosis of insulin across the BBB.

Addressing these will unequivocally answer the most significant question arising from my findings i.e. whether, or not, a rectification of impaired signaling motifs at the BBB will enhance the availability of insulin in the AD brain parenchyma and sustain a normal trafficking of Aβ40 and Aβ42.

BIBLIOGRAPHY

Abbott, N. J. (2002). Astrocyte-endothelial interactions and blood-brain barrier permeability. *J Anat, 200*(6), 629-638.

Alzheimer's, A. (2016). 2016 Alzheimer's disease facts and figures. *Alzheimers Dement, 12*(4), 459-509.

Armulik, A., Genove, G., Mae, M., Nisancioglu, M. H., Wallgard, E., Niaudet, C., . . . Betsholtz, C. (2010). Pericytes regulate the blood-brain barrier. *Nature, 468*(7323), 557-561. doi:10.1038/nature09522

Azizi, P. M., Zyla, R. E., Guan, S., Wang, C., Liu, J., Bolz, S. S., . . . Lee, W. L. (2015). Clathrin-dependent entry and vesicle-mediated exocytosis define insulin transcytosis across microvascular endothelial cells. *Mol Biol Cell, 26*(4), 740-750. doi:10.1091/mbc.E14-08-1307

Banks, W. A., Owen, J. B., & Erickson, M. A. (2012). Insulin in the brain: there and back again. *Pharmacol Ther, 136*(1), 82-93. doi:10.1016/j.pharmthera.2012.07.006

Bautch, V. L., & James, J. M. (2009). Neurovascular development: The beginning of a beautiful friendship. *Cell Adh Migr, 3*(2), 199-204.

Birtwistle, M. R., & Kholodenko, B. N. (2009). Endocytosis and signalling: a meeting with mathematics. *Mol Oncol, 3*(4), 308-320. doi:10.1016/j.molonc.2009.05.009

Bosco, D., Fava, A., Plastino, M., Montalcini, T., & Pujia, A. (2011). Possible implications of insulin resistance and glucose metabolism in Alzheimer's disease pathogenesis. *J Cell Mol Med, 15*(9), 1807-1821. doi:10.1111/j.1582-4934.2011.01318.x

Braak, H., & Braak, E. (1991). Neuropathological stageing of Alzheimer-related changes. *Acta Neuropathol, 82*(4), 239-259.

Bradbury, J. (2005). Hope for AD with NGF gene-therapy trial. *Lancet Neurol, 4*(6), 335.

Brankatschk, B., Wichert, S. P., Johnson, S. D., Schaad, O., Rossner, M. J., & Gruenberg, J. (2012). Regulation of the EGF transcriptional response by endocytic sorting. *Sci Signal, 5*(215), ra21. doi:10.1126/scisignal.2002351

Butt, A. M., Jones, H. C., & Abbott, N. J. (1990). Electrical resistance across the blood-brain barrier in anaesthetized rats: a developmental study. *J Physiol, 429*, 47-62.

Clavaguera, F., Bolmont, T., Crowther, R. A., Abramowski, D., Frank, S., Probst, A., . . . Tolnay, M. (2009). Transmission and spreading of tauopathy in transgenic mouse brain. *Nat Cell Biol, 11*(7), 909-913. doi:10.1038/ncb1901

Cordy, J. M., Hooper, N. M., & Turner, A. J. (2006). The involvement of lipid rafts in Alzheimer's disease. *Mol Membr Biol, 23*(1), 111-122. doi:10.1080/09687860500496417

Covaceuszach, S., Capsoni, S., Ugolini, G., Spirito, F., Vignone, D., & Cattaneo, A. (2009). Development of a non invasive NGF-based therapy for Alzheimer's disease. *Curr Alzheimer Res, 6*(2), 158-170.

Craft, S., Baker, L. D., Montine, T. J., Minoshima, S., Watson, G. S., Claxton, A., . . . Gerton, B. (2012). Intranasal insulin therapy for Alzheimer disease and

amnestic mild cognitive impairment: a pilot clinical trial. *Arch Neurol, 69*(1), 29-38. doi:10.1001/archneurol.2011.233

Deane, R., Wu, Z., Sagare, A., Davis, J., Du Yan, S., Hamm, K., . . . Zlokovic, B. V. (2004). LRP/amyloid beta-peptide interaction mediates differential brain efflux of Abeta isoforms. *Neuron, 43*(3), 333-344. doi:10.1016/j.neuron.2004.07.017

Declercq, L. D., Vandenberghe, R., Van Laere, K., Verbruggen, A., & Bormans, G. (2016). Drug Development in Alzheimer's Disease: The Contribution of PET and SPECT. *Front Pharmacol, 7*, 88. doi:10.3389/fphar.2016.00088

Ding, A., Nitsch, R., & Hoyer, S. (1992). Changes in brain monoaminergic neurotransmitter concentrations in rat after intracerebroventricular injection of streptozotocin. *J Cereb Blood Flow Metab, 12*(1), 103-109. doi:10.1038/jcbfm.1992.13

Dorrance, A. M., Matin, N., & Pires, P. W. (2014). The effects of obesity on the cerebral vasculature. *Curr Vasc Pharmacol, 12*(3), 462-472.

Duelli, R., Schrock, H., Kuschinsky, W., & Hoyer, S. (1994). Intracerebroventricular injection of streptozotocin induces discrete local changes in cerebral glucose utilization in rats. *Int J Dev Neurosci, 12*(8), 737-743.

Duffy, K. R., & Pardridge, W. M. (1987). Blood-brain barrier transcytosis of insulin in developing rabbits. *Brain Res, 420*(1), 32-38.

Farris, W., Leissring, M. A., Hemming, M. L., Chang, A. Y., & Selkoe, D. J. (2005). Alternative splicing of human insulin-degrading enzyme yields a novel isoform with a decreased ability to degrade insulin and amyloid beta-protein. *Biochemistry, 44*(17), 6513-6525. doi:10.1021/bi0476578

Freiherr, J., Hallschmid, M., Frey, W. H., 2nd, Brunner, Y. F., Chapman, C. D., Holscher, C., . . . Benedict, C. (2013). Intranasal insulin as a treatment for Alzheimer's disease: a review of basic research and clinical evidence. *CNS Drugs, 27*(7), 505-514. doi:10.1007/s40263-013-0076-8

Goh, L. K., & Sorkin, A. (2013). Endocytosis of receptor tyrosine kinases. *Cold Spring Harb Perspect Biol, 5*(5), a017459. doi:10.1101/cshperspect.a017459

Goldfine, I. D. (1987). The insulin receptor: molecular biology and transmembrane signaling. *Endocr Rev, 8*(3), 235-255. doi:10.1210/edrv-8-3-235

Grunblatt, E., Salkovic-Petrisic, M., Osmanovic, J., Riederer, P., & Hoyer, S. (2007). Brain insulin system dysfunction in streptozotocin intracerebroventricularly treated rats generates hyperphosphorylated tau protein. *J Neurochem, 101*(3), 757-770. doi:10.1111/j.1471-4159.2006.04368.x

Han, W., & Li, C. (2010). Linking type 2 diabetes and Alzheimer's disease. *Proc Natl Acad Sci U S A, 107*(15), 6557-6558. doi:10.1073/pnas.1002555107

Heni, M., Schopfer, P., Peter, A., Sartorius, T., Fritsche, A., Synofzik, M., . . . Hennige, A. M. (2014). Evidence for altered transport of insulin across the blood-brain barrier in insulin-resistant humans. *Acta Diabetol, 51*(4), 679-681. doi:10.1007/s00592-013-0546-y

Hovorka, R., & Hilgertova, J. (1991). Identification of insulin receptor systems: assessing the impact of model selection and measurement error on precision of parameter estimates using Monte Carlo study. *J Theor Biol, 151*(3), 367-383.

Hoyer, S., Lee, S. K., Loffler, T., & Schliebs, R. (2000). Inhibition of the neuronal insulin receptor. An in vivo model for sporadic Alzheimer disease? *Ann N Y Acad Sci, 920*, 256-258.

Irannejad, R., Tsvetanova, N. G., Lobingier, B. T., & von Zastrow, M. (2015). Effects of endocytosis on receptor-mediated signaling. *Curr Opin Cell Biol, 35*, 137-143. doi:10.1016/j.ceb.2015.05.005

Kabayama, K., Sato, T., Saito, K., Loberto, N., Prinetti, A., Sonnino, S., . . . Inokuchi, J. (2007). Dissociation of the insulin receptor and caveolin-1 complex by ganglioside GM3 in the state of insulin resistance. *Proc Natl Acad Sci U S A, 104*(34), 13678-13683. doi:10.1073/pnas.0703650104

Kamei, N., Shingaki, T., Kanayama, Y., Tanaka, M., Zochi, R., Hasegawa, K., . . . Takeda-Morishita, M. (2016). Visualization and Quantitative Assessment of the Brain Distribution of Insulin through Nose-to-Brain Delivery Based on the Cell-Penetrating Peptide Noncovalent Strategy. *Mol Pharm, 13*(3), 1004-1011. doi:10.1021/acs.molpharmaceut.5b00854

Kosuda, S., Kusano, S., Aoki, S., Suzuki, K., Fujii, H., Kawakami, R., . . . et al. (1993). [Brain SPECT by intraarterial infusion of 99mTc-HMPAO for assessing the cerebral distribution of carotid artery infusions in patients with brain tumor]. *Kaku Igaku, 30*(6), 613-620.

Lannert, H., & Hoyer, S. (1998). Intracerebroventricular administration of streptozotocin causes long-term diminutions in learning and memory abilities and in cerebral energy metabolism in adult rats. *Behav Neurosci, 112*(5), 1199-1208.

Lee, W. L., & Klip, A. (2016). Endothelial Transcytosis of Insulin: Does It Contribute to Insulin Resistance? *Physiology (Bethesda), 31*(5), 336-345. doi:10.1152/physiol.00010.2016

Ling, X., Martins, R. N., Racchi, M., Craft, S., & Helmerhorst, E. (2002). Amyloid beta antagonizes insulin promoted secretion of the amyloid beta protein precursor. *J Alzheimers Dis, 4*(5), 369-374.

Ljubicic, S., Bezzi, P., Brajkovic, S., Nesca, V., Guay, C., Ohbayashi, N., . . . Regazzi, R. (2013). The GTPase Rab37 Participates in the Control of Insulin Exocytosis. *Plos One, 8*(6). doi:ARTN e68255

10.1371/journal.pone.0068255

Mackic, J. B., Weiss, M. H., Miao, W., Kirkman, E., Ghiso, J., Calero, M., . . . Zlokovic, B. V. (1998). Cerebrovascular accumulation and increased blood-brain barrier permeability to circulating Alzheimer's amyloid beta peptide in aged squirrel monkey with cerebral amyloid angiopathy. *J Neurochem, 70*(1), 210-215.

Malakar, P., Chartarifsky, L., Hija, A., Leibowitz, G., Glaser, B., Dor, Y., & Karni, R. (2016). Insulin receptor alternative splicing is regulated by insulin signaling and modulates beta cell survival. *Sci Rep, 6*, 31222. doi:10.1038/srep31222

Marshall, S. (1985). Kinetics of insulin receptor internalization and recycling in adipocytes. Shunting of receptors to a degradative pathway by inhibitors of recycling. *J Biol Chem, 260*(7), 4136-4144.

Matsuzaki, T., Sasaki, K., Tanizaki, Y., Hata, J., Fujimi, K., Matsui, Y., . . . Iwaki, T. (2010). Insulin resistance is associated with the pathology of Alzheimer disease: the Hisayama study. *Neurology, 75*(9), 764-770. doi:10.1212/WNL.0b013e3181eee25f

Mawuenyega, K. G., Sigurdson, W., Ovod, V., Munsell, L., Kasten, T., Morris, J. C., . . . Bateman, R. J. (2010). Decreased clearance of CNS beta-amyloid in Alzheimer's disease. *Science, 330*(6012), 1774. doi:10.1126/science.1197623

Molina, J. A., Jimenez-Jimenez, F. J., Vargas, C., Gomez, P., de Bustos, F., Gomez-Escalonilla, C., . . . Arenas, J. (2002). Cerebrospinal fluid levels of insulin in patients with Alzheimer's disease. *Acta Neurol Scand, 106*(6), 347-350.

Morino-Koga, S., Yano, S., Kondo, T., Shimauchi, Y., Matsuyama, S., Okamoto, Y., . . . Kai, H. (2013). Insulin receptor activation through its accumulation in lipid rafts by mild electrical stress. *J Cell Physiol, 228*(2), 439-446. doi:10.1002/jcp.24149

Ott, A., Stolk, R. P., van Harskamp, F., Pols, H. A., Hofman, A., & Breteler, M. M. (1999). Diabetes mellitus and the risk of dementia: The Rotterdam Study. *Neurology, 53*(9), 1937-1942.

Patlak, C. S., Blasberg, R. G., & Fenstermacher, J. D. (1983). Graphical evaluation of blood-to-brain transfer constants from multiple-time uptake data. *J Cereb Blood Flow Metab, 3*(1), 1-7. doi:10.1038/jcbfm.1983.1

Plaschke, K., & Hoyer, S. (1993). Action of the diabetogenic drug streptozotocin on glycolytic and glycogenolytic metabolism in adult rat brain cortex and hippocampus. *Int J Dev Neurosci, 11*(4), 477-483.

Plaschke, K., Kopitz, J., Siegelin, M., Schliebs, R., Salkovic-Petrisic, M., Riederer, P., & Hoyer, S. (2010). Insulin-resistant brain state after intracerebroventricular streptozotocin injection exacerbates Alzheimer-like changes in Tg2576 AbetaPP-overexpressing mice. *J Alzheimers Dis, 19*(2), 691-704. doi:10.3233/JAD-2010-1270

Preston, J. E., Joan Abbott, N., & Begley, D. J. (2014). Transcytosis of macromolecules at the blood-brain barrier. *Adv Pharmacol, 71*, 147-163. doi:10.1016/bs.apha.2014.06.001

Rivera, E. J., Goldin, A., Fulmer, N., Tavares, R., Wands, J. R., & de la Monte, S. M. (2005). Insulin and insulin-like growth factor expression and function deteriorate with progression of Alzheimer's disease: link to brain reductions in acetylcholine. *J Alzheimers Dis, 8*(3), 247-268.

Rosenbloom, M. H., Barclay, T. R., Pyle, M., Owens, B. L., Cagan, A. B., Anderson, C. P., . . . Hanson, L. R. (2014). A single-dose pilot trial of intranasal rapid-acting insulin in apolipoprotein E4 carriers with mild-moderate Alzheimer's disease. *CNS Drugs, 28*(12), 1185-1189. doi:10.1007/s40263-014-0214-y

Sajja, R. K., Prasad, S., & Cucullo, L. (2014). Impact of altered glycaemia on blood-brain barrier endothelium: an in vitro study using the hCMEC/D3 cell line. *Fluids Barriers CNS, 11*(1), 8. doi:10.1186/2045-8118-11-8

Sanchez-Wandelmer, J., Davalos, A., Herrera, E., Giera, M., Cano, S., de la Pena, G., . . . Busto, R. (2009). Inhibition of cholesterol biosynthesis disrupts lipid raft/caveolae and affects insulin receptor activation in 3T3-L1 preadipocytes. *Biochim Biophys Acta, 1788*(9), 1731-1739. doi:10.1016/j.bbamem.2009.05.002

Spires-Jones, T. L., de Calignon, A., Meyer-Luehmann, M., Bacskai, B. J., & Hyman, B. T. (2011). Monitoring protein aggregation and toxicity in Alzheimer's disease mouse models using in vivo imaging. *Methods, 53*(3), 201-207. doi:10.1016/j.ymeth.2010.12.009

Stanley, M., Macauley, S. L., Caesar, E. E., Koscal, L. J., Moritz, W., Robinson, G. O., . . . Holtzman, D. M. (2016). The Effects of Peripheral and Central High Insulin on Brain Insulin Signaling and Amyloid-beta in Young and Old APP/PS1 Mice. *J Neurosci, 36*(46), 11704-11715. doi:10.1523/JNEUROSCI.2119-16.2016

Steen, E., Terry, B. M., Rivera, E. J., Cannon, J. L., Neely, T. R., Tavares, R., . . . de la Monte, S. M. (2005). Impaired insulin and insulin-like growth factor expression and signaling mechanisms in Alzheimer's disease--is this type 3 diabetes? *J Alzheimers Dis, 7*(1), 63-80.

Storck, S. E., Meister, S., Nahrath, J., Meissner, J. N., Schubert, N., Di Spiezio, A., . . . Pietrzik, C. U. (2016). Endothelial LRP1 transports amyloid-beta(1-42) across the blood-brain barrier. *J Clin Invest, 126*(1), 123-136. doi:10.1172/JCI81108

Stoscheck, C. M., & Carpenter, G. (1984). Characterization of the metabolic turnover of epidermal growth factor receptor protein in A-431 cells. *J Cell Physiol, 120*(3), 296-302. doi:10.1002/jcp.1041200306

Suzuki, A., Takeuchi, W., Ishitsu, T., Morimoto, Y., Kobashi, K., & Ueno, Y. (2015). High-resolution brain SPECT imaging by combination of parallel and tilted detector heads. *Ann Nucl Med, 29*(8), 682-696. doi:10.1007/s12149-015-0992-4

Swaminathan, S. K., Ahlschwede, K. M., Sarma, V., Curran, G. L., Omtri, R. S., Decklever, T., . . . Kandimalla, K. K. (2017). Insulin differentially affects the distribution kinetics of amyloid beta 40 and 42 in plasma and brain. *J Cereb Blood Flow Metab*, 271678X17709709. doi:10.1177/0271678X17709709

Takeda, S., Sato, N., Uchio-Yamada, K., Sawada, K., Kunieda, T., Takeuchi, D., . . . Morishita, R. (2010). Diabetes-accelerated memory dysfunction via cerebrovascular inflammation and Abeta deposition in an Alzheimer mouse model with diabetes. *Proc Natl Acad Sci U S A, 107*(15), 7036-7041. doi:10.1073/pnas.1000645107

Talbot, K., Wang, H. Y., Kazi, H., Han, L. Y., Bakshi, K. P., Stucky, A., . . . Arnold, S. E. (2012). Demonstrated brain insulin resistance in Alzheimer's disease patients is associated with IGF-1 resistance, IRS-1 dysregulation,

and cognitive decline. *J Clin Invest, 122*(4), 1316-1338. doi:10.1172/JCI59903

Tamaki, C., Ohtsuki, S., & Terasaki, T. (2007). Insulin facilitates the hepatic clearance of plasma amyloid beta-peptide (1 40) by intracellular translocation of low-density lipoprotein receptor-related protein 1 (LRP-1) to the plasma membrane in hepatocytes. *Mol Pharmacol, 72*(4), 850-855. doi:10.1124/mol.107.036913

Templeman, N. M., Flibotte, S., Chik, J. H. L., Sinha, S., Lim, G. E., Foster, L. J., . . . Johnson, J. D. (2017). Reduced Circulating Insulin Enhances Insulin Sensitivity in Old Mice and Extends Lifespan. *Cell Rep, 20*(2), 451-463. doi:10.1016/j.celrep.2017.06.048

Urayama, A., & Banks, W. A. (2008). Starvation and triglycerides reverse the obesity-induced impairment of insulin transport at the blood-brain barrier. *Endocrinology, 149*(7), 3592-3597. doi:10.1210/en.2008-0008

Van Cauwenberghe, C., Van Broeckhoven, C., & Sleegers, K. (2016). The genetic landscape of Alzheimer disease: clinical implications and perspectives. *Genet Med, 18*(5), 421-430. doi:10.1038/gim.2015.117

van de Haar, H. J., Jansen, J. F., van Osch, M. J., van Buchem, M. A., Muller, M., Wong, S. M., . . . Backes, W. H. (2016). Neurovascular unit impairment in early Alzheimer's disease measured with magnetic resonance imaging. *Neurobiol Aging, 45*, 190-196. doi:10.1016/j.neurobiolaging.2016.06.006

Wang, H., Wang, A. X., Liu, Z., & Barrett, E. J. (2008). Insulin signaling stimulates insulin transport by bovine aortic endothelial cells. *Diabetes, 57*(3), 540-547. doi:10.2337/db07-0967

Wang, Q., & Lu, Z. (1994). [The presence and distribution of insulin in rat brain and its relation to feeding]. *Zhongguo Yi Xue Ke Xue Yuan Xue Bao, 16*(6), 434-437.

Werther, G. A., Hogg, A., Oldfield, B. J., McKinley, M. J., Figdor, R., & Mendelsohn, F. A. (1989). Localization and Characterization of Insulin-Like Growth Factor-I Receptors in Rat Brain and Pituitary Gland Using in vitro Autoradiography and Computerized Densitometry* A Distinct Distribution from Insulin Receptors. *J Neuroendocrinol, 1*(5), 369-377. doi:10.1111/j.1365-2826.1989.tb00131.x

Wilinska, M. E., Chassin, L. J., Schaller, H. C., Schaupp, L., Pieber, T. R., & Hovorka, R. (2005). Insulin kinetics in type-I diabetes: continuous and bolus delivery of rapid acting insulin. *IEEE Trans Biomed Eng, 52*(1), 3-12. doi:10.1109/TBME.2004.839639

Winkler, E. A., Nishida, Y., Sagare, A. P., Rege, S. V., Bell, R. D., Perlmutter, D., . . . Zlokovic, B. V. (2015). GLUT1 reductions exacerbate Alzheimer's disease vasculo-neuronal dysfunction and degeneration. *Nat Neurosci, 18*(4), 521-530. doi:10.1038/nn.3966

Yoon, N., Dang, T. Q., Chasiotis, H., Kelly, S. P., & Sweeney, G. (2014). Altered transendothelial transport of hormones as a contributor to diabetes. *Diabetes Metab J, 38*(2), 92-99. doi:10.4093/dmj.2014.38.2.92

Yuede, C. M., Lee, H., Restivo, J. L., Davis, T. A., Hettinger, J. C., Wallace, C. E., . . . Cirrito, J. R. (2016). Rapid in vivo measurement of beta-amyloid reveals biphasic clearance kinetics in an Alzheimer's mouse model. *J Exp Med, 213*(5), 677-685. doi:10.1084/jem.20151428

Zhang, Y., Zhou, B., Deng, B., Zhang, F., Wu, J., Wang, Y., . . . Zhai, Q. (2013). Amyloid-beta induces hepatic insulin resistance in vivo via JAK2. *Diabetes, 62*(4), 1159-1166. doi:10.2337/db12-0670

Zlokovic, B. (1997). Can blood-brain barrier play a role in the development of cerebral amyloidosis and Alzheimer's disease pathology. *Neurobiol Dis, 4*(1), 23-26. doi:10.1006/nbdi.1997.0134

APPENDIX

CHAPTER 2

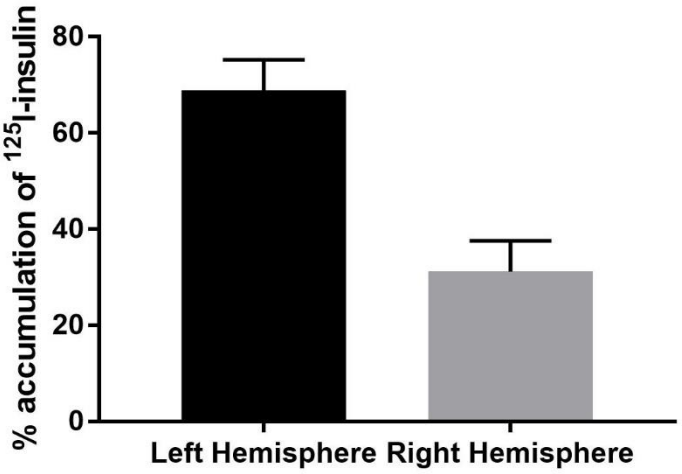

Figure A1. Percentage accumulation of left and right brain hemisphere accumulation of 100 µCi of ^{125}I-insulin dosed via the internal carotid

CHAPTER 3

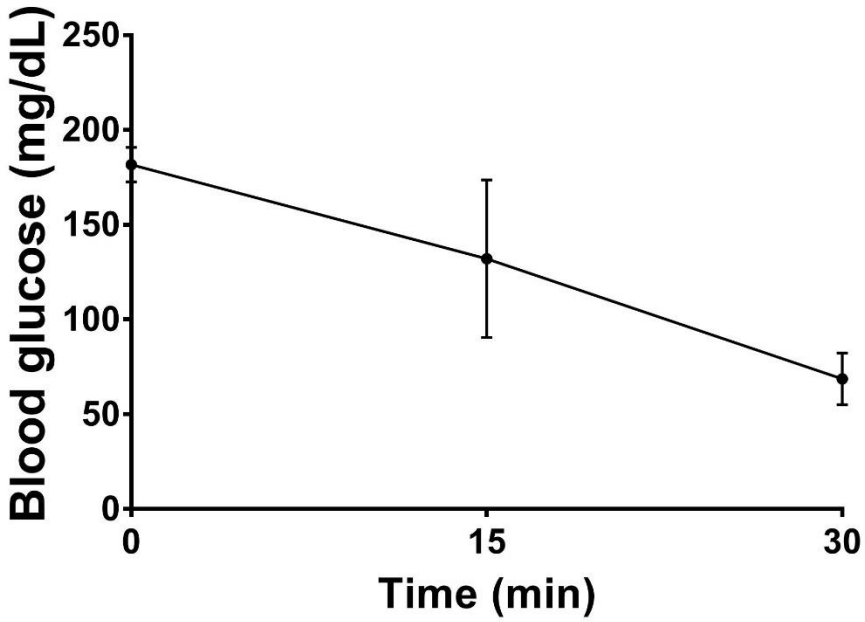

Figure A2. Tolerance of WT mice (n=3), represented as blood glucose levels (mg/dl), to the intraperitoneal administration of 100µCi of ^{125}I-insulin

CHAPTER 4

Example of back-end equations for 5-compartmental model on Stella©:

BBB(t) = BBB(t - dt) + (R13 - Flow_1) * dt

INIT BBB = 0

INFLOWS:

R13 = k41*Plasma

OUTFLOWS:

Flow_1 = k34*BBB/no_of_int_compt

BBB_AUC(t) = BBB_AUC(t - dt) + (INTEGRATOR) * dt

INIT BBB_AUC = INT(INTEGRATOR)

INFLOWS:

INTEGRATOR = BBB

Brain_AUC(t) = Brain_AUC(t - dt) + (Flow_3) * dt

INIT Brain_AUC = INT(Flow_3)

INFLOWS:

Flow_3 = Brain_tissue

Brain_tissue(t) = Brain_tissue(t - dt) + (Flow_1 - Flow_2) * dt

INIT Brain_tissue = 0

INFLOWS:

Flow_1 = k34*BBB/no_of_int_compt

OUTFLOWS:

Flow_2 = Brain_tissue*k13

Elimination_compt(t) = Elimination_compt(t - dt) + (Rateelim) * dt

INIT Elimination_compt = 0

INFLOWS:

Rateelim = k01*Plasma

Plasma(t) = Plasma(t - dt) + (R21 + Flow_2 - R12 - R13 - Rateelim) * dt

INIT Plasma = 100

INFLOWS:

R21 = Tissue*k12

Flow_2 = Brain_tissue*k13

OUTFLOWS:

R12 = k21*Plasma

R13 = k41*Plasma

Rateelim = k01*Plasma

Plasma_AUC(t) = Plasma_AUC(t - dt) + (Plasma_int) * dt

INIT Plasma_AUC = INT(Plasma_int)

INFLOWS:

Plasma_int = Plasma

Tissue(t) = Tissue(t - dt) + (R12 - R21) * dt

INIT Tissue = 0

INFLOWS:

R12 = k21*Plasma

OUTFLOWS:

R21 = Tissue*k12

Tissue_AUC(t) = Tissue_AUC(t - dt) + (Tissue_int) * dt

INIT Tissue_AUC = INT(Tissue_int)

INFLOWS:

Tissue_int = Tissue

k01 = 0.256

k12 = 0.391

k13 = 0.0035

k21 = 0.348

k34 = 0.5

k41 = 0.00142

no_of_int_compt = 4

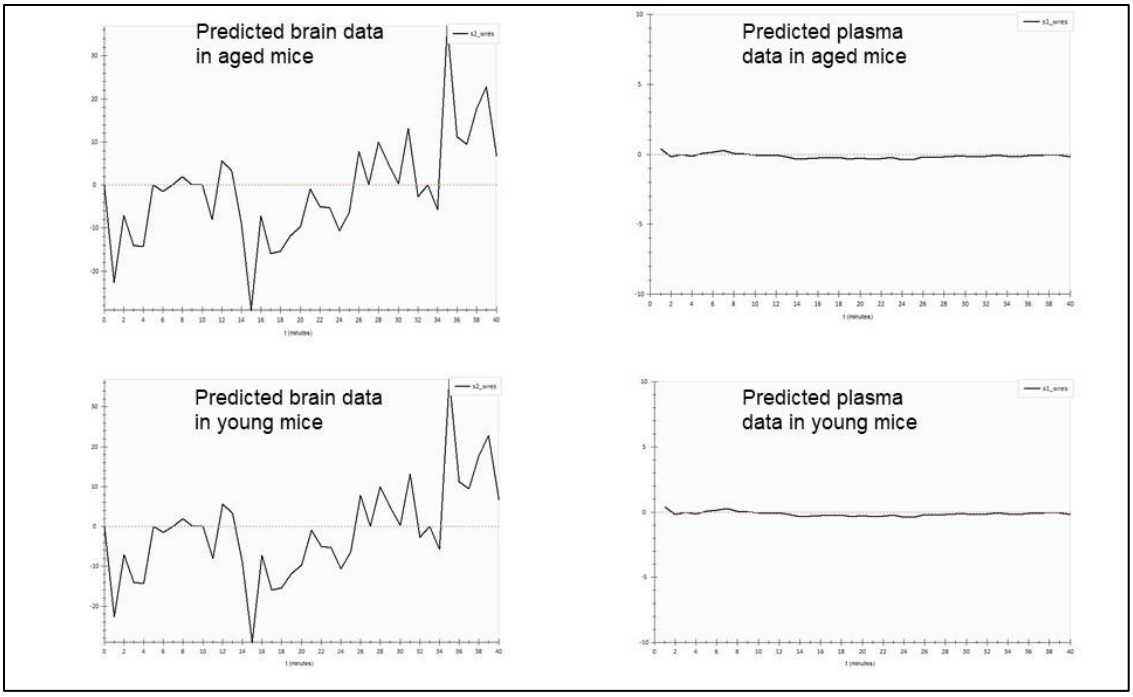

Figure A3. Weighted residuals of predicted values (from SAAM II©) for brain and plasma concentration profiles of ^{125}I-insulin in young and aged mice (n=1; representative plots)

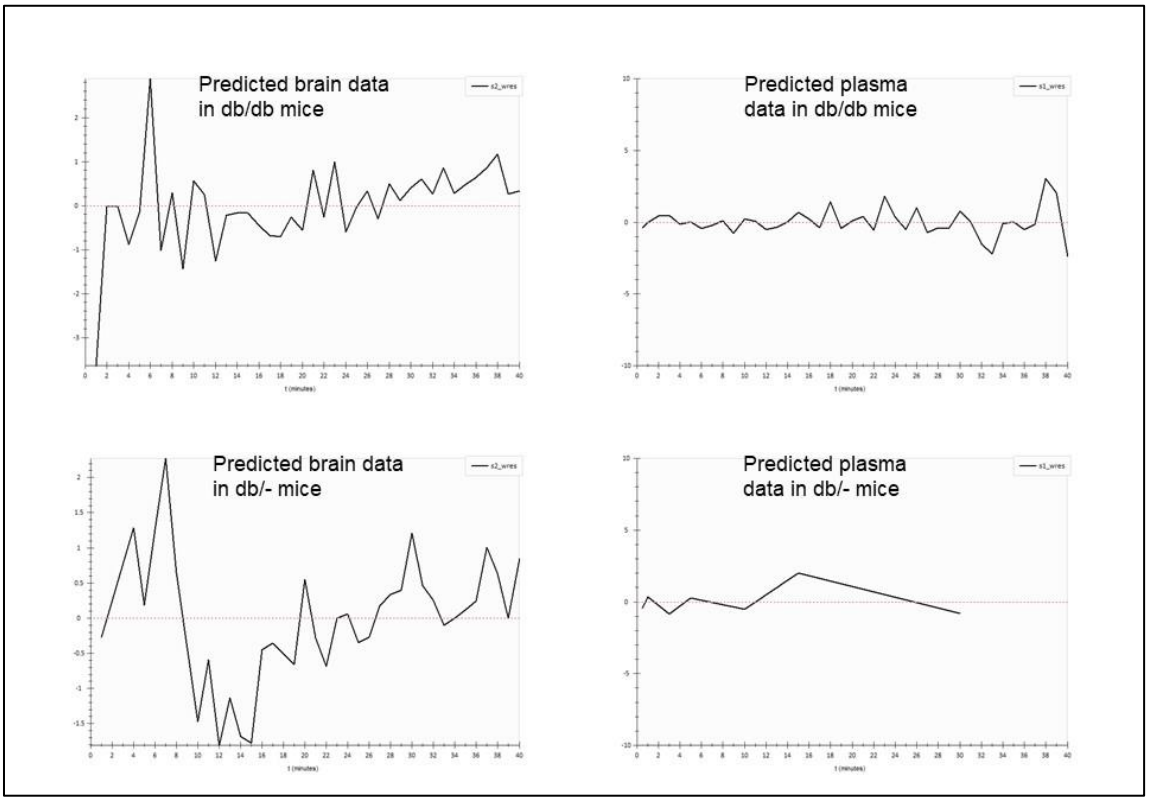

Figure A4. Weighted residuals of predicted values (from SAAM II©) for brain and plasma concentration profiles of ^{125}I-insulin in db/db and db/- mice (n=1; representative plots)

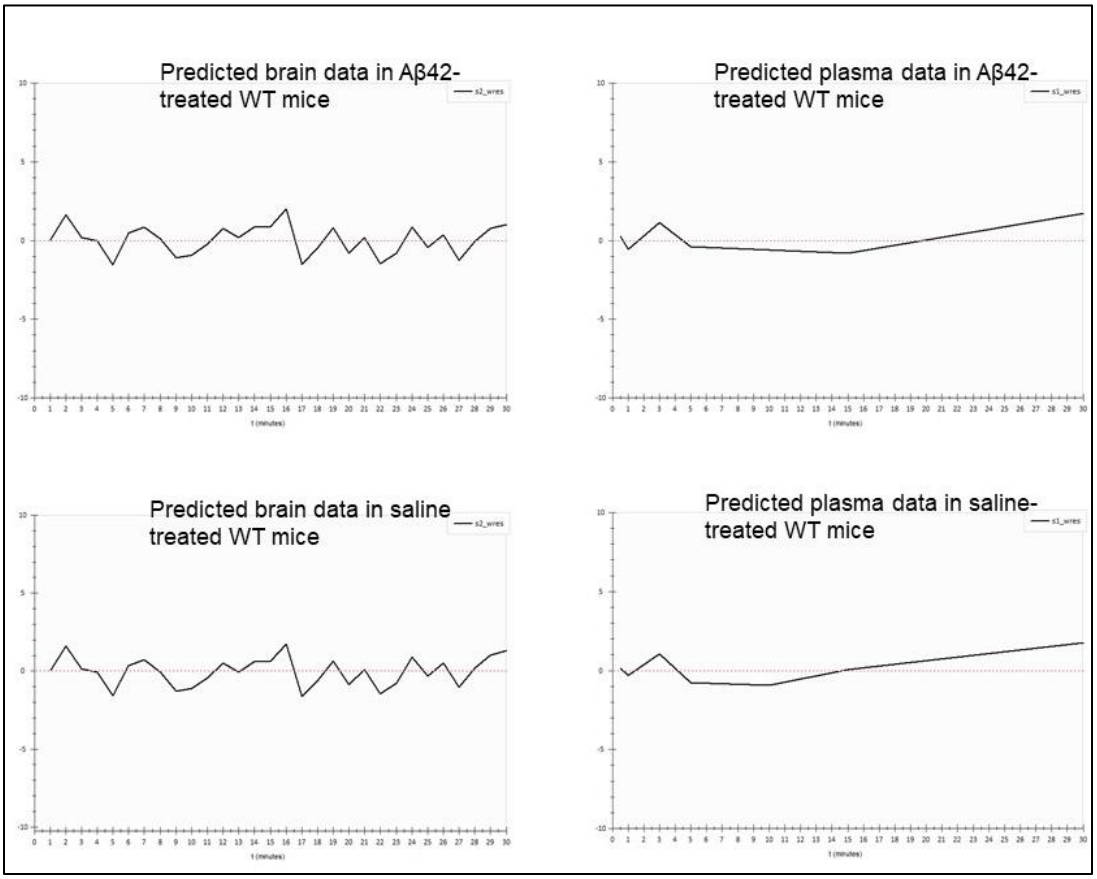

Figure A5. Weighted residuals of predicted values (from SAAM II©) for brain and plasma concentration profiles of ^{125}I-insulin in Aβ42-treated and saline-treated WT mice (n=1; representative plots)

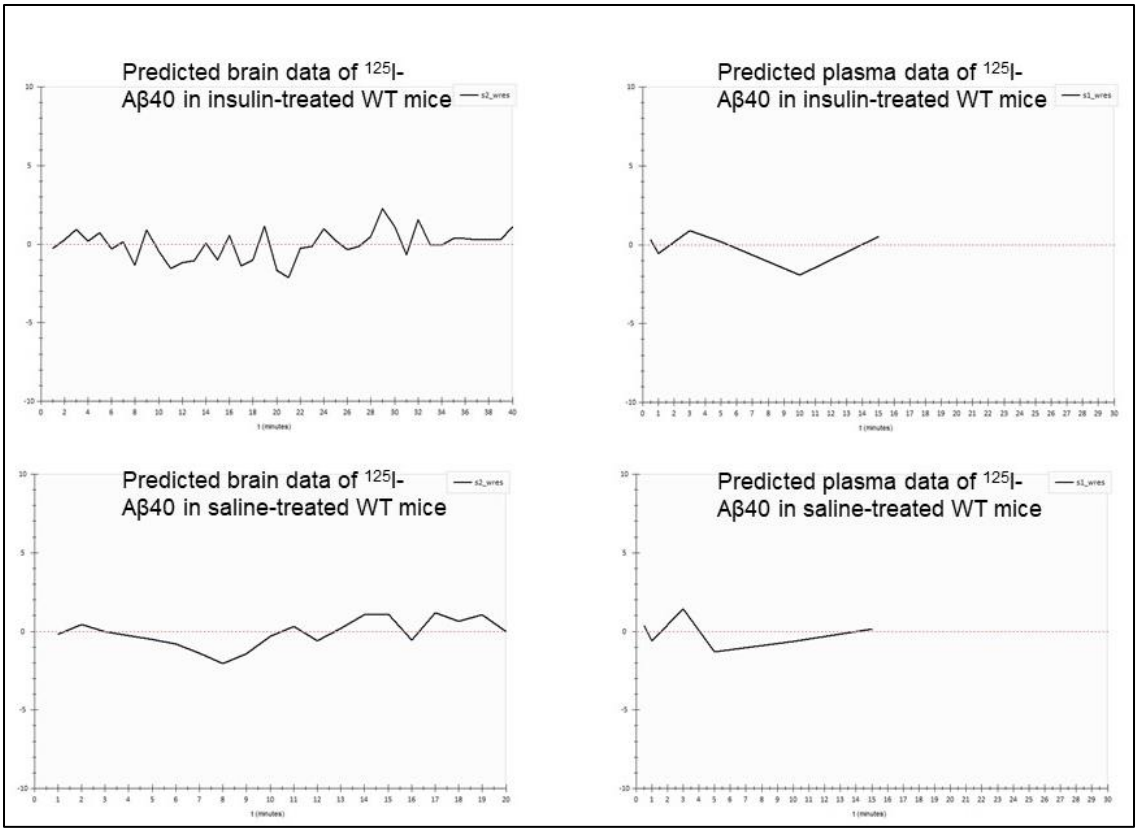

Figure A6. Weighted residuals of predicted values (from SAAM II©) for brain and plasma concentration profiles of ^{125}I-Aβ40 in insulin-treated or saline-treated WT mice (n=1; representative plots)

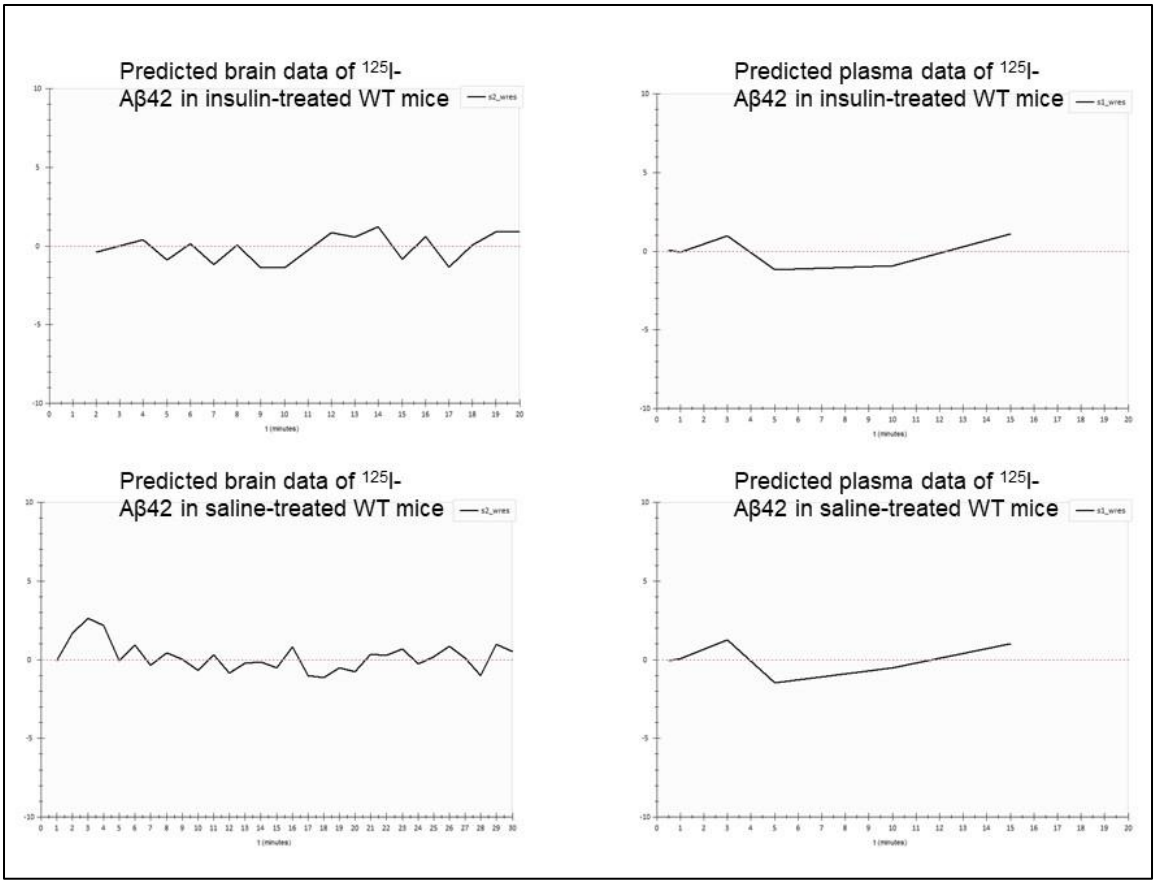

Figure A7. Weighted residuals of predicted values (from SAAM II©) for brain and plasma concentration profiles of ^{125}I-Aβ42 in insulin-treated or saline-treated WT mice (n=1; representative plots)

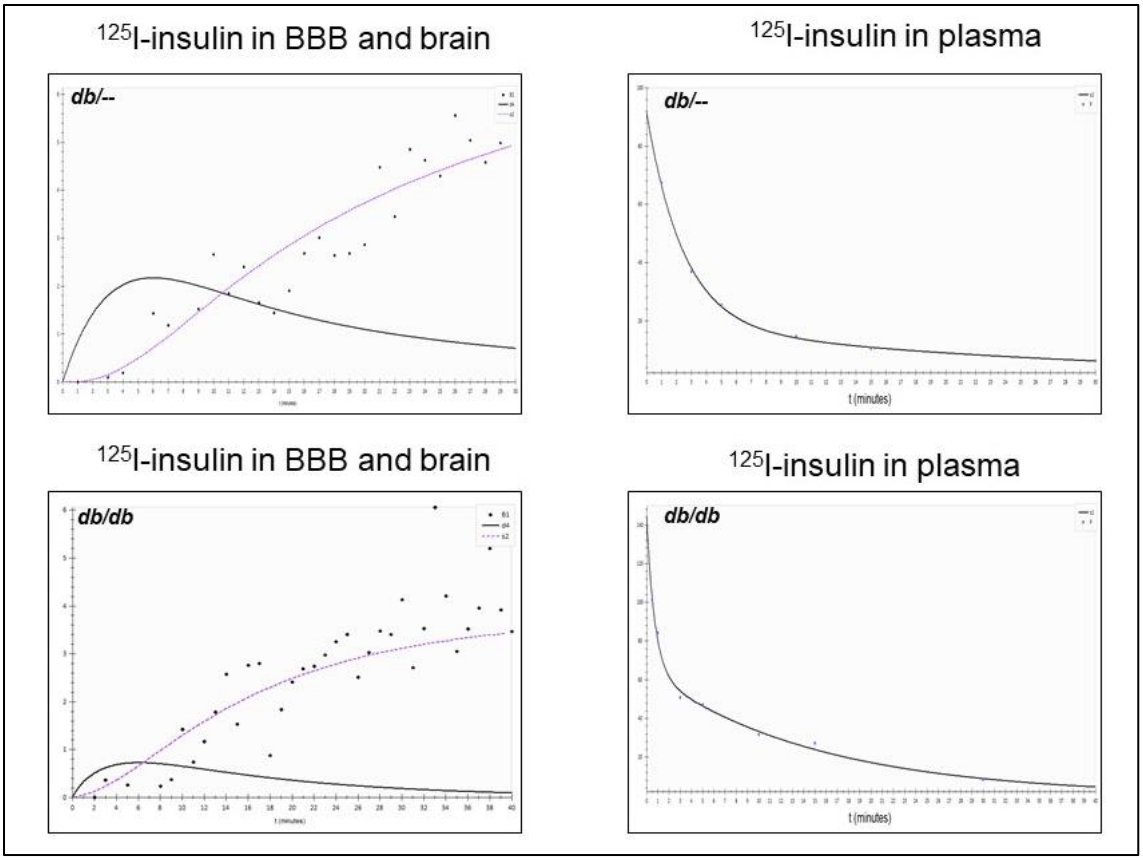

Figure A8. Predicted BBB, brain and peripheral tissue amounts (from SAAM II©) for ^{125}I-insulin in db/- and db/db mice (n=1; representative plots)

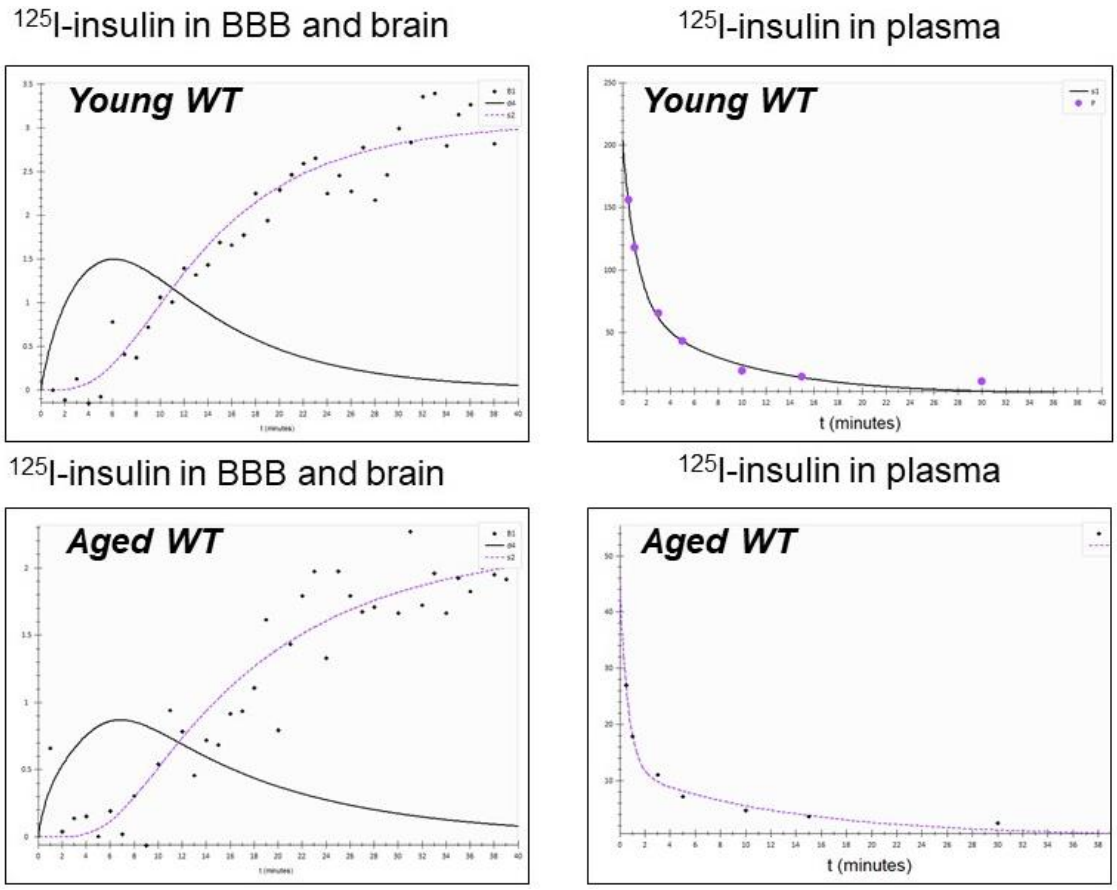

Figure A9. Predicted BBB, brain and peripheral tissue amounts (from SAAM II©) for ^{125}I-insulin in young and aged WT mice (n=1; representative plots)

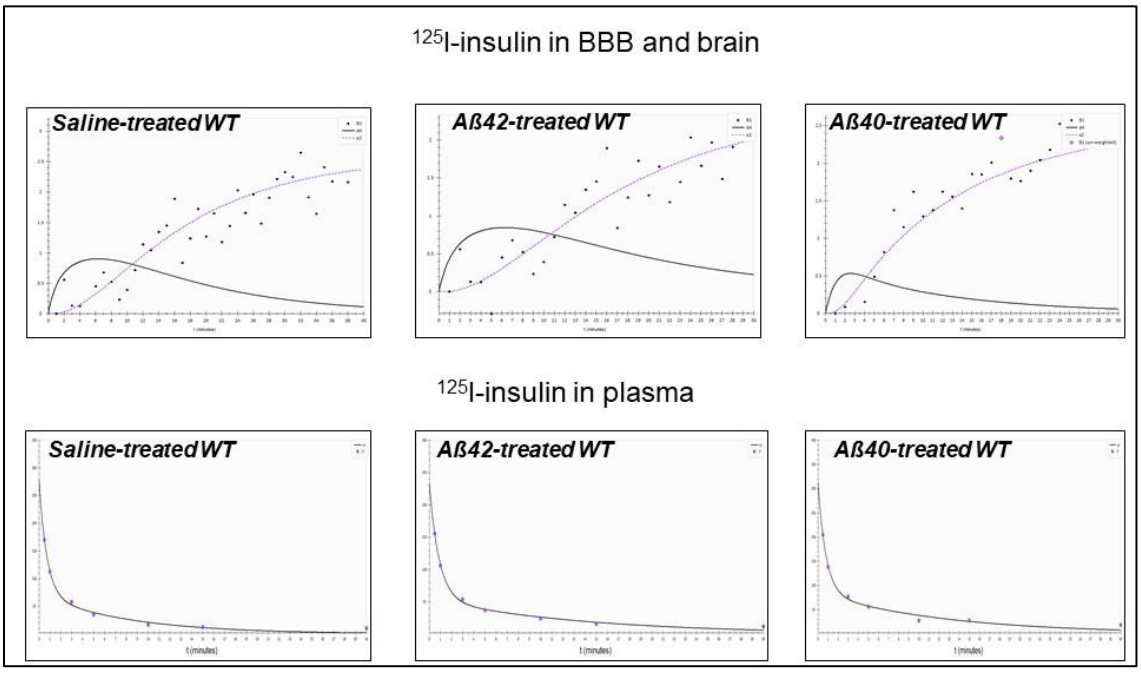

Figure A11. Predicted BBB, brain and peripheral tissue amounts (from SAAM II©) for ^{125}I-insulin in WT mice treated with either saline, Aß40 or Aß42 (n=1; representative plots)

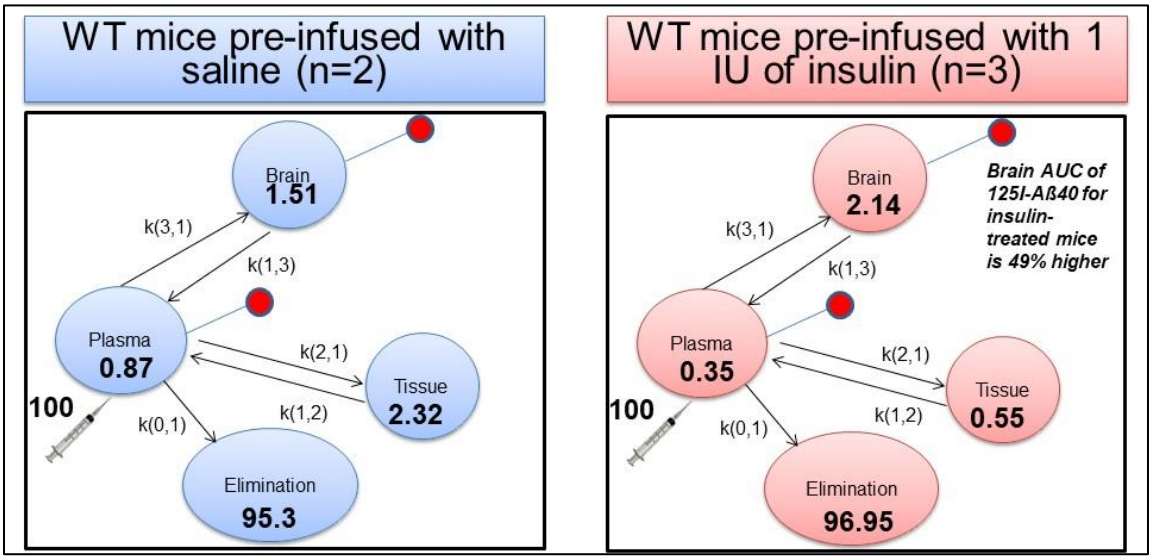

Figure A12. Schematic of predicted mass distribution after 45 minutes following dose of 100 units of Aβ40 into the plasma of WT mice pre-treated with either saline or 1IU of insulin. Values for the distribution parameters were obtained from mean estimates of rate constants derived from SAAM II© analysis of ^{125}I- Aβ40 distribution from saline pre-treated (n=2) and insulin pre-treated(n=3) mice (described in chapter 4)

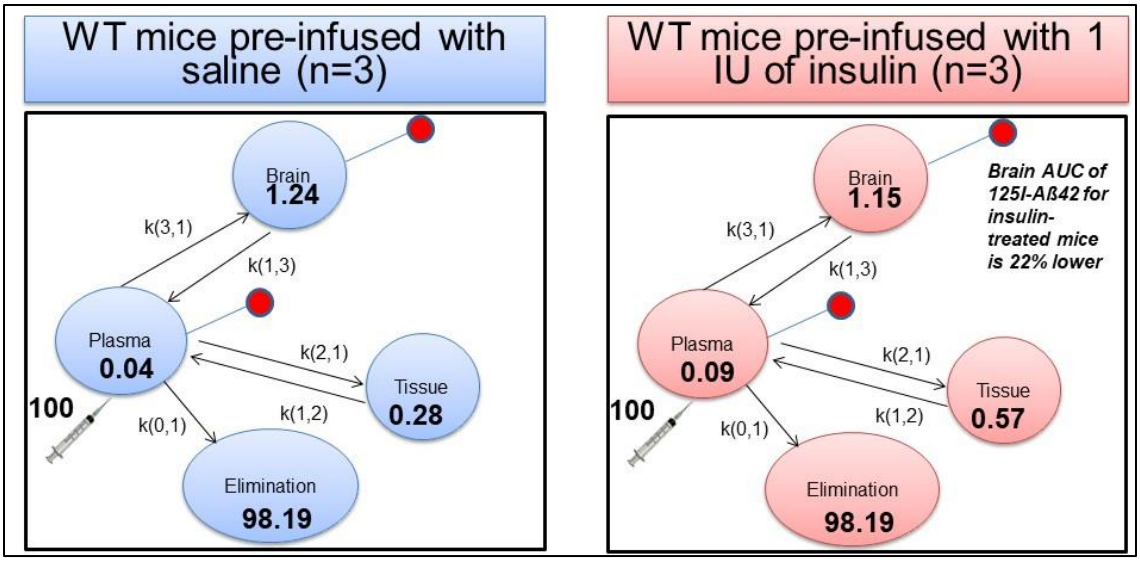

Figure A13. Schematic of predicted mass distribution after 45 minutes following dose of 100 units of insulin into the plasma of db/db or $db^{/-}$ mice. Values for the distribution parameters were obtained from mean estimates of rate constants derived from SAAM II© analysis of ^{125}I-insulin distribution from db—(n=5) and db/db(n=3) mice (described in chapter 4)

CHAPTER 5

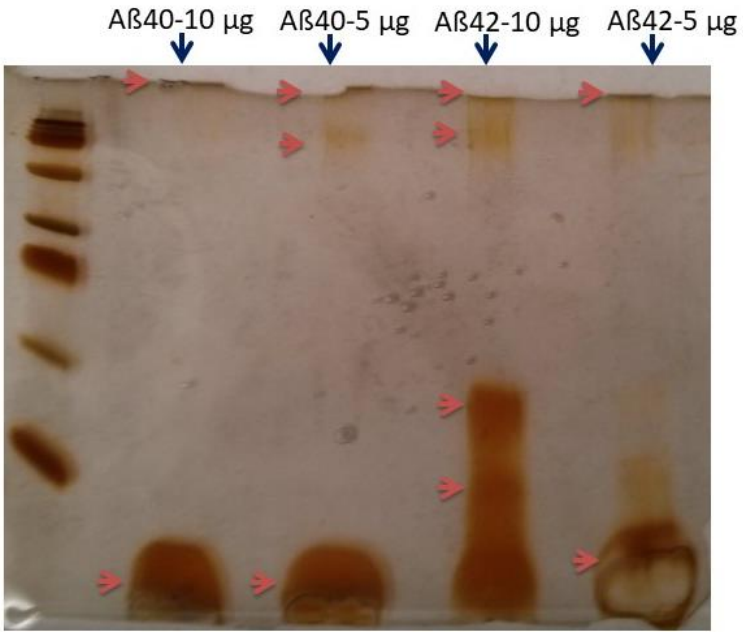

Figure A14. Silver stains of reconstituted Aβ40 and Aβ42 films. Morphology of either 5 or 10μg of Aβ40 and Aβ42 utilized for in-vitro studies concerning insulin transport across the blood-brain barrier.

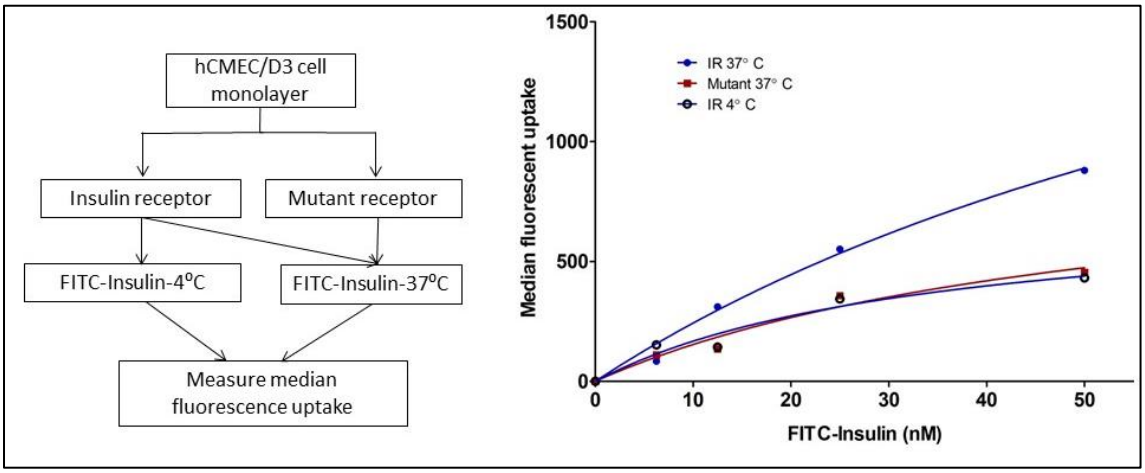

Figure A15. Median fluorescent uptake of increasing concentrations FITC-insulin uptake into polarized hCMEC/D3 monolayers is temperature-dependent and IR-mediated. hCMEC/D3 cell monolayers were over-expressed with 1.5 μg/ml of either IR-WT or mutant IR DNA. The IR-WT overexpressed cells were treated with increasing concentrations of FITC-insulin for 30 minutes at either 4ºC or 37ºC; mutant IR overexpressed cells were treated in the same manner at 37ºC for 30 minutes. Cell monolayers were washed and analyzed for FITC-insulin uptake by Flow Cytometry (BD Accuri©). Averaged median fluorescent uptake of FITC-insulin is higher in hCMEC/D3 overexpressed with IR-WT at 37ºC as compared to that at 4ºC or in cells overexpressed with mutant IR at 37ºC